



TECHNISCHE  
UNIVERSITÄT  
WIEN  
Vienna University of Technology

# DISSERTATION

## Grain Boundaries and Interfaces in Thin Films of Yttria Stabilized Zirconia (YSZ)

ausgeführt am

Institut Chemische Technologien und Analytik,  
FB Elektrochemie,  
der Technischen Universität Wien

unter Anleitung von

Univ. Prof. Dipl. Phys. Dr. Jürgen Fleig

durch

**Dipl. Ing. Matthias Gerstl**

Matrikelnummer: 0325384

Sonnenuhrgasse 6/18

A-1060 Wien

Wien, im Februar 2012

# Contents

<b>1</b>	<b>Introduction and State of Research</b>	<b>1</b>
<b>2</b>	<b>Theoretical Aspects</b>	<b>5</b>
2.1	Solid oxide fuel cells (SOFC)	5
2.2	Defects in Solids	7
2.2.1	Point defects	7
2.2.2	Mass and charge transport	11
2.2.3	Conductivity	14
2.3	Defect chemistry in YSZ	16
2.3.1	Yttria doping	16
2.3.2	Grain boundaries	18
2.4	Phenomenological diffusion coefficients	19
2.4.1	Conductivity based diffusion coefficient	20
2.4.2	Tracer diffusion coefficient	21
2.4.3	Chemical diffusion coefficient	22
2.5	Impedance Spectroscopy	23
2.5.1	Impedance spectra	23
2.5.2	Equivalent circuits	24

2.5.3	The charge transfer resistance . . . . .	28
2.6	Time of Flight Secondary Ion Mass Spectrometry (TOF-SIMS) . . . . .	29
2.6.1	Introduction and principle of TOF-SIMS . . . . .	29
2.6.2	Evaluation of the <sup>18</sup> O concentration profiles . . . . .	31
<b>3</b>	<b>Experimental</b>	<b>35</b>
3.1	Sample preparation . . . . .	35
3.1.1	Sol-Gel process . . . . .	35
3.1.2	Pulsed laser deposition (PLD) . . . . .	36
3.1.3	Photolithography and magnetron sputtering . . . . .	37
3.2	Sample Characterisation . . . . .	38
3.2.1	X-ray diffraction (XRD) . . . . .	38
3.2.2	Evaluation of the film thicknesses . . . . .	39
3.2.3	Atomic force microscopy (AFM) . . . . .	39
3.2.4	Electrical impedance spectroscopy . . . . .	39
3.2.5	Tracer diffusion experiments . . . . .	41
3.2.6	TOF-SIMS . . . . .	43
3.3	Simulation . . . . .	43
<b>4</b>	<b>The separation of grain and grain boundary impedance in thin YSZ layers</b>	<b>46</b>
4.1	Introduction . . . . .	46
4.2	Theoretical Considerations . . . . .	46
4.3	Experimental Results and Discussion . . . . .	55
4.3.1	Microstructure of the YSZ thin films . . . . .	55
4.3.2	Electrical Measurements . . . . .	56
4.4	Conclusions . . . . .	71
<b>5</b>	<b>Sol-gel prepared thin layers of yttria stabilized zirconia</b>	<b>73</b>
5.1	Introduction . . . . .	73

5.2	Experimental Results and Discussion . . . . .	74
5.2.1	Microstructure of the YSZ films . . . . .	74
5.2.2	Electrical properties of the YSZ films . . . . .	77
5.3	Conclusions . . . . .	83
<b>6</b>	<b>Current driven tracer incorporation in thin films of YSZ</b>	<b>84</b>
6.1	Introduction . . . . .	84
6.2	Methodology . . . . .	84
6.3	Experimental results and discussion . . . . .	85
6.3.1	Results on layer S . . . . .	86
6.3.2	Results on layer F . . . . .	90
6.4	Conclusions . . . . .	92
<b>7</b>	<b>Tracer diffusion studies in thin film YSZ</b>	<b>96</b>
7.1	Introduction . . . . .	96
7.2	Theoretical considerations . . . . .	96
7.3	Experimental results and discussion . . . . .	101
7.3.1	Microstructure of the YSZ thin films . . . . .	102
7.3.2	Electrical impedance spectroscopy . . . . .	105
7.3.3	Tracer diffusion experiments . . . . .	111
7.4	Conclusions . . . . .	117
<b>8</b>	<b>Summary of the scientific achievements</b>	<b>118</b>
	<b>Bibliography</b>	<b>122</b>

# Abstract

Thin films of yttria stabilized zirconia (YSZ) were prepared on magnesia, sapphire and strontium titanate (STO) single crystals using pulsed laser deposition (PLD) and a sol-gel method. The thin films were characterised regarding their lateral grain size and thickness with atomic force microscopy (AFM) and digital holographic microscopy (DHM). The crystallinity and texture was determined by X-ray diffraction (XRD). However, the focus laid on the bulk and interfacial mass and charge transport properties of said films, which were investigated by impedance spectroscopy and tracer diffusion measurements analysed by means of time of flight secondary ion mass spectrometry (TOF-SIMS).

An improved electrode geometry is introduced to study thin ion conducting films by impedance spectroscopy. It is shown that long, thin, and closely spaced electrodes arranged interdigitally allow a separation of grain and grain boundary effects also in very thin films. Results demonstrate that YSZ films produced by pulsed laser deposition and the sol-gel method on sapphire substrates exhibit a bulk conductivity which is very close to that of macroscopic YSZ samples, while the bulk conductivity of YSZ on magnesia was lower due to a lower degree of crystallinity. The grain boundary conductivity was about one to two orders of magnitude lower than the respective bulk conductivity, with higher values for the PLD grown layers. No separation of grain bulk

and grain boundary impedance was possible for YSZ films on STO. Also a surprisingly large total conductivity with significantly different activation energies was measured.

Lateral oxygen tracer diffusion coefficients were recorded by use of a novel two-step experiment, which consists of a tracer incorporation step at lower temperatures and a subsequent diffusion step in ultra high vacuum (UHV) at higher temperatures. This allowed the measurement of well defined diffusion profiles, which could be analytically evaluated. The films on sapphire and magnesia exhibited good agreement between effective transport properties of impedance and tracer measurements. The high conductivity of the YSZ layers on STO could be unambiguously attributed to conduction in the substrate, as the tracer diffusion coefficients were in the same range as those for YSZ on alumina. In all cases, the tracer diffusion experiments did not show any significant increase of oxygen diffusion along a free YSZ surface compared to a Pt|YSZ interface.

# Kurzfassung

Dünne Schichten aus mit Yttriumoxid stabilisiertem Zirkoniumdioxid (YSZ) wurden auf Magnesiumoxid (MgO), Saphir und Strontiumtitanat (STO) Einkristallen mittels gepulster Laserdeposition (PLD) und nach einer Sol-Gel Methode hergestellt. Von diesen dünnen Filmen wurde die laterale Korngröße, sowie deren Schichtdicke mittels Rasterkraftmikroskopie (AFM) bzw. mit digital holographischer Mikroskopie gemessen. Die Kristallinität und Textur wurde mit Röntgenbeugung (XRD) bestimmt. Der Fokus der vorliegenden Arbeit lag aber auf den Massen- und Ladungstransporteigenschaften durch Kornvolumen und Korngrenzen dieser Filme, welche mit Impedanzspektroskopie sowie mit Tracerdiffusion und anschließender Analyse durch Flugzeit Sekundärionenmassenspektrometrie (TOF-SIMS) gemessen wurden.

Im Zuge der Untersuchungen wurde eine verbesserte Elektrodengeometrie entwickelt um ionenleitende Dünnschichten mit Impedanzspektroskopie zu messen. Es stellte sich heraus, dass lange und schmale Elektroden mit kleinem Abstand, die kammförmig angeordnet sind, die Kornvolumen- und Korngrenzimpedanz selbst in sehr dünnen Schichten trennen können. Die Ergebnisse zeigten, dass die mit PLD und nach der Sol-Gel Methode hergestellten YSZ Dünnschichten eine Kornvolumenleitfähigkeit sehr ähnlich der von makroskopischen Polykristallen aufweisen, während die Schichten auf Magnesiumoxid eine niedrigere Leitfähigkeit besitzen, was mit der geringeren Kristallinität erklärt wer-

den kann. Die Korngrenzleitfähigkeiten waren ein bis zwei Größenordnungen niedriger als die entsprechenden Kornvolumenleitfähigkeiten, wobei die mittels PLD hergestellten Schichten etwas höhere Werte zeigten. In den YSZ Schichten auf STO konnte keine Trennung von Korn- und Korngrenzleitfähigkeit erreicht werden. Zusätzlich zeigten die Proben mit diesen Schichten eine erstaunlich hohe Gesamtleitfähigkeit und signifikant unterschiedliche Aktivierungsenergien.

Eine neuartige zweistufige Methode zur Messung von lateralen Tracerdiffusionskoeffizienten mit  $^{18}\text{O}$  wurde entwickelt, welche aus dem Einbau des Tracergases bei niedriger und nachfolgender Diffusion bei erhöhter Temperatur besteht. Dadurch war es möglich wohldefinierte Diffusionsprofile zu messen, die mit analytischen Funktionen ausgewertet werden konnten. Für die YSZ Schichten auf Saphir und Magnesiumoxid stimmten die Messungen der Transporteigenschaften mit Impedanzspektroskopie und Tracerdiffusion sehr gut überein. Die hohe Leitfähigkeit der YSZ Schichten auf STO hingegen konnten zweifelsfrei einer parallelen elektronischen Leitung im Substrat zugewiesen werden, nachdem der Tracerdiffusionskoeffizient in diesen Schichten sehr gut mit den auf Saphir gemessenen Werten übereinstimmte.

# Introduction and State of Research

The topic of thin film ion conductors has drawn a lot of research interest in the last years [1–16, 16–26, 26–30, 30–38]. This is understandable, considering on the one hand their use as powerful model systems to study so called “nano-ionics” and thus materials properties only observable on the nanometer scale, also termed “true size effects” [1, 39]. On the other hand a possible use in several different applications like batteries, fuel cells, and sensors is discussed and partly even in early test stages [23, 26, 37].

Numerous studies focusing on different oxide film materials such as yttria stabilized zirconia (YSZ) [2, 10, 13, 14, 16–18, 20, 21, 23], gadolinium doped ceria (GDC) [7–9, 23, 40, 41], scandia stabilized zirconia (SSZ) [11, 11, 30, 41–43] and calcia stabilized zirconia (CSZ) [15, 29, 43, 44] have been published. Different preparation methods like pulsed laser deposition (PLD) [11–13, 18, 22–24, 26–28, 30, 32, 45, 46], magnetron [31] or electron-beam sputtering [20], chemical vapour deposition [2, 4] and sol-gel processing [16, 19, 47–50] on several substrate materials were employed with a variation of preparation parameters to produce films of different microstructure and thickness.

Due to the vast data a constriction of the scope of research is necessary, therefore, this thesis will focus on yttria stabilized zirconia. YSZ is a well known ceramic material, which, due to its hardness and excellent refractory characteristics, is used in an array

## 1 Introduction and State of Research

of applications including thermal barrier coatings [51–54], dental prostheses [55–58], ceramic knives and even jewellery. Of more relevance to the present work is that YSZ is also a fast oxygen ion conductor. This interesting property is, for example, used for detecting and quantifying oxygen gas in the so called  $\lambda$ -probe, which is routinely implemented in combustion engines to regulate the air to fuel ratio [59]. However, while the use of YSZ in an oxygen sensor is fairly standard nowadays, a lot of research is focussed on the development and optimization of solid oxide fuel cells (SOFC) e.g. Refs. [9, 20, 23, 60–69]. In an SOFC YSZ is implemented as an ion selective membrane separating the fuel gas from the oxygen: Oxygen ions can pass through the YSZ membrane, but electrons are forced to take a detour, thus creating a direct current, which can be used as a power source. A short treatise of the working principle of a solid oxide fuel cell can be found in chapter 2. It is evident that the membrane affects the internal resistance of such a fuel cell by impeding the oxygen ion diffusion, hence, a thin membrane is advantageous, which is an example for a trivial size effect. A kind of fuel cells with particularly thin membranes, partly of the order of 100 nm, are called micro-SOFCs and are regarded by some to be possible future alternatives for Li-ion batteries in small scale portable devices [23].

However, some studies on oxygen ion conduction in YSZ thin films reported effects beyond these trivial size effects, therefore, maybe, being examples for true size effects. Though finding comprehensive relations between film thickness, structure and ionic conductivity has not yet been possible, as different studies showed a variety of different results, which are partly even contradictory. For example some groups reported conductivity enhancements in nanoscale YSZ layers [3, 14, 38] compared to macroscopic data, which they explain by a fast ion conduction path along the substrate|layer region, as, in a thin layer, the volume fraction of the interface region increases the thinner the layer is prepared. A similar explanation was given for a reported increase in ionic diffusivity found in macroscopic YSZ, but with nano-crystalline grains by tracer diffusion experi-

## 1 Introduction and State of Research

ments [70, 71]. Likewise the authors claimed that the high density of grain boundaries promoted the diffusion of oxygen ions, which is a surprising claim since grain boundaries in YSZ are generally accepted to be blocking to transport of oxygen ions [31, 72–75]. These results, however, have been thoroughly refuted in Ref. [76], where no fast ion transport along grain boundaries could be found. The most spectacular experiment has been published in Ref. [77], where an incredible increase of eight orders of magnitude in ionic conductivity in YSZ|strontium-titanate (STO) hetero-layers was claimed to be found. Again, these findings led to vivid discussions and were doubted heavily [78, 79], especially since in Ref. [34] similar results in conductivity were interpreted differently as being mainly electronic in nature, as opposed to ionic. Only recently, even the feasibility of achieving significantly higher conductivity by tailoring interfaces has been challenged [80], as the more spectacular results could not be reproduced, or, as pointed out in Ref. [81], may be due to data misinterpretations by neglecting substrate conductivity. Nonetheless, important connections between crystallographic strain and changes in ionic conductivity have been revealed in a series of experiments on different multilayer systems in Refs. [15, 24, 29, 30]. There it was conclusively shown that a dilative crystallographic strain, i.e. a strain widening the interatomic distances, forced upon the YSZ layer by sandwiching it between materials with different lattice constants, facilitates oxygen ion transport by reducing interactions between the ions. The maximum possible increase in conductivity was estimated to be 2.5 orders of magnitude. The converse argument is also true: A compressive crystallographic strain decreases the ionic conductivity. In first theoretical studies using ab-initio simulations these results were confirmed and it was postulated that the beneficial effect on ion transport has a maximum at a strain value of about 4% [25, 82].

On the other end of the spectrum studies have found decreases in oxygen ion conductivity of thin film YSZ, usually from about one to four orders of magnitude [4, 23, 31, 38, 83]. This effect might be readily explained by blocking grain boundaries in the polycrystalline

## 1 Introduction and State of Research

layers, as has been suggested in Refs. [31, 74]. However, while separation of grain and grain boundary oxygen ion conductivity in YSZ using impedance spectroscopy is common in macroscopic samples [72, 73, 84, 85], the case is not so trivial for thin films and has so far been only achieved in thicker layers in Ref. [16].

The goals of this thesis is to gather more information on oxygen ion transport in thin films of yttria stabilized zirconia by using two main methods:

- By using electrical impedance spectroscopy and a special electrode configuration, it is aimed to resolve grain and grain boundary contributions even in thin YSZ layers and see if there are significant differences to macroscopic reference samples. The results are found in chapters 4, 5, and also in chapter 7.
- With  $^{18}\text{O}$  tracer diffusion experiments and time of flight secondary ion mass spectrometry, it is intended to find ways to overcome the experimental difficulties of measuring lateral tracer diffusion profiles in thin YSZ films and finally, to clarify whether or not fast oxygen ion diffusion is present at some YSZ|substrate interfaces. These results are summarized in chapters 6 and, more elaborately, in chapter 7.

Main parts of this thesis, especially chapter 4 and partly chapter 6 have already been published in Refs. [18] and [17] respectively. The results in chapters 5 and 7 are currently submitted to a journal. The author of this thesis was also strongly involved in studies using impedance spectroscopy on thin film YSZ on silicon wafers, which allowed simultaneous measurement of the in- and across plane conductivities of the YSZ layer. This work is currently considered for publication or in print [86], but not included in the present thesis.

## Theoretical Aspects

### 2.1 Solid oxide fuel cells (SOFC)

As opposed to a combustion engine driven generator, which only uses the heat of the reaction  $\Delta H_R$ , a fuel cell is a device that directly converts the energy from a chemical reaction  $\Delta G_R$  into an electric current, according to

$$-zFU = \Delta G_R = \Delta H_R - T\Delta S_R. \quad (2.1)$$

In eq. 2.1  $z$  denotes the number of electrons transferred in the elementary reaction,  $F$  the Faraday constant,  $U$  the cell voltage,  $T$  the absolute temperature and  $\Delta S_R$  the reaction entropy. In Fig. 2.1 a sketch of a solid oxide fuel cell is shown.

Oxygen is reduced on the right side at the cathode according to



and incorporated into the electrolyte at the electrolyte|cathode interface. The fuel, in

## 2 Theoretical Aspects

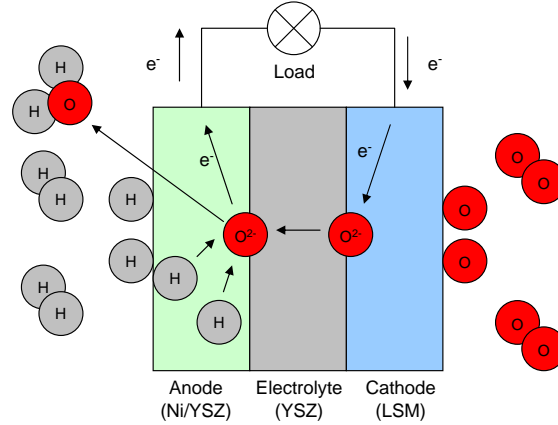


Figure 2.1: Sketch of a working solid oxide fuel cell (SOFC). While anode and cathode have to be conducting for both electrons and oxygen ions, it is imperative that the electrolyte is blocking to electronic current, otherwise there is an internal short circuit and the power output is decreased dramatically. Further information about the cermet Ni/YSZ and lanthanum strontium manganate (LSM) as examples for anode and cathode materials are found in [87–89]. Image modified from Ref. [90].

this case molecular hydrogen, is oxidized on the left side at the anode and then reacts with the oxygen ions to form water vapour:



Adding and adjusting eqs. 2.2 and 2.3 gives the well known oxyhydrogen reaction:



The standard potential  $E_0$  of eq. 2.4, which is equivalent to  $U$  in eq. 2.1 at standard conditions, amounts to 1.229 V at 25°C [91] and is the maximum open circuit voltage of a single cell under standard concentrations of all species. During operation of the fuel cell the open circuit voltage is reduced by several overpotentials, which can be assigned to different reaction steps in the individual parts of the fuel cell. Reducing these overpotentials is essential to optimizing the fuel cell and a key incentive in the

field of solid state ionics. An overview of research progress on cathode [88, 89], anode [87, 89, 92] and electrolyte [89, 93] performance can be found in recent reviews.

### 2.2 Defects in Solids

The model of an ideal crystal, consisting of an infinite number of irreducible elementary cells in all spatial dimensions, is often enough describe certain features of real samples like e.g. the crystal structure, or a valid simplification for ab initio calculations in theoretical chemistry. Nonetheless, very often deviations from this ideality enable properties impossible in a perfect crystal, with the most famous example probably being the p-n junction in semiconductors [94]. However, also ion conduction in solids is made possible by certain defects and impeded by others. Defects can be categorised by their spatial extension into 0-dimensional point defects like impurity atoms, vacancies or interstitials, 1-dimensional defects like linear dislocations and 2-dimensional defects like grain boundaries or interfaces [39]. Point defects, grain boundaries and interfaces in yttria stabilized zirconia are of key importance to this thesis and will therefore be treated in detail.

#### 2.2.1 Point defects

To unambiguously describe point defects in a crystal lattice the so called KRÖGER-VINK notation was introduced in Ref. [95]. It uses the naming scheme  $S_P^C$ , where  $S$  defines the species of the defect e.g. atoms or ions (Na, Al, . . .), electrons (e) or holes (h) and vacancies (V).  $P$  denotes the species, which in an ideal crystal would be at this lattice position, interstitial atoms or ions are marked with an i. Finally  $C$  represents the charge of the defect species relative to the species of an ideal lattice; relatively positive charges are denoted with a dot  $\bullet$ , relatively negative charges with a dash  $/$  and relatively neutral charges with an  $\times$ .

### Intrinsic Defects

Depending on the formation mechanism SCHOTTKY and FRENKEL disorders are distinguished. In Fig. 2.2 examples for these defect types are shown in a silver chloride single crystal. When an ion or atom changes from its lattice position to an interstitial one, for example



it is referred to as a FRENKEL disorder, see Fig. 2.2(b). A SCHOTTKY disorder is formed, when one or more ions change from the crystal bulk to the surface creating vacancies in the bulk, cf. Fig. 2.2(c). Even in a dislocation free single crystal of negligible impurity, point defects are formed due to entropic reasons. This is evident, when visualizing one mole of e.g. a silicon single crystal: There is exactly one perfect, i.e. defect free, arrangement of atoms, while only a single defect like an interstitial silicon atom ( $Si_i^{\times}$ ) would allow over  $10^{23}$  arrangements, which is obviously entropically favourable. However, for the formation of defects bondings have to be broken, therefore the concentration of defects has a maximum at a given temperature. The concentration of defects  $c_i$  formed by a reaction similar to 2.5 at the thermodynamic equilibrium can be quantified by:

$$\prod_i c_i = \exp\left(\frac{-\Delta G_D}{k_B \cdot T}\right) \prod_i n_i = \exp\left(\frac{-\Delta H_D}{k_B \cdot T}\right) \cdot \exp\left(\frac{\Delta S_D}{k_B}\right) \prod_i n_i \quad (2.6)$$

In eq. 2.6  $n_i$  denotes the volume concentration of the lattice positions involved, while  $\Delta G_D$ ,  $\Delta H_D$  and  $\Delta S_D$  are the thermodynamic parameters of the defect formation reaction and  $k_B$  being BOLTZMANN's constant.

### Extrinsic Defects

By doping an ionic crystal with aliovalent ions, extrinsic defects of opposite relative charge are created to maintain charge neutrality. For example, in the above silver chloride single crystal a divalent cadmium ion on a monovalent silver lattice position would have

## 2 Theoretical Aspects

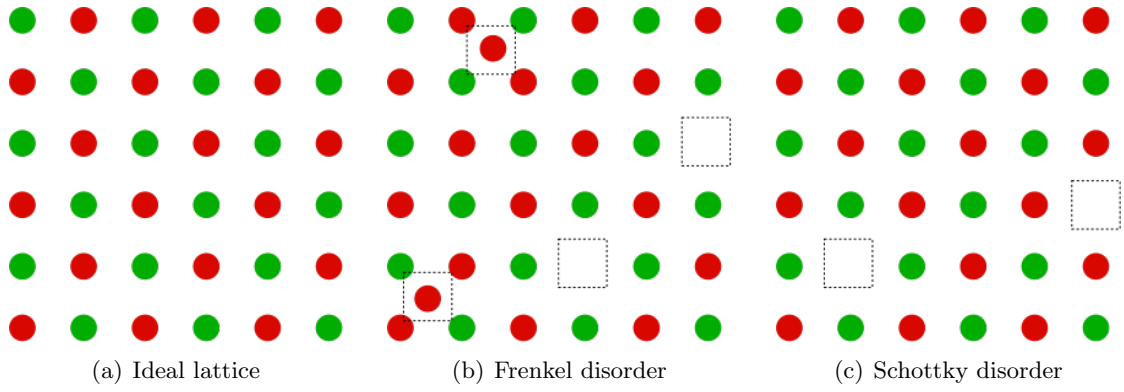
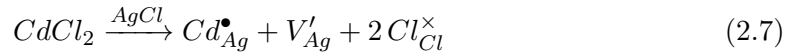


Figure 2.2: Intrinsic point defects visualized on the (100) plane of a cubic AgCl single crystal.  $\text{Ag}^+$  ions are represented by the red and  $\text{Cl}^-$  ions by the green dots. Images adapted from Refs. [96, 97]

to be compensated by an additional silver vacancy. The appropriate defect formation reaction therefore reads:



The concentration of extrinsic defects is fixed by the dopant concentration and unaffected by the temperature or the gas atmosphere.

### Non-stoichiometry

As opposed to intrinsic and extrinsic defects the so called non-stoichiometry accounts for defects formed by the solid crystal reacting to the surrounding gas atmosphere. For example in some oxides a pronounced stoichiometry change can be observed depending on the oxygen partial pressure. Tin oxide, for instance, shows an under-stoichiometric oxygen content at normal pressures [98]. This factor is accounted for by writing the chemical formula  $\text{SnO}_{2-\delta}$ , with  $\delta$  being the partial pressure depending parameter. Cobalt oxide, on the other hand, has more oxygen at normal pressure than is apparent from its

## 2 Theoretical Aspects

molecular formula [99, 100]. It is therefore referred to as over-stoichiometric oxide and written  $\text{Co}_{1-\delta}\text{O}$ .

The extent of the non-stoichiometry depends not only on the oxygen partial pressure, but also on the tendency of the cations in the crystals zu change their oxidation state, since excess positive or negative charges have to be compensated by some means. For instance, under-stoichiometric oxides compensate the excess positive charge by partial reduction of the metal cations, which is equivalent to electrons being transferred into the conduction band ( $CB$ ). The formation of such an oxygen vacancy in an oxide of type  $\text{MO}_{1-\delta}$  is described by:



Therefore non-stoichiometric ionic defects are compensated by electronic defects. Since “hard” ions like  $\text{Mg}^{2+}$  or  $\text{Al}^{3+}$  cannot change their valence easily, almost no non-stoichiometry is observed in their oxides. Other oxides, however, with “softer” cations like  $\text{Ce}^{4+}$  or  $\text{Mn}^{2+}$  can have an oxygen non-stoichiometry in the percent range [101–103].

Using the mass action law on eq. 2.8 it can be shown that the concentration of oxygen vacancies created by non-stoichiometry depends on the oxygen partial pressure  $p$  by:

$$[V_O^{\bullet\bullet}] = \frac{1}{2} [e'_{CB}] = \sqrt[3]{\frac{K_\delta}{4}} (p_{O_2})^{-\frac{1}{6}} \quad (2.9)$$

From eq. 2.9 it is evident that the concentration of non-stoichiometric oxygen vacancies is proportional to  $p^{-\frac{1}{6}}$ , with  $K_\delta$  being the equilibrium constant of the reaction in eq. 2.8. Similar considerations for an over-stoichiometric oxide of type  $\text{M}_{1-\delta}\text{O}$  yield a concentration dependence of  $p^{+\frac{1}{6}}$  for the formation of cation vacancies:

$$[V_M''] = \frac{1}{2} [h_{VB}^\bullet] = \sqrt[3]{\frac{K'_\delta}{4}} (p_{O_2})^{+\frac{1}{6}} \quad (2.10)$$

### BROUWER diagrams

An easy way to represent the partial pressure dependence of the concentrations of the electronic or ionic point defects in crystals are the isothermal BROUWER diagrams. An example of such a diagram for an undoped metal oxide of type  $\text{MO}_{1-\delta}$  is shown in Fig. 2.3(a). The defect concentrations are plotted against the oxygen partial pressure both in logarithmic scale. Depending on the defect with the highest concentration, the majority charge carriers, different pressure regimes can be defined. The intrinsic SCHOTTKY disorders ( $V_{\text{O}}^{\bullet\bullet}$  and  $V_{\text{M}}''$ ) dominate in region II of Fig. 2.3(a), but in region I and III the non-stoichiometry prevails: The low oxygen partial pressure in region I facilitates the formation of oxygen vacancies and electrons according to the mechanism in eq. 2.9, while the high oxygen partial pressure favours the defects formed in eq. 2.10. This diagram is valid for an over- and under-stoichiometric metal oxide, however, the exact boundaries of the pressure regimes obviously differ. For example at ambient pressure  $\text{Co}_{1-\delta}\text{O}$  would be in regime III, while  $\text{ZnO}_{1-\delta}$  would be in region I.

In Fig. 2.3(b) a BROUWER for a negatively doped metal oxide of type  $\text{MO}_{1-\delta}$  is plotted. The regions at the extremely low or high oxygen partial pressures I and IV have the same characteristics and majority charge carriers as regions I and III in Fig. 2.3(a). Region II, however, is dominated by the extrinsic oxygen vacancies introduced by the negative doping, the intrinsic defect concentration is considered to be negligible in comparison. In region III the high oxygen partial pressure has consumed all extrinsic vacancies, which can only be charge compensated by holes in the valence band.

### 2.2.2 Mass and charge transport

The aforementioned electronic and ionic point defects are the basis for mass and charge transport in ionic crystals, therefore it is appropriate to give a short introduction into the driving forces of these transport phenomena.

2 Theoretical Aspects

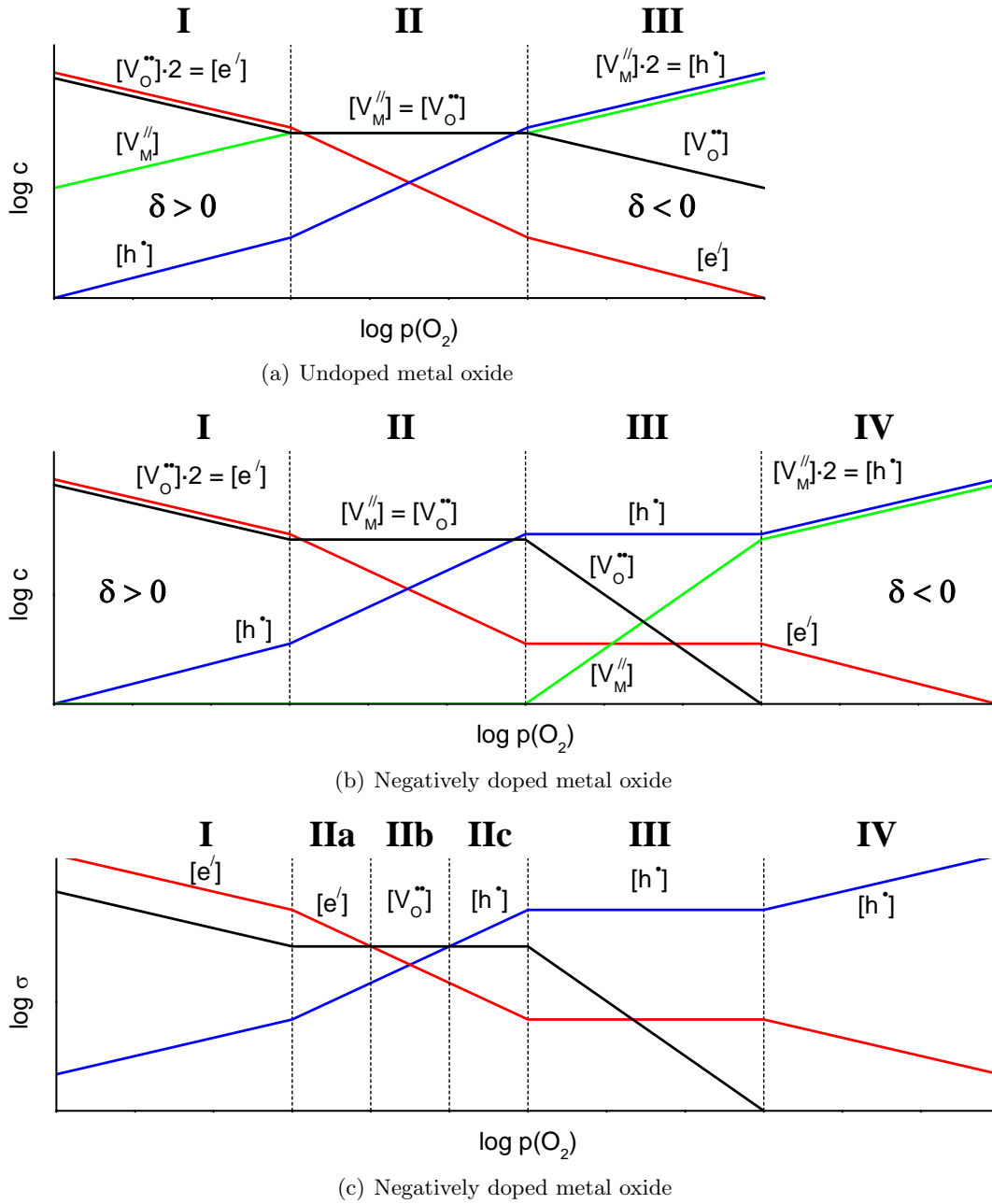


Figure 2.3: BROUWER diagrams of the point defect concentrations for an (a) undoped and (b) a negatively doped metal oxide of type  $\text{MO}_{1-\delta}$ . In (c) the conductivities of the point defects of the metal oxide in (b) are plotted. Images adapted from Ref. [101].

## 2 Theoretical Aspects

The chemical potential  $\mu$  of a particle describes its tendency to change place or react. For a general particle  $k$  it is defined by [39]

$$\mu_k = \mu_0 + k_B \cdot T \ln(c_k) \quad (2.11)$$

with  $\mu_0$  being the chemical potential under standard conditions and  $c_k$  the concentration of  $k$ . For large concentrations the standard chemical potential also becomes concentration dependent (and  $c_k$  in eq. 2.11 is replaced with  $\frac{c_k}{1-c_k}$ ), but it is common practice to rather substitute the concentration term  $c_k$  with an activation term  $a_k$  and leave  $\mu_0$  unchanged.

Since an electric field also affects a charged particles willingness to move or react, eq. 2.11 can be generalized to define the so called electrochemical potential  $\tilde{\mu}_k$ :

$$\tilde{\mu}_k = \mu_k + z_k \cdot e \cdot \varphi \quad (2.12)$$

In eq. 2.11  $z_k$  denotes the charge number,  $e$  the elementary charge and  $\varphi$  the electric potential. In equilibrium the electrochemical potential is spatially constant. If this equilibrium is disturbed, particles flow until equilibrium is reached again. This particle flow  $J_k$  is described by the generalized transport equation:

$$J_k = -\frac{\sigma_k}{z_k^2 e^2} \nabla \tilde{\mu}_k \quad (2.13)$$

with  $\sigma$  denoting the conductivity and

$$\nabla \tilde{\mu}_k = \nabla \mu_k + z_k \cdot e \cdot \nabla \varphi \quad (2.14)$$

With eqs. 2.13 and 2.14 two border cases can be distinguished. If the gradient of the

## 2 Theoretical Aspects

chemical potential in eq. 2.14  $\nabla\mu_k = 0$ , then the only remaining driving force is the electric field  $\nabla\varphi$ . Using the definition of the electric current density  $j_k$

$$j_k = z_k \cdot e \cdot J_k \quad (2.15)$$

OHM's law of electric conduction can be derived:

$$\sum_k j_k = j = -\sigma \cdot \nabla\varphi \quad (2.16)$$

However, if in eq. 2.14  $\nabla\varphi = 0$  only a gradient in the chemical potential can cause mass and charge transport. Therefore eq. 2.13 changes to

$$J_k = -\frac{\sigma_k}{z_k^2 e^2} \nabla\mu_k = -\frac{\sigma_k}{z_k^2 e^2} (\nabla\mu_0 + k_B \cdot T \cdot \nabla \ln c_k) \quad (2.17)$$

In a homogeneous material  $\nabla\mu_0 = 0$  and  $\nabla \ln c_k = \frac{\nabla c_k}{c_k}$ , therefore eq. 2.17 becomes

$$J_k = -\frac{k_B \cdot T \cdot \sigma_k}{z_k^2 e^2 c_k} \nabla c_k = -D_k \cdot \nabla c_k \quad (2.18)$$

which is FICK's first law of diffusion [104, 105] with the diffusion coefficient  $D_k$ . The NERNST-EINSTEIN relation is also included in eq. 2.18 as rearranging yields

$$D_k = \sigma_k \cdot \frac{k_B \cdot T}{z_k^2 e^2 c_k} \quad (2.19)$$

which connects the conductivity of the species  $k$  with its diffusion coefficient.

### 2.2.3 Conductivity

A different representation of eq. 2.19 at a constant temperature reads

$$\sigma_k = z_k \cdot e \cdot u_k \cdot c_k \quad (2.20)$$

## 2 Theoretical Aspects

with the mobility  $u_k$  defined by

$$u_k = \frac{D_k \cdot z_k \cdot e}{k_B \cdot T} \quad (2.21)$$

The mobility of electronic defects is considerably higher than that of ionic point defects. Thus, the BROUWER diagram in Fig. 2.3(b) can be changed to plot the conductivity rather than the concentration of the charge carriers, which is shown in Fig. 2.3(c). Region II in Fig. 2.3(b), where the majority charge carriers are the extrinsic oxygen vacancies, is divided in three subregions. In regions IIa and IIc the current is mainly electronic and transported by electrons or holes respectively, while in region IIb the current is transported by the abundant oxygen vacancies. However, the charge compensation in region II is still overwhelmingly achieved by the oxygen vacancies.

In solid crystals ions changing position have to overcome an energy barrier [39]. The height of this barrier can be considered as the activation energy  $E_a$  of the transport reaction of the ion moving to a neighbouring lattice position. The temperature dependence of the success of such a reaction is of ARRHENIUS-type, and therefore the temperature dependence of the conductivity, with  $\sigma_0$  being the pre-exponential factor, reads

$$\sigma_k = \sigma_0 \cdot \exp\left(-\frac{E_a}{k_B \cdot T}\right) \quad (2.22)$$

for solids with constant charge carrier concentrations in the investigated temperature regime. The activation energy is often extracted from so called ARRHENIUS-plots, where the logarithmic conductivity is plotted against the inverse absolute temperature. By measuring conductivity values at several temperatures a linear curve with a slope of  $-E_a/k_B$  can be fitted, see e.g. Fig. 4.8 in chapter 4.

## 2.3 Defect chemistry in YSZ

### 2.3.1 Yttria doping

Depending on the temperature, zirconium dioxide crystallizes in different structures as the phase diagram in Fig. 2.4 shows. The cubic phase in pure zirconia is only stable above about 2400°C, but the transformation temperature decreases rapidly with increasing yttria content. The YSZ layers and macroscopic polycrystals studied in the present thesis have an yttria level of approximately 8 mol%. At this doping level the cubic phase is still thermodynamically unstable at room temperature, but can be frozen in by quenching the sample fast enough. Therefore this state is considered kinetically stable, hence the name yttria *stabilized* zirconia. Cubic YSZ crystallizes in the fluorite structure like CaF<sub>2</sub> with the Zr<sup>4+</sup> ions in a face-centered cubic lattice with the O<sup>2-</sup> ions in the tetrahedral positions, thus constituting a primitive cubic lattice. The lattice parameter of cubic YSZ has been determined to be 0.514 nm [106]. The crystal structure of cubic YSZ and a representation of the yttria doping process is pictured in Fig. 2.5.

Besides stabilizing the cubic phase, the trivalent yttrium ions on the lattice positions of the tetravalent zirconium ions also introduce oxygen vacancies. Using the KRÖGER-VINK notation this defect formation reaction can be written as



and exemplifies a formation of extrinsic vacancies through negative doping by the lesser positive Y<sup>3+</sup> ions. In ambient air YSZ is in region II of the BROUWER diagram in Fig. 2.3(b) and region IIb of Fig. 2.3(c), hence, in the pressure regime where oxygen vacancies are the majority charge carriers and also conduct the current, while having a negligible electronic defect concentration. These properties make YSZ an ideal candidate for an electrolyte in a solid oxide fuel cell, as the high oxygen vacancy concentration ensures a high ionic conductivity and ion mobility at elevated temperatures, thus reducing

## 2 Theoretical Aspects

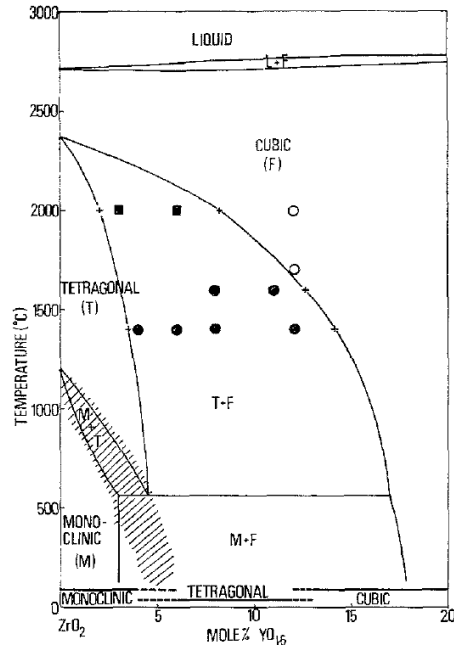


Figure 2.4: Phase diagram of YSZ in the zirconia rich portion of the zirconia-ytria system. Note that the x-axis indicates the mole percent of  $\text{YO}_{1.5}$  rather than  $\text{Y}_2\text{O}_3$ . Non-equilibrium homogeneous phases are indicated at the lower margin. The symbols indicate phases found at room temperature: Open circles for the cubic, filled circles for the tetragonal and squares for the monoclinic phase. The hatched region indicates a non-equilibrium monoclinic-tetragonal transition, see image source in Ref. [107].

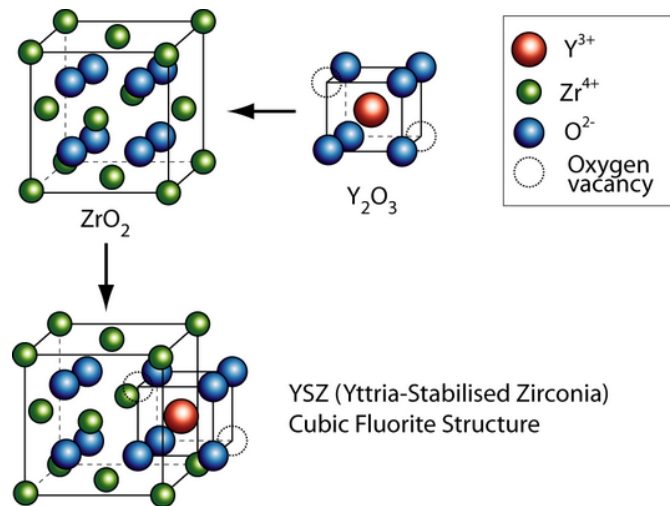


Figure 2.5: Fluorite type crystal structure of cubic zirconia and a graphic visualization of the generation of oxygen vacancies by yttria doping. Image source: Ref. [108]

the internal resistance of the SOFC. Additionally, the virtually non-existent electronic defects avoid a short circuit of the electronic current, see Fig. 2.1. The latter is a problem in some other potential electrolytes like gadolinium doped cerium oxide (GDC) at higher temperatures and low oxygen partial pressures [93].

### 2.3.2 Grain boundaries

In polycrystalline YSZ grain boundaries represent areas of structural mismatch between neighbouring YSZ grains. This relatively narrow zone, with an extension of roughly the length of one or two elementary cells of YSZ, is often called the crystallographic grain boundary or grain boundary core [39, 85, 102, 109, 110]. The different chemical surroundings in this grain boundary core causes an enrichment of oxygen vacancies and also of the yttrium dopant ions. However, the segregation of yttrium to the grain boundary core is found to be insufficient to charge balance the excess oxygen vacancies. Thus, a positively charged grain boundary core is created, which in turn is charge compensated by a depletion of oxygen vacancies in the adjacent regions inside both grains [109]. This space charge region of lower oxygen vacancy concentration plus the grain boundary core is called the electrical grain boundary. Nonetheless, from a crystallographic point of view the space charge region is part of the grain bulk. A sketch of the oxygen vacancy concentration profile across an individual grain boundary can be found in Fig. 2.6. The depletion of the concentration of the oxygen vacancies, which constitute the majority charge carriers, leads to a lower ionic conductivity, cf. eq. 2.20, in the space charge regions of the grain boundaries compared to the undisturbed bulk regions of polycrystalline YSZ. Therefore it is sensible to distinguish between a bulk and grain boundary conductivity, or resistivity in YSZ.

Besides the grain boundary space charge regions, caused by oxygen vacancy accumulation in the grain boundary core, a second mechanism impeding ionic current flow across grain boundaries in YSZ of low purity has to be considered. A major impurity

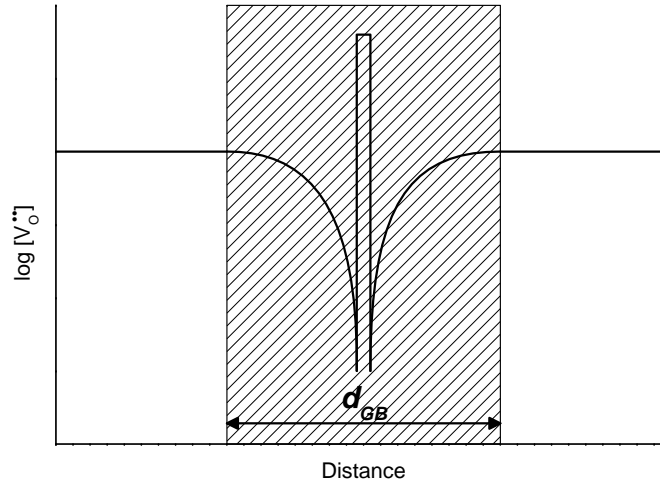


Figure 2.6: Schematic representation of the oxygen vacancy concentration change across a grain boundary in YSZ according to Ref. [85]. The shaded region highlights the grain boundary space charge region with the electric grain boundary width  $d_{GB}$ .

in YSZ, besides alkali and some transition metal ions, is silicon dioxide [85]. During the sintering process these impurities aggregate at the grain boundaries, most favoured are junctions of three grains, constituting a siliceous phase, which is highly blocking to oxygen ions. Therefore, this siliceous phase reduces the contact area between the grains which has been shown to create an additional so called current constriction resistance [111]. This type of grain boundary resistance is obviously more prevalent in crystals with larger individual grains, as less grain boundaries are present there. Hence, the impurity concentration is higher in an individual grain boundary. Measurement of grain bulk and grain boundary resistance in YSZ thin films is a major topic in this thesis, especially in chapter 4.

## 2.4 Phenomenological diffusion coefficients

The diffusion coefficient of a charged mobile species, as implied in eq. 2.19, sometimes termed “microscopic” diffusion coefficient [39], is impossible to measure directly. How-

## 2 Theoretical Aspects

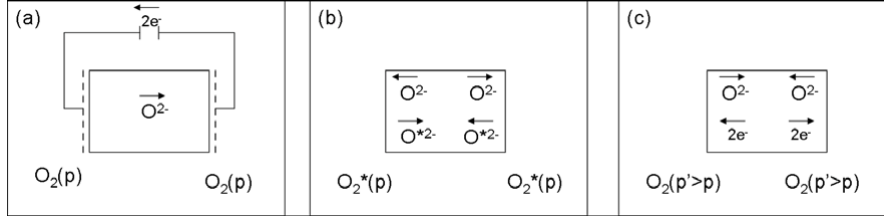


Figure 2.7: Schematic representations of measurements of phenomenological diffusion coefficients according to Ref. [39]: (a) conductivity experiment, (b) tracer exchange experiment, (c) partial pressure change experiment.

ever, there exist several methods allowing to record “macroscopic”, or phenomenological diffusion coefficients, which are connected to this otherwise inaccessible parameter. In Fig. 2.7 the three principal experimental approaches to measure these “macroscopic” diffusion coefficients are sketched and will be discussed in the following sections.

### 2.4.1 Conductivity based diffusion coefficient

In the experiment sketched in Fig. 2.7(a) the conductivity of an oxide ion conducting material is measured. For a successful experiment it is crucial to keep the total current small to maintain linearity in the current-voltage correlation and also not to change the sample stoichiometry. Further prerequisites are reversible electrodes and obviously negligible electronic current in the investigated sample. Some of these experimental confinements can be circumvented by using electrical impedance spectroscopy to directly extract the conductivity of the sample under investigation, without having to worry about electrode effects.

The conductivity can be converted into a diffusion coefficient using eq. 2.19, with the concentration of the charge carrier being equal to the volume concentration of oxygen  $c_{O^{2-}}$  in the sample. By not using the concentration of the mobile species, which are, depending on the predominant charge transport mechanism, the oxygen vacancies or interstitial oxygen ions, but the total oxygen concentration, an average diffusion coefficient for the whole oxygen assemble is calculated, which is sometimes also termed the self

## 2 Theoretical Aspects

diffusion coefficient [39]. In this thesis the self or conductivity based diffusion coefficient will be referred to by  $D^\sigma$ . With the knowledge of the concentration of the mobile point defects in the oxygen lattice  $c_k$ , one can easily convert the self diffusion coefficient into the defect diffusion coefficient  $D_k$  by

$$D^\sigma = \frac{c_k}{c_{O^{2-}}} D_k \quad (2.24)$$

with  $D_k$  obviously being a significantly larger value. In YSZ the oxygen vacancy concentration is extrinsically fixed by the yttria doping, hence, with the assumption that virtually all oxygen vacancies are mobile, a calculation of the defect diffusion coefficient is possible. However, for the sake of convention and comparability only  $D^\sigma$  was calculated, while the values for  $D_k$  are not explicitly given in this thesis, see for example chapters 6 and 7.

### 2.4.2 Tracer diffusion coefficient

The tracer diffusion coefficient is usually measured by annealing the sample of interest for a specific time in an atmosphere of tracer enriched gas, for oxide ion conductors mainly  $^{18}\text{O}_2$ , as sketched in Fig. 2.7(b). Subsequently, a tracer diffusion depth profile is recorded by an isotope sensitive analysis method, e.g. secondary ion mass spectrometry (SIMS). The driving force of the tracer exchange is the configurational entropy, i.e. the concentration difference of the tracer in the gas phase and in the sample. In contrast to the conductivity based diffusion coefficient  $D^\sigma$  the tracer diffusion coefficient  $D^*$  is derived from a pure diffusion process. These two diffusion coefficients are interconnected by the following correlation [39, 112, 113]

$$D^* = H_R \cdot D^\sigma \quad (2.25)$$

## 2 Theoretical Aspects

with  $H_R$  being the so called HAVEN ratio. The tracer diffusion coefficient is usually slightly smaller than the self diffusion coefficient, even though basically the same process is monitored. This is due to a preferred “backwards” orientation of tracer diffusion: In an ion conducting oxide with the charge transport being mainly carried out by vacancy diffusion, as is the case in stabilized zirconia, after a successful jump of a tracer ion, the next vacancy is usually not available right away. Therefore, the next jump of the tracer ion is likely to be into the vacancy it just created, i.e. the lattice position it came from, given that it has not been already occupied in the meantime. This correlation factor can be exactly calculated and has the value of 0.65 for a primitive cubic lattice [39], which is the structure of the oxygen sublattice in YSZ. However, the HAVEN ratio also accounts for other effects that might cause differences in the tracer and conductivity experiment. Nonetheless, in reality the measurement accuracy of tracer diffusion experiments is often such that  $H_R = 1$  is a very reasonable approximation. In chapters 6 and 7 new methods of tracer diffusion experiments are described along with a detailed description of experimental setup and evaluation of the results.

### 2.4.3 Chemical diffusion coefficient

The chemical diffusion coefficient describes the diffusion process taking place when exposing a, for example, oxide ion conducting sample to a different oxygen chemical potential, as sketched in Fig. 2.7(c). The driving force in this experiment is the gradient of the oxygen partial pressure, which causes changes in the non-stoichiometry and therefore in the point defect concentrations, see Fig. 2.3. A typical experiment might consist of equilibrating a sample with intrinsically governed point defects in one oxygen partial pressure, then rapidly changing the atmosphere and measuring the conductivity relaxation of the sample [39]. Since a concentration variation of non-stoichiometric defects requires both electronic and ionic defects, see e.g. eq. 2.8, a mixture of both transport properties is probed in such an experiment.

The chemical diffusion coefficient is not of interest in the practical part of this thesis, but is mentioned here shortly for the sake of completeness.

## 2.5 Impedance Spectroscopy

### 2.5.1 Impedance spectra

The impedance  $Z$  is defined by OHM's law as

$$Z = \frac{U(t)}{I(t)} \quad (2.26)$$

with  $U(t)$  and  $I(t)$  being the alternating voltage and current respectively at a known frequency, which are flowing through  $Z$ . Hence, impedance spectroscopy is the frequency resolved recording of complex impedances by applying a voltage signal to a system and measuring the resulting current. The input voltage signal can be a step signal or even white noise, both of which require the output current signal to be FOURIER transformed to extract the frequency spectrum from the time dependent response [114]. However, the most commonly used experimental approach is to measure directly in the frequency domain, by consecutively applying single frequency sinus voltages and measuring the amplitudes and phase shifts of the current response. Therefore, with the knowledge of the amplitude of the input voltage  $\hat{U}$  and by measuring the amplitude of the responding current  $\hat{I}$  as well as the phase shift  $\varphi$ , the complex impedance can be calculated:

$$\frac{\hat{U}}{\hat{I}} \cdot \exp(i \cdot \varphi) = Z = Z' + i \cdot Z'' \quad (2.27)$$

In eq. 2.27 the complex impedance  $Z$  is also split into its real part  $Z'$  and imaginary part  $Z''$ . Plotting several of these vectors recorded at different angular frequencies  $\omega$  in the complex plane creates the so called NYQUIST or impedance plot [114, 115], see for

example Fig. 4.7(a). An alternative way of representing such an impedance spectrum is the modulus plot. The complex modulus of the impedance can be calculated by

$$M = i \cdot \omega \cdot Z \quad (2.28)$$

While containing the same information as the NYQUIST plot, the modulus plot highlights different features of the impedance spectrum, an example for a modulus plot is found for instance in Figs. 2.8(b) and (d).

### 2.5.2 Equivalent circuits

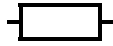
In solid state chemistry impedance spectra are usually interpreted by means of an equivalent circuit. This circuit is constructed by virtually arranging electronic components in such a way that a simulated impedance spectrum recorded on this circuit resembles the data from the actual measured one. A well designed equivalent circuit does not only create a good fit to the measured data, but also allows to interpret each electronic component as a specific process in the sample. A list of the electronic components and their impedances used in this thesis along with possible mechanistic interpretations is given in Table 2.1.

#### The single RC-circuit

Direct current in a solid electrochemical cell induces a faradayic reaction or a transport process as the movement of oxygen ions in YSZ. Alternating current of high frequencies, on the other hand, is transported by dielectric polarization of immobile charge carriers like valence electrons or the anion and cation sub-lattices. At intermediate frequencies both of these processes overlap, hence, the equivalent circuit describing such a process is a parallel arrangement of a resistor and a capacitor, often called an RC-element or

## 2 Theoretical Aspects

Table 2.1: Short list and description of electronic components used to design equivalent circuits to fit impedance data recorded in this thesis. CPE is an acronym for Constant Phase Element.

Component	Symbol	Impedance	Interpretations
Resistor $R$		$Z_R = R$	Ionic conduction in YSZ bulk or grain boundaries or charge transfer at electrodes. $R$ is the resistance in Ohms.
Capacitor $C$		$Z_C = \frac{1}{i\omega C}$	Dielectric polarization of electrons and ions in YSZ or the double layer capacitance of the SCHOTTKY barrier at the electrodes. $C$ is the capacitance in Farad.
CPE $CPE$		$Z_{CPE} = Q^{-1} (i \cdot \omega)^{-r}$	The Constant Phase Element is used to model non-ideal capacitors, for $r = 1 - \epsilon$ where ( $0 < \epsilon \leq 0.3$ )

VOIGT's structure [114, 115], see inset in Fig. 2.8(a). It is commonly known that parallel impedances add up according to

$$Z_{RC} = \left( \frac{1}{Z_R} + \frac{1}{Z_C} \right)^{-1} = \frac{R}{1 + i \cdot \omega \cdot C \cdot R} \quad (2.29)$$

with usage of the symbols in Table 2.1. Separating of the real and complex part in eq. 2.29 yields

$$Z_{RC} = \frac{R}{1 + \omega^2 P^2} - i \frac{\omega \cdot R \cdot P}{1 + \omega^2 P^2} \quad (2.30)$$

with the time constant  $P = R \cdot C$ . The NYQUIST plot of 2.30 resembles a semi-circle which emerges at high frequencies from the origin and intercepts the x-axis at  $\omega = 0$  with a diameter of  $R$ , see Fig. 2.8(a). At the maximum of the imaginary component, the peak frequency

$$\omega_{Peak} = \frac{1}{P} = (R \cdot C)^{-1} \quad (2.31)$$

exactly half of the current is transported through the resistor and the capacitor each. The value of  $\omega_{Peak}$  is an important property to characterise an RC-element.

## 2 Theoretical Aspects

Conversely, the complex modulus of above equivalent circuit according to eq. 2.28 is

$$M_{RC} = \frac{\omega^2 \cdot R \cdot P}{1 + \omega^2 P^2} + i \frac{\omega \cdot R}{1 + \omega^2 P^2} \quad (2.32)$$

In the modulus plot eq. 2.32 also creates a semi-circle, as shown in Fig. 2.8(b). However, this time the low frequencies are close to the origin and the axis intercept is at  $\frac{1}{C}$  at  $\omega = \infty$ , which can easily be shown as follows:

$$\lim_{\omega \rightarrow \infty} M_{RC} = \frac{\omega^2 \cdot R \cdot P}{\omega^2 P^2} = \frac{\omega^2 \cdot R^2 \cdot C}{\omega^2 \cdot R^2 \cdot C^2} = \frac{1}{C} \quad (2.33)$$

In conclusion a single RC-element excellently describes the impedance response for a YSZ single crystal over a large frequency range. However, electrode and grain boundary contribution have been neglected so far.

### Multiple RC-circuits

As already noted above, in polycrystalline YSZ grain boundaries constitute an impediment to the current flow and have to be accounted for by an additional resistance  $R_{GB}$  in series to the bulk resistor  $R_{Bulk}$ . Consequently, an additional capacitor  $C_{GB}$  representing the dielectric loss over the grain boundaries is also introduced, see inset in Fig. 2.8(c). The impedance of this equivalent circuit is described analogous to eq. 2.30:

$$Z_{2RC} = \frac{R_{Bulk}}{1 + \omega^2 P_B^2} - i \frac{\omega \cdot R_{Bulk} \cdot P_B}{1 + \omega^2 P_B^2} + \frac{R_{GB}}{1 + \omega^2 P_{GB}^2} - i \frac{\omega \cdot R_{GB} \cdot P_{GB}}{1 + \omega^2 P_{GB}^2} \quad (2.34)$$

If the time constants, or peak frequencies, of both processes are sufficiently different, two well separated consecutive semi-circles are found in the impedance plot. The diameters of each semi-circle represent  $R_{Bulk}$  and  $R_{GB}$  respectively, as is discussed in Fig. 2.8. While the resistances of YSZ bulk and grain boundaries are usually at most one or two orders of magnitude apart [85], the capacitances often differ over a much larger range,

## 2 Theoretical Aspects

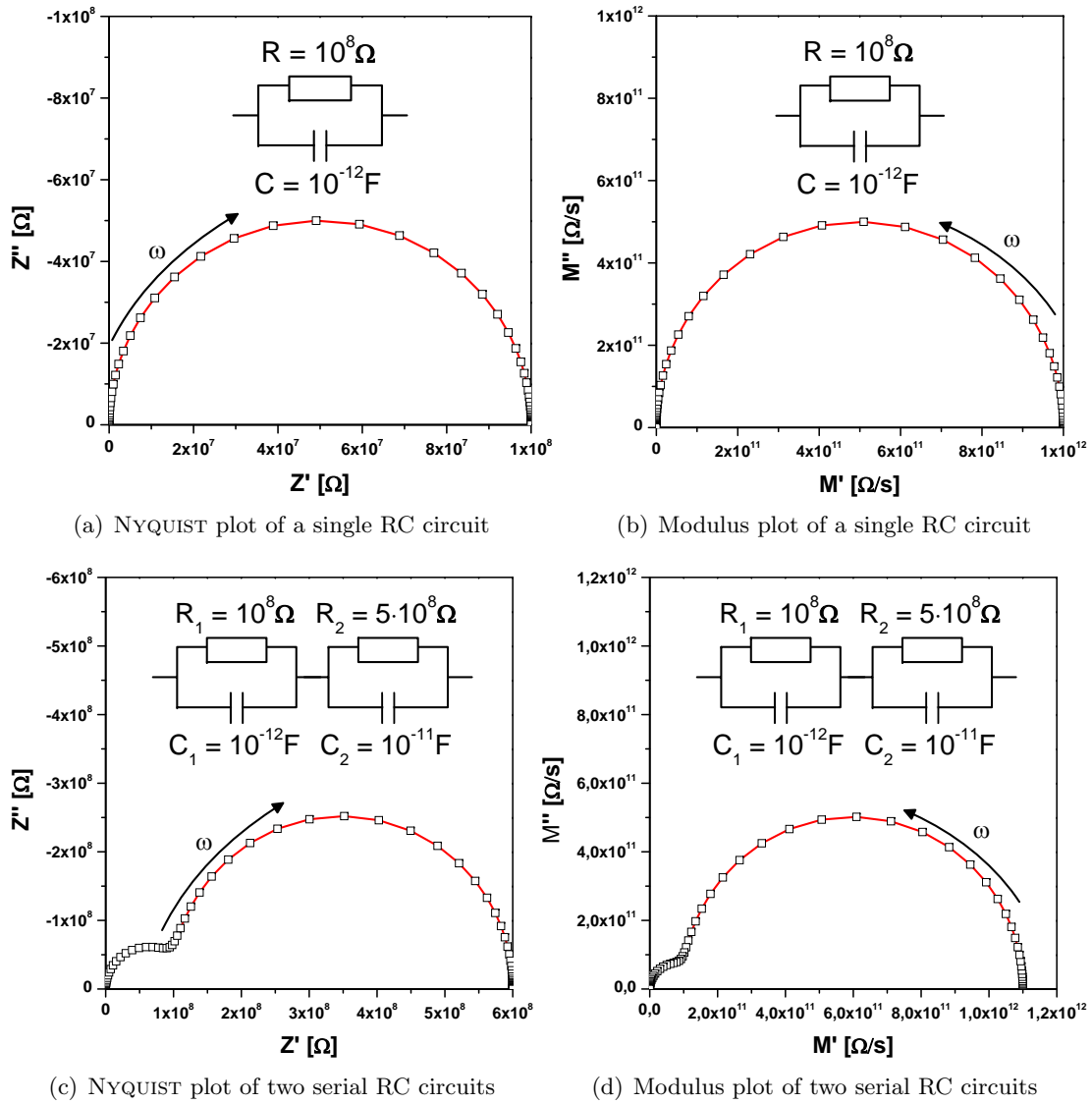


Figure 2.8: Graphical representations of impedance data in NYQUIST (a),(c), and modulus plots (b), (d). The equivalent circuits with their respective values are given in each diagram, the arrow denotes the direction of decreasing frequency. Note how the diameters of the semi-circles in the NYQUIST plots in (a) and (c) directly represent a resistance in the equivalent circuit. In the modulus plot in (b) the diameter of the semi-circle gives the inverse of  $C_1$ , while in (d) the rightmost intercept is equal to  $(C_1 + C_2)^{-1}$

## 2 Theoretical Aspects

as is shown in eq. 4.2 and 4.3. For similar time constants both semicircles would overlap with a diameter of  $R_{Bulk} + R_{GB}$ .

The effect of metal electrodes can, to a first approximation, be accounted for by introducing a third RC-element. As the electrode capacitance is very much larger than any other element, separation is no problem. For further information on the impedance of metal electrodes on YSZ detailed studies are found in Ref. [116, 117].

### Constant Phase Elements (CPE)

Above considerations do not acknowledge inevitable non-idealities of real samples. The grain boundary capacitance in polycrystalline YSZ can hardly be described by an ideal capacitor, but calls for the use of a constant phase element. The reason is that the grain boundary impedance response is in fact averaging over numerous individual grain boundaries, which are all similar, but slightly different in width and crystallographic disorder. Hence, the characteristic frequencies are also distributed around a mean value leading to a depressed semi-circle rather than an ideal one. This behaviour can be described by a constant phase element with an exponential factor  $r < 1$ , see Table 2.1. On the other hand, if each transport step is indiscernible from the other, a very narrow distribution of the peak frequencies and therefore an ideal semi-circle results.

### 2.5.3 The charge transfer resistance

In the practical execution of an impedance measurement one also has to choose the probing voltage wisely. Assuming the absence of a diffusion limitation, each individual transport step, i.e. the hop of an oxygen ion into a neighbouring vacancy, has a current voltage relation described by the BUTLER-VOLMER equation [118]:

$$I = A \cdot j_0 \left( \exp \left( \frac{\alpha z e \eta}{k_B T} \right) - \exp \left( \frac{(1 - \alpha) z e \eta}{k_B T} \right) \right) \quad (2.35)$$

In eq. 2.35  $I$  denotes the cathodic or anodic electrode current,  $A$  the active surface area of the electrode and  $j_0$  the exchange current density; further the charge transfer coefficient  $0 < \alpha < 1$ , the elementary charge  $e$ , BOLTZMANN's constant  $k_B$  and finally the overpotential  $\eta = U - E_0$ . As no reaction is taking place in the transport of an oxygen vacancy the standard potential  $E_0$  is nil and  $\eta$  in eq. 2.35 is simply given by the external voltage per elementary step. A plot of eq. 2.35 is shown in Fig. 2.9.

The validity of an impedance measurement relies on a linear relation between imposed voltage and responding current, which is only the case in the vicinity of  $\eta = 0$ , as can be seen in Fig. 2.9. Luckily in the measurement of bulk effects the voltage drop is distributed over very many individual steps, hence, a non-linearity is virtually impossible. Similarly the transport steps in grain boundaries, while considerably fewer in numbers, are usually still plentiful enough to guarantee a linear relationship, see also chapter 3. However, studies on the non-linearity of grain boundaries in oxide ion conductors do exist [119, 120].

When studying electrode effects, where the rate limiting step, and therefore the largest resistance, can be the charge transfer step from the incorporation of the adsorbed gas [60, 116]. Hence, the whole voltage drop is over one elementary step only. Therefore, it is crucial not to choose a too large probing voltage.

## 2.6 Time of Flight Secondary Ion Mass Spectrometry (TOF-SIMS)

### 2.6.1 Introduction and principle of TOF-SIMS

Secondary ion mass spectrometry allows to measure qualitative ion distributions in the lateral direction as well as the recording of depth profiles. Therefore, it is a very powerful tool of surface analysis in different branches from material science to biology [121]. It relies on the principle that an impacting primary ion beam generates, beside un-

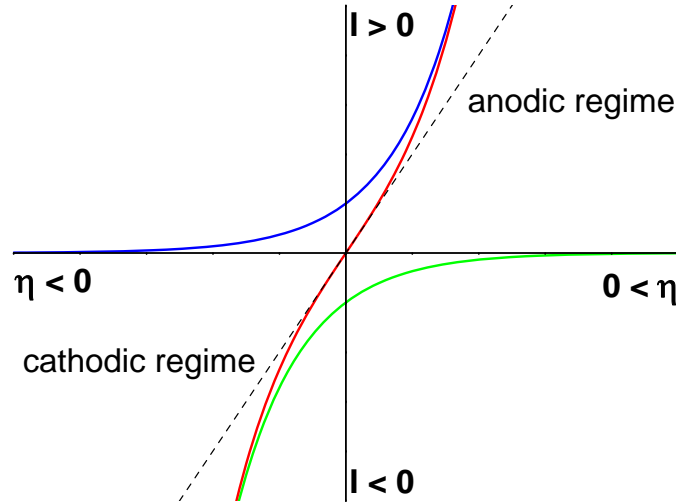


Figure 2.9: Graphic representation of the BUTLER-VOLMER equation in eq. 2.35. The blue line represents the anodic current in the first term, while the green one gives the cathodic current in the second term of eq. 2.35. The red line is the sum of both currents. The dashed black line is a linear approximation close to  $\eta = 0$ .

charged atoms and clusters, secondary ions which can be focused on a detector. Since the ionization probability of the different elements is heavily dependent on the matrix, quantification of SIMS data is difficult. However, in the present work SIMS is used to measure lateral  $^{18}\text{O}$  tracer concentration profiles, see eq. 2.37, which circumvents the aforementioned problem, as the ionization probability of  $^{16}\text{O}$  and  $^{18}\text{O}$  are the same.

The instrument used in this thesis is equipped with a detector, which separates the ion masses by their different flight times. A consequence of this mechanism is that the primary ion beam scanning the surface needs to be pulsed, or else a constant stream of ions would clog up the detector. To ensure that the flight time is proportional to the secondary ion mass, the primary ions need to have a very narrow distribution of kinetic energy. The kinetic energy  $E_{kin}$ , and thus the flight time  $t_F$  over a specified length  $L_a$  is given by [122]

$$E_{kin} = q \cdot U_e = \frac{m \cdot v^2}{2} \Rightarrow t_F = L_a \cdot \sqrt{\frac{m}{2 \cdot q \cdot U_A}} \quad (2.36)$$

## 2 Theoretical Aspects

with  $q$  being the charge of the ion,  $U_A$  the acceleration voltage,  $m$  the secondary ion mass and  $v$  the velocity. From eq. 2.36 it is clear that the mass signal from a doubly charged ion might interfere with the signal from a singly charged one of half its mass. However, for oxygen analysis in YSZ the sources for possible mass interferences, like  $^{32}\text{S}$  for  $^{16}\text{O}$ , are of negligible concentration.

The pulsed primary ion beam has a very low intensity and therefore a small sputtering effect. Hence, a secondary caesium gun of high intensity is also implemented, which is switched on after the complete region of interest has been scanned by the primary gun. Besides guaranteeing an effective material removal for depth profiling, some Cs ions are also neutralized and implemented in the investigated sample. The electropositive nature of the caesium atoms increases the secondary ion output for negatively charged ions like oxygen [123]. This setup is called dual-beam TOF-SIMS.

Finally, for charge compensation of the sample low energy electrons are constantly provided through a heated wire and an extraction voltage. This voltage is chosen to be small enough, usually about 20 V, to have negligible effect on secondary ion extraction and acceleration, which are in the kV range.

### 2.6.2 Evaluation of the $^{18}\text{O}$ concentration profiles

When the finite 90 ns pulse of the primary  $\text{Bi}^+$  ion beam hits the substrate, secondary ions are generated and separated by mass in the analyser of the SIMS machine. For low concentration atoms in the sample, like naturally abundant  $^{18}\text{O}$  (0.2% of the total oxygen content) in YSZ, the probability of being knocked out of the sample and becoming a secondary ion is equally distributed over the whole pulse length, resulting in a box shaped time resolved intensity spectrum, see Fig. 2.10(b). After detecting a secondary ion, the detector has a dead time of about 20 ns during which no further ion signals can be recorded. This limitation can be corrected up to a factor of 6 by a Poisson correction [122] included in the software. However, secondary ions from atoms present

## 2 Theoretical Aspects

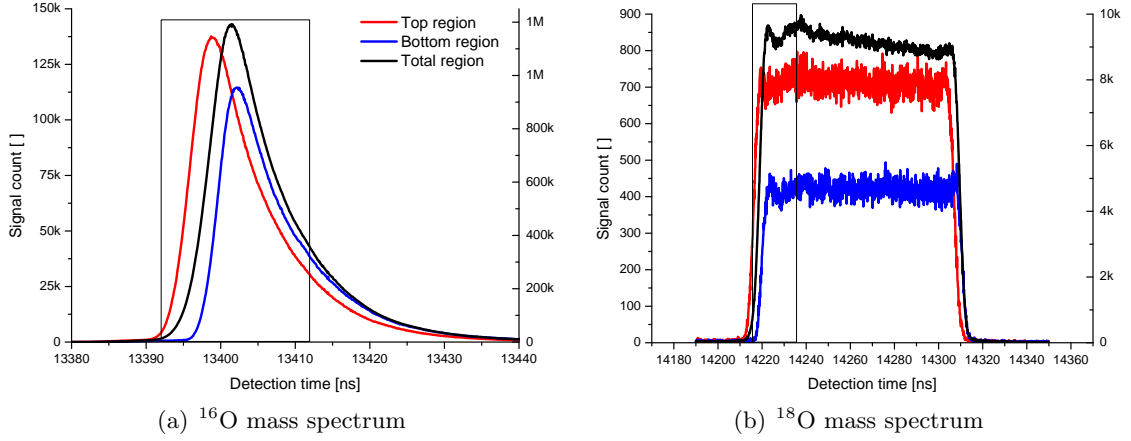


Figure 2.10: Mass spectra of the (a)  $^{16}\text{O}$  and (b)  $^{18}\text{O}$  signals recorded in a typical measurement (Sample Sap-PLD 2; lateral diffusion under the free YSZ Surface, see Table 7.2). The  $^{18}\text{O}$  signal in (b) is of ideal box-shape with a length equal to the primary ion pulse duration of 90 ns. The red and blue lines correspond to partial evaluations of the top or bottom regions in the lateral intensity images in Fig. 2.11, while the black line represents the total area. Due to the high signal count, the black lines scale with the right y-axis. The rectangular boxes highlight the integrated area of 20 ns used for calculating  $c_{^{18}\text{O}}$  with eq. 2.37. Note the different scaling of the x-axis.

in high concentrations like  $^{16}\text{O}$  are generated in large numbers during the whole pulse. Due to the dead time of the detector the ions generated in the first few nanoseconds are recorded preferentially and consequently clog up the detector for ions generated later in the pulse. This leads to asymmetric signals as shown in Fig. 2.10(a), which can not be reasonably Poisson corrected. Since evaluation of  $^{18}\text{O}$  concentrations ( $c_{^{18}\text{O}}$ ) relies on integrating the intensities ( $S_i$ ) of these time resolved oxygen signals according to

$$c_{^{18}\text{O}} = \frac{S_{^{18}\text{O}}}{S_{^{16}\text{O}} + S_{^{18}\text{O}}} \quad (2.37)$$

this is a major problem. In Ref. [124] an empirical method was proposed to overcome this issue, by integrating just the first 20 ns of each signal, see rectangular box in Fig. 2.10.

Another problem in evaluating the lateral profiles was charging of the sample surface during measurement, which lead to a change in intensity dependent on the analysed area,

## 2 Theoretical Aspects

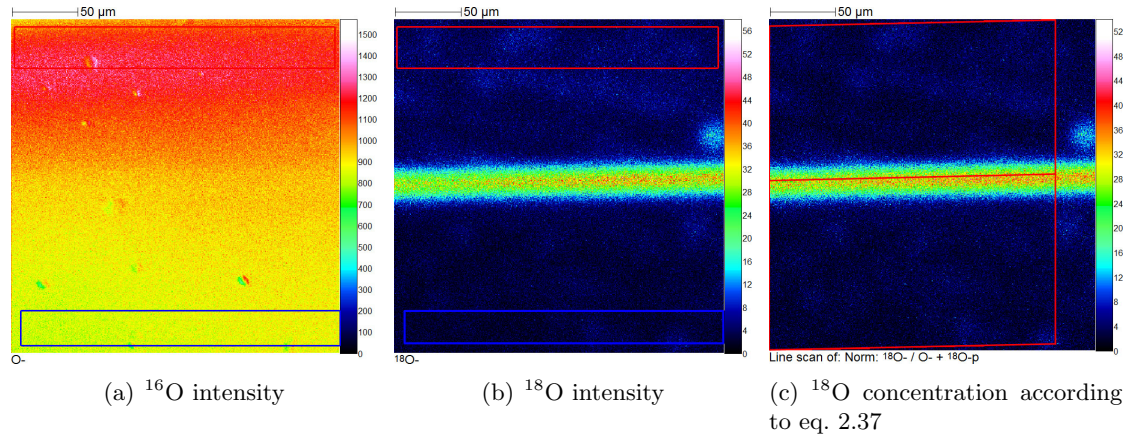


Figure 2.11: Lateral intensity distributions of the (a)  $^{16}\text{O}$ , (b)  $^{18}\text{O}$  signals and the (c) normalized concentration  $c_{^{18}\text{O}}$  according to eq. 2.37 (Sample Sap-PLD2; lateral diffusion under the free YSZ surface, see Table 7.2). The red and blue rectangles in (a) and (b) highlight the regions used to illustrate the signal shift between top and bottom region in Fig. 2.10. The two red boxes in (c) mark the integrated area for the lateral diffusion profiles in Fig. 2.12; the slightly distorted rectangular shape was necessary to exactly align with the  $c_{^{18}\text{O}}$  box profile, see also chapter 7.

most apparent in the  $^{16}\text{O}$  intensity distribution image in Fig. 2.37(a). The integrated area can only be set for a cumulative signal, but since the charged surface caused the  $^{16}\text{O}$  ions generated in the upper regions of the analysed area to arrive at a different time than the ones originating from the bottom regions, a different part of the signal is considered for integration, see red and blue data in Fig. 2.10. Due to the distinct asymmetric shape of the  $^{16}\text{O}$  signal this leads to different intensities. This drift is also present in the  $^{18}\text{O}$  signal, however, because of the symmetric box shape the intensity variation is not that pronounced. These effects could be minimized by randomly scanning the surface rather than in a sawtooth pattern and by increasing the pause time for charge compensation. However, the final lateral  $^{18}\text{O}$  concentration profiles still had a sloped baseline as shown in Fig. 2.12, which was subtracted before evaluation. It also proved favourable to subtract a baseline from the final profiles, as it simplified the fitting process by eliminating the need to include a parameter for the background concentration in eqs. 7.2 and 7.3.

## 2 Theoretical Aspects

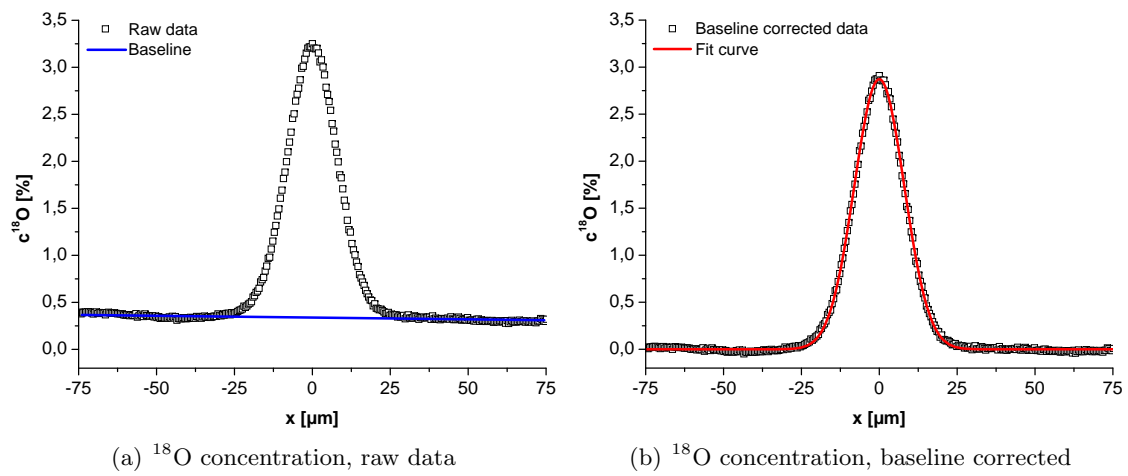


Figure 2.12: Lateral diffusion profiles of a typical sample (Layer Sap-PLD 2; lateral diffusion under the free YSZ surface, see Table 7.2) (a) without and (b) with baseline correction. The data was extracted from the highlighted area in Fig. 2.11(c). The blue line in (a) is the manually drawn baseline, which has been subtracted in (b). The fit curve in (b) was calculated by eq. 7.3.

# Experimental

## 3.1 Sample preparation

YSZ layers of different thicknesses were prepared by a sol-gel method and pulsed laser deposition (PLD) on MgO (100), SrTiO<sub>3</sub> (111) and sapphire Al<sub>2</sub>O<sub>3</sub> (0001) single crystalline 1 x 1 cm<sup>2</sup> substrates purchased from Crystec, Germany.

### 3.1.1 Sol-Gel process

The alkoxide route described in the following to prepare the YSZ sol was taken from Ref. [50]. Acetic acid (100% p.a.), Y(III) nitrate hexahydrate (99+%), 2-propanol (99,5+%) and HNO<sub>3</sub> conc. (65%, AnalPur) were purchased from Merck, Germany. Zr(IV) butoxide solution (80 wt. % in 1-butanol) was obtained from Aldrich, USA.

3.402 g of the zirconium complex in butanol was diluted with 6.39 g isopropanol to reduce viscosity and sensitivity to moisture. 0.85 g of acetic acid was added dropwise to the stirred solution and stirred for further 2 hours at room temperature to complete the reaction between the alkoxide and the acetic acid. The catalyst solution, consisting of 0.39 g isopropanol and 0.83 g nitric acid, was added afterwards and the solution was stirred for another 2 hours. Then the 0.477 g of the yttria salt was dissolved in 2.22 g

### 3 Experimental

of 2-propanol and added to the mixture, which was subsequently stirred for 12 hours overnight. The final solution was passed through a filter with 0.22  $\mu\text{m}$  pore diameter to remove any solid particles. The molar ratio of yttrium to zirconium in the solution is equivalent to a 7.8% yttria stabilized zirconia crystal.

An SCC-200 spin coater (KLM, Germany) was used for spin-coating the layers. 80  $\mu\text{l}$  of the YSZ sol were pipetted onto the spinning substrates and the rotation was maintained for further 30 seconds. Afterwards, the fresh layers were dried at room temperature, then at 100°C for 2 minutes each, and were finally calcined at 500°C for 10 minutes. Subsequent sintering lasted 12 hours at 1200°C with heating and cooling ramps of 10°C per minute.

#### 3.1.2 Pulsed laser deposition (PLD)

The targets for the laser ablation were prepared from 8%  $\text{Y}_2\text{O}_3$  doped  $\text{ZrO}_2$  (Tosoh, Japan) by cold isostatic pressing and subsequent sintering at 1550°C for 5 hours. The YSZ thin films were deposited on the single crystalline substrates at 0.04 mbar oxygen background pressure. The substrate temperature during deposition was between 500°C and 650°C, controlled by a pyrometer (Heitronics, Germany). A KrF excimer laser (Coherent Lambda Physics, Germany) with a pulse frequency of 5 Hz and a pulse length of 50 ns was used to ablate the YSZ target with an estimated fluence of about 1.5  $\text{J}/\text{cm}^2$  on the target. The distance between target and substrate was 6 cm. Different deposition times were employed to obtain various film thicknesses. In a few instances also a  $\text{La}_{0.6}\text{Sr}_{0.4}\text{CoO}_{3-x}$  (LSC) target, synthesized by a Pecchini method [66], was used to prepare mixed-conducting electrodes at 550°C in a background pressure of 0.4 mbar oxygen. All other parameters were the same as above. In Fig. 3.1 a sketch of the PLD setup is shown.

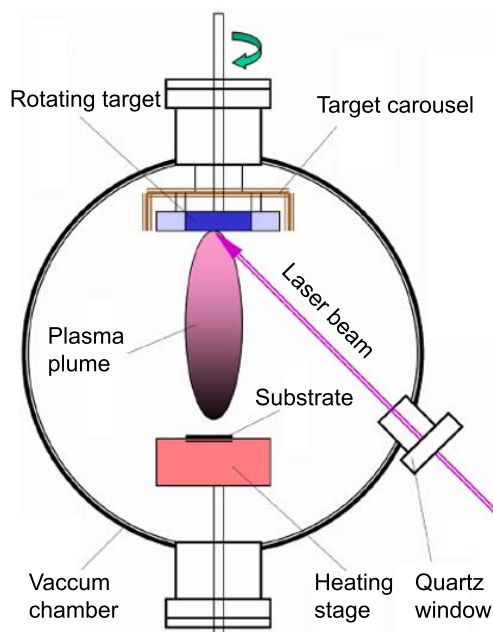


Figure 3.1: Sketch of the pulsed laser deposition (PLD) setup used. Image slightly modified from Ref. [125].

### 3.1.3 Photolithography and magnetron sputtering

Lift-off (negative) photolithography was employed to prepare defined electrodes for impedance spectroscopy studies and gas-tight barrier layers used in oxygen exchange experiments. For micro-patterning of LSC layers standard (positive) lithography was applied.

N-1430 photoresist was obtained from MicroResist Technology, Germany. 80  $\mu\text{l}$  of the photoresist was pipetted onto the spinning YSZ layer. Rotation speed was held constant for 30 s at 2700 rpm for lift-off and 3000 rpm for standard lithography using an SCC-200 spin coater (KLM, Germany). The resist was pre-baked at 100°C for 2 minutes to increase mechanical strength and exposed for 80 seconds to a USHIO 350DP Hg UV-lamp (Ushio, Japan). Photo masks were purchased from Rose, Germany. The unexposed photoresist was removed with a basic developing agent supplied by MicroResist Technology, Germany.

### 3 Experimental

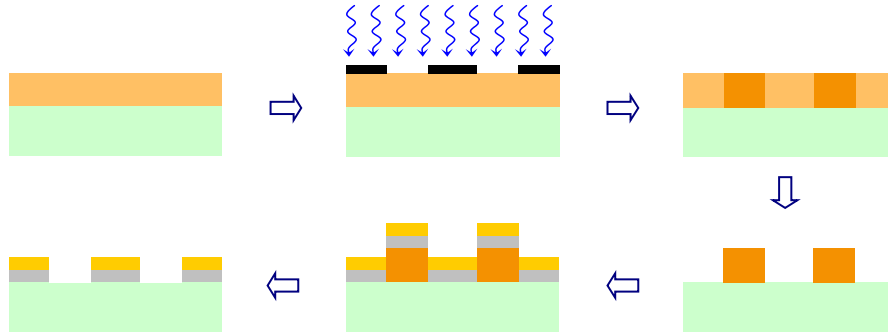


Figure 3.2: Spin coating of the substrate (green) and pre-baking of the photoresist (orange) → Exposure of the photoresist to UV light through a photomask → Parts of the resist have polymerized (toughened) → Removal of the unexposed photoresist with developing agent → Application of Cr/Au double layer → Removal of exposed resist with acetone

The samples meant for lift-off lithography were placed in a MED 020 magnetron sputtering machine (BalTec, Germany). For electrode preparation 400 nm gold was sputtered onto a 20 nm chromium adhesion layer, while the barrier layers were prepared by applying 100 nm Au on 80 nm Cr. The 200 nm thick platinum layers used in chapter 7 were not structured by photolithography since no sharp edges were required, but merely by covering parts of the surface with adhesive tape (Tixo, Austria) before sputtering.

In Fig. 3.2 the individual steps of the lift-off photolithography process are sketched, as this is the procedure predominantly used in this thesis.

## 3.2 Sample Characterisation

### 3.2.1 X-ray diffraction (XRD)

X-ray diffraction measurements were performed on a X'Pert PRO system (PANalytical, Germany), with primary and secondary Soller slits of 0.04 rad, a fixed divergence slit of 0.5°, a fixed antiscatter-slit of 1° and a 200 mm goniometer radius. Measuring time was 60 minutes between 5-135° in 2° intervals. A X'Celerator detector (PANalytical,

Germany) with a Ni K filter was used in Bragg-Brentano geometry with Cu K $_{\alpha}$  radiation. Final structural refinements were carried out with TOPAS 4.2 (Bruker, Germany).

#### 3.2.2 Evaluation of the film thicknesses

Film thicknesses were determined by sputtering a crater down to the YSZ/substrate interface, controlled by TOF-SIMS (TOF-SIMS V machine; IONTOF, Germany). The resulting sputter crater depth was measured by digital holographic microscopy (DHM, Lyncée tec, Switzerland).

#### 3.2.3 Atomic force microscopy (AFM)

Grain sizes of the thin films were determined by evaluating top-view images recorded by atomic force microscopy. Measurements were performed on a NanoScope V multimode AFM (Bruker AXS (formerly Veeco), USA) with a J-piezo scanner (maximum scan range: 120 x 120  $\mu\text{m}^2$ ) in tapping, constant amplitude mode using silicon cantilevers with integrated silicon tips (Arrow NC cantilevers, NanoWorld, Switzerland, spring constant 42 N/m, resonance frequency 285 kHz) under ambient conditions. The size of all images was 512 x 512 pixels and the images were recorded at a scanning rate of 2 Hz. Lateral grain sizes ( $d_G$ ) were calculated using the linear intercept method either manually or with aid of the EPQ program by IMTRONIC, Germany, see Fig. 3.3 and eq. 3.1.

$$d_G = \frac{\text{Total length of reference lines}}{\text{Total number of linear intercepts}} \quad (3.1)$$

#### 3.2.4 Electrical impedance spectroscopy

Impedance spectroscopy studies were carried out in ambient air by means of an Alpha-A high performance frequency analyzer (Novocontrol, Germany) in the frequency range of 1 MHz to 1 Hz with an effective amplitude of 1 V. Compared to studies on electrode reactions, where the amplitudes are about 10 mV, e.g. [116], this is a very large value.

### 3 Experimental

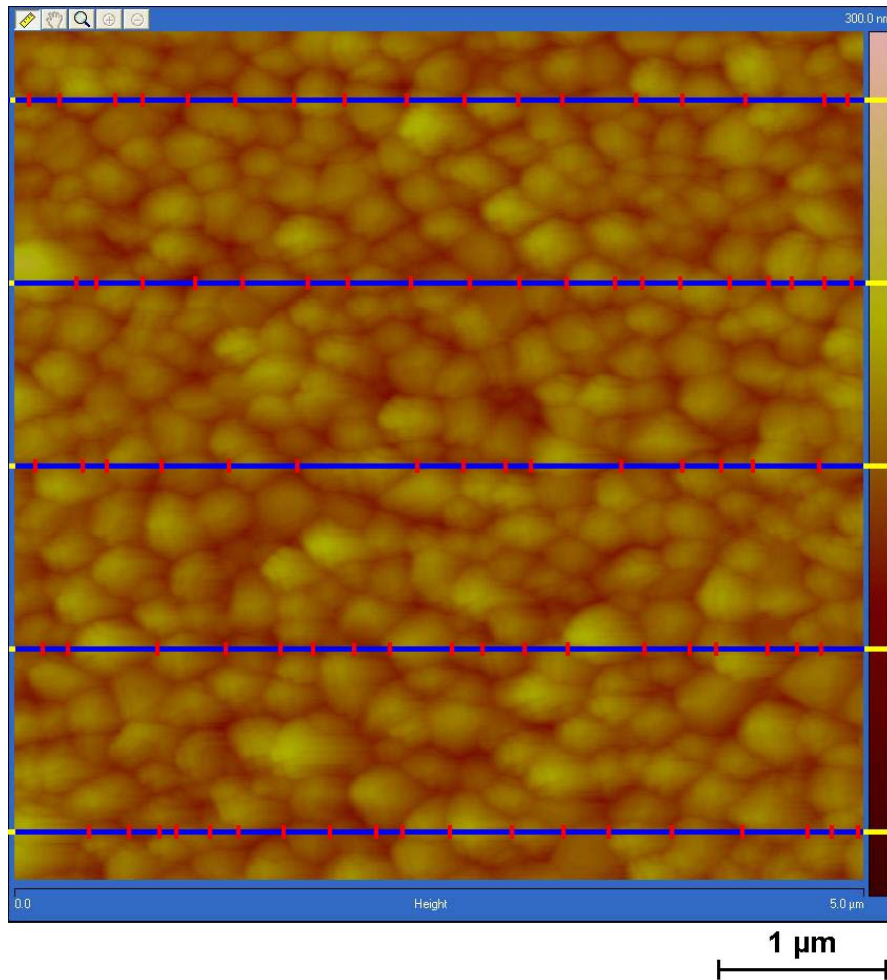


Figure 3.3: Example of a grain size evaluation using intercepts (red vertical lines) on reference lines (blue). The yellow areas of the reference lines outside the AFM image were not considered in the automated calculation. Example image taken from layer B, see Table 5.1

### 3 Experimental

However, in bulk YSZ this amplitude is evenly distributed over a lot of elementary reactions, i.e. oxygen ions hopping into neighbouring vacancies, while in electrodes a single charge transfer step is monitored. The far smaller number of grain boundaries might still cause a problem [119, 120], however even in the more coarse grained samples studied in this thesis, this voltage was still in the linear regime. In Fig. 3.4 two impedance spectra are shown, recorded with different amplitudes on the YSZ film, with the by far largest grain size of 440 nm investigated in this work (Sap-SG 1 in Table 7.1 or layer E in Table 5.1). Obviously the spectra overlap perfectly, but the increased amplitude allowed improved data quality.

The samples were placed on a heating stage and electric contact was provided by micro-manipulators (Suss Microtec, Germany) clamping gold coated steel tips (Pierenkemper, Germany). Spectra were usually recorded in 50°C intervals between 200°C and 500°C. Impedance data evaluation and simulation was done with ZView software (Scribner Associates Inc., USA).

#### 3.2.5 Tracer diffusion experiments

##### Temperature driven tracer implementation

97%  $^{18}\text{O}_2$  tracer gas was purchased from Campro scientific, Germany. Parts of the YSZ layers were covered with a Cr/Au barrier layer. The sample was equilibrated in air at 300°C in a quartz tube, then, after evacuation, the tube was filled with 250 mbar of the tracer gas and kept at 300°C for 30 minutes. Afterwards, the sample was quenched to room temperature. About half of the layer surface was covered with 200 nm Pt also using magnetron sputtering. Lateral  $^{18}\text{O}$  concentration profiles were measured before and after the diffusion using a TOF-SIMS V machine (IONTOF, Germany). The lateral diffusion was carried out on a heating stage in the vacuum chamber of the TOF-SIMS at 500°C for 30 to 90 minutes.

### 3 Experimental

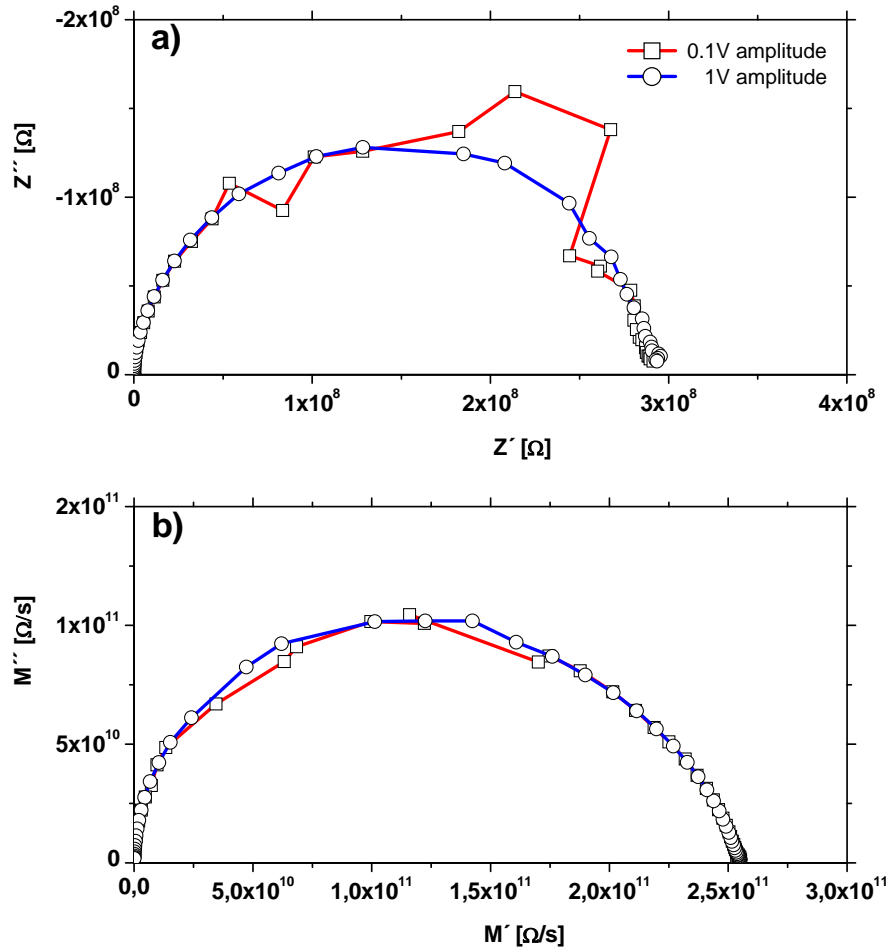


Figure 3.4: Impedance spectra in (a) NYQUIST and (b) modulus plots of a 28 nm YSZ thin film with 440 nm grain size (Sap-SG 1 in Table 7.1 or layer E in Table 5.1) at 300°C. The spectrum recorded with a 0.1 V amplitude (red line) shows significantly more data scattering than the spectrum recorded with a 1 V amplitude (blue line), but no systematic deviation is found. Both spectra were recorded on the same interdigital electrodes with a 25  $\mu\text{m}$  spacing, 10  $\mu\text{m}$  width and a total length of 9.0 cm. Data points at 50 and 100 Hz are removed as extreme outliers.

#### Current driven tracer implementation

For current-driven oxygen tracer incorporation into a YSZ film a mixed conducting  $\text{La}_{0.6}\text{Sr}_{0.4}\text{CoO}_{3-x}$  (LSC) layer of ca. 40 nm thickness was deposited on the YSZ film by PLD at a substrate temperature of 550°C. A 5 to 10  $\mu\text{m}$  broad gap was etched into the LSC layer using photolithography and hydrochloric acid thus yielding two electrodes for the electrical oxygen pumping experiments. LSC electrodes were chosen due to their low polarization resistance towards electrochemical oxygen exchange [66]. Electrical  $^{18}\text{O}$  incorporation into YSZ was performed at about 300°C in an atmosphere of ca. 200 mbar  $^{18}\text{O}_2$ . For the actual diffusion experiment a part of the YSZ film was covered by a 200 nm thick Pt film sputter-deposited after removal of the LSC electrodes. The lateral diffusion was carried out on a heating stage in the vacuum chamber of the TOF-SIMS at 500°C for 30 to 90 minutes. Tracer concentration analysis before and after diffusion was performed by TOF-SIMS.

#### 3.2.6 TOF-SIMS

$^{18}\text{O}$  concentration profiles were recorded with a TOF-SIMS V machine (IONTOF, Germany). A  $\text{Bi}^+$  primary ion beam with 90 ns pulse length (25 keV in burst alignment mode, 0.2 pA) and a  $\text{Cs}^+$  sputter beam (2 keV, 170 nA) were used to gain lateral concentration profiles with a maximum lateral resolution of about 200 nm. Only the first 20 ns of the  $^{16}\text{O}$  and  $^{18}\text{O}$  signal were integrated and used for evaluation, cf. chapter 2. Usually about 200 scans were accumulated for the final profiles with a minimum of 70 and a maximum of 570 scans.

### 3.3 Simulation

Finite elements calculations to simulate the substrate stray capacitances for the different electrode geometries in chapter 4, as well as the diffusion profiles in chapter 7, were done

### 3 Experimental

with COMSOL multiphysics 3.5 software (Comsol AB, Sweden). The standard linear solver UMFPACK was used with adaptive mesh refinement, until the final results did not significantly improve with each iteration.

Simulation of the electrode stray capacitances for the different electrode geometries was done in two dimensional mode, with a cross-sectional model normal to the electrode length  $L$  of one electrode finger, designations taken from Fig. 4.1(a). The extension in the x-direction was given by the area designated to the electrode width  $B$  plus half of the electrode spacing  $D$  on each side of it, thus giving a symmetrical model of width  $B + D$ . The individual values can be found in chapter 4. The y-extension was chosen to be the thickness of the alumina single crystals of  $500\ \mu\text{m}$ . The different elongations in x and y direction could be easily dealt with by the adaptive mesh refinement mode, by automatically generating an optimal mesh density. The electrode length normal to the simulated plane was set to 1 m, which was just an internal scaling factor for the final output and did not affect the finite element calculation directly. The anisotropic relative permittivity  $\varepsilon_r$  of the sapphire single crystal of 9.3 perpendicular and 11.5 parallel to the crystallographic c-axis [91, 126] was averaged to 10. The electrode area was forced to a constant voltage of 1 V, while the left and right boundary areas were set to 0 V, the remaining areas were set to zero flux. The final result was divided by two to give the capacitance between two neighbouring electrode fingers. The capacitive current through the surrounding air is not accounted for, and should amount to about 10% of the calculated values assuming  $\varepsilon_r = 1$ , which is discussed in chapter 4. In Fig. 3.5 an example of the resulting potential distribution of above calculations is shown.

The one dimensional simulation of the diffusion profiles is described in detail in chapter 7.

### 3 Experimental

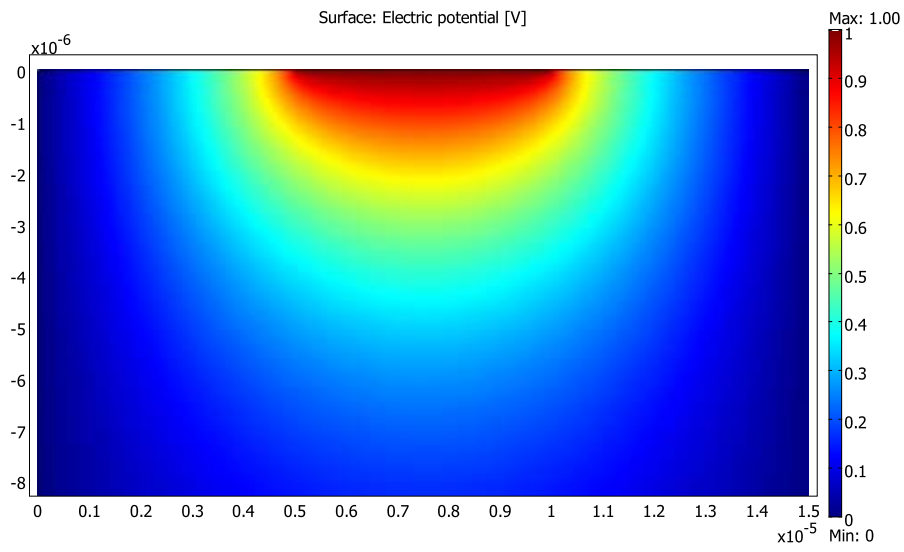


Figure 3.5: Cross section of a potential distribution of an electrode finger with 5  $\mu\text{m}$  width and 10  $\mu\text{m}$  spacing. The dimension of the x- and y-axis dimension is in meters, the colour code defines the potential in volts.

# The separation of grain and grain boundary impedance in thin YSZ layers

## 4.1 Introduction

In this chapter it is shown that optimizing the electrode geometry allows a separation of grain and grain boundary contributions even in very thin YSZ layers and for small grain sizes. A comparison with results obtained for conventional electrode geometries reveals a distinct improvement. The temperature dependent bulk and grain boundary conductivity of the thin films is determined and compared to that of macroscopic YSZ samples. This chapter has been published as a scientific paper in Ref. [18]

## 4.2 Theoretical Considerations

Electrical current flow in macroscopic polycrystalline bulk samples, i.e. charge transport through grain bulk and grain boundaries and partly also electrode reactions can be modelled with consecutive meshes of a resistor  $R$  parallel to a capacitor  $C$  for each process [127, 128]. If the characteristic, or peak frequencies  $\omega_{Peak} = \frac{1}{RC}$  of these  $RC$  elements are

#### 4 The separation of grain and grain boundary impedance in thin YSZ layers

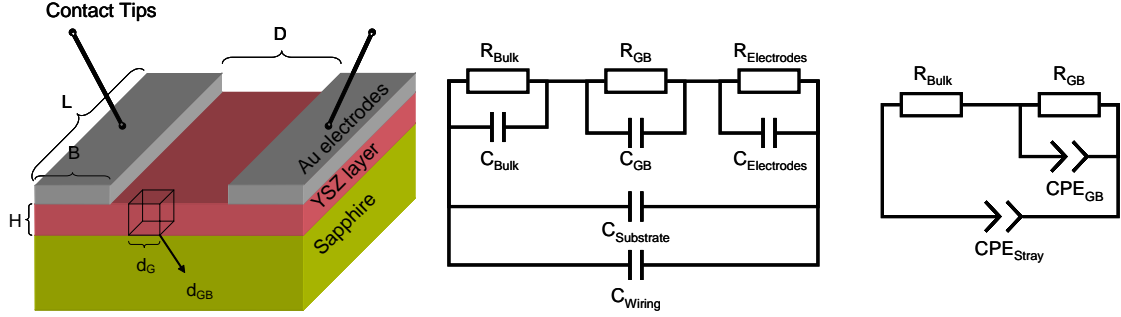


Figure 4.1: (a) Sketch of the measurement setup.  $L$  denotes the length of the electrodes,  $B$  their width, and  $D$  the distance between them. The thickness of the layer is referred to as  $H$ , the grain size is labelled  $d_G$ , and the electrical grain boundary thickness as  $d_{GB}$ . (b) Equivalent circuit representing a thin ion conducting layer on an insulating substrate. (c) Modified equivalent circuit used to fit all recorded impedance spectra in this study; capacitances are replaced by constant phase elements.

sufficiently different, each process can be well resolved in the total impedance spectrum. Impedance contributions of the set up (wires, etc.) are often of minor importance.

In the case of a thin film on an insulating substrate, however, one has also to consider the unavoidable substrate and setup impedance, mainly by adding parallel stray capacitances to the basic equivalent circuit. One stray capacitance ( $C_{Substrate}$ ) represents capacitive displacement current between the two electrodes through substrate (and also air). Another stray capacitor refers to the geometrical capacitance between the contacting wires, in the setup of Fig. 4.1(a) represented by contact tips ( $C_{Wiring}$ ). The total stray capacitance  $C_{Stray}$  is thus given by

$$C_{Stray} = C_{Substrate} + C_{Wiring} \quad (4.1)$$

These capacitances, if large enough, can make a separation of the above mentioned impedance contributions impossible. In Fig. 4.1(b) the resulting equivalent circuit for modelling lateral charge transport in an ion conducting thin film is plotted. It is obvious that in case of a large substrate capacitance compared to the bulk and grain boundary

#### 4 The separation of grain and grain boundary impedance in thin YSZ layers

capacitances ( $C_{Bulk}$  and  $C_{GB}$ ) only one effective RC element remains which includes both resistors and does not give any information on  $R_{Bulk}$  and  $R_{GB}$ .

In the following we discuss typical sizes of all capacitors and thus identify parameter regimes in which  $C_{GB}$  is at least of a similar size as  $C_{Stray}$ , and thus a separation of the bulk and grain boundary resistances ( $R_{Bulk}$  and  $R_{GB}$ ) becomes feasible. Using the symbols of geometrical parameters ( $L, H, D$ ) in Fig. 4.1(a) one can quantify the capacitance of the grain bulk by

$$C_{Bulk} = \varepsilon_{YSZ} \cdot \frac{L \cdot H}{D} \quad (4.2)$$

The symbol  $\varepsilon_{YSZ}$  denotes the bulk permittivity of YSZ. According to the brick layer model [128, 129] the capacitance of the grain boundaries is given by

$$C_{GB} = \varepsilon_{YSZ} \cdot \frac{L \cdot H}{d_{GB}} \cdot \frac{d_G}{D} \quad (4.3)$$

with  $d_G$  and  $d_{GB}$  denoting grain size and grain boundary thickness. It shall be noted that only the part of the layer between the electrodes is considered in eqs. 4.2 and 4.3, while additional lateral current beneath the electrodes is neglected. However penetration of the current beneath the electrodes is of minor importance for very thin layers ( $H \ll D$ ) considered in this contribution. An exact treatment of interdigital electrodes on electroceramic thin films can be found in Refs. [130] and [131]. The substrate stray capacitance is described by

$$C_{Bulk} = \varepsilon_{Substrate} \cdot \frac{L \cdot B}{D} \cdot f_{Geometry} \quad (4.4)$$

with  $\varepsilon_{Substrate}$  being the substrate permittivity which is assumed to be much larger than the vacuum value. The additional displacement current through air is thus neglected. Any effect of the YSZ film on  $C_{Substrate}$  is also neglected, as the film is thin compared

#### 4 The separation of grain and grain boundary impedance in thin YSZ layers

to the spacing between the electrodes. The geometry factor  $f_{Geometry}$  in eq. 4.4 only depends on the ratio of  $B/D$  and takes account of the in-plane arrangement of the electrodes.  $C_{Substrate}$  thus strongly depends on the ratio between width and distance of the electrodes.

The capacitance of the contact tips or wires is more difficult to estimate. However, it is clear that it depends on distance and size of the tips/wires and how they are positioned to each other, but it is not affected by the electrode geometry. The electrode capacitance on ion conductors ( $C_{Electrode}$ ), finally, can often be considered as a kind of double layer capacitance and is thus the largest in the system. It usually exceeds the others by several orders of magnitude and the frequency range in which it is relevant does not interfere with that of the other capacitances. For more information on the size of a typical electrode capacitance of Au on YSZ see for example Ref. [132].

It was already mentioned above that separability of bulk and grain boundary effects is expected to require a grain boundary capacitance with a size similar or larger than that of the stray capacitance. In order to achieve such situations the importance of the contact tips/wires can be minimized by using long electrodes, as  $C_{Wiring}$  is the only capacitance, which does not scale with the electrode length while  $C_{GB}$  linearly increases with  $L$ . For simultaneously maximizing the ratio

$$\frac{C_{GB}}{C_{Substrate}} = \frac{\varepsilon_{YSZ}}{\varepsilon_{Substrate}} \cdot \frac{H \cdot d_G}{B \cdot d_{GB}} \cdot f_{geometry} \quad f_{geometry} = f_{geometry} \left( \frac{B}{D} \right) \quad (4.5)$$

i.e. to reduce the importance of the substrate stray capacitance, the width of the electrodes  $B$  has to be reduced. In order to keep  $f_{geometry}$  constant and, moreover, from a practical point of view it is advisable to simultaneously reduce the distance between the electrodes, as this results in lower total resistances. All together, long and thin electrodes with a small distance should strongly help separating bulk and grain boundary impedance effects.

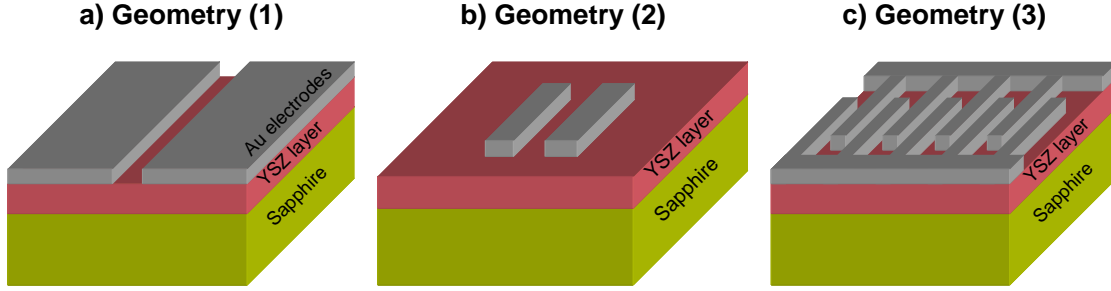


Figure 4.2: Schematic sketches of the different electrode geometries, images are not to scale. (a) Geometry (1) according to Ref. [31]: two large area electrodes that cover the whole sample surface ( $1 \times 1 \text{ cm}^2$ ), except a gap of 2 mm. A similar geometry is used in the present experimental work with a spacing of only  $500 \mu\text{m}$ . (b) Geometry (2) according to Ref. [16]: two wide electrodes (4 mm long,  $100 \mu\text{m}$  wide) with a spacing of  $68 \mu\text{m}$ . (c) Geometry (3) applied in the present experimental study: Narrow interdigital stripe electrodes connected to current collectors. Effective length of the individual finger is  $400 \mu\text{m}$ . Spacings are  $25 \mu\text{m}$  or  $10 \mu\text{m}$  and electrode width  $10 \mu\text{m}$  or  $5 \mu\text{m}$ . Usually several hundred fingers are connected in parallel leading to effective lengths of about 10 cm.

For more quantitative statements with estimates of the absolute values of the capacitances, a model YSZ layer ( $\varepsilon_{\text{YSZ}} = 27 \cdot \varepsilon_0$ ,  $\varepsilon_0$  is the vacuum permittivity) of 100 nm thickness with columnar grains of 20 nm diameter on a  $1 \times 1 \text{ cm}^2$  sapphire substrate ( $\varepsilon_{\text{Sapphire}} = 10 \cdot \varepsilon_0$ ) is considered. A width of the grain boundaries of 4 nm is used, as proposed in Ref. [133]. The specific grain boundary conductivity is assumed to be two orders of magnitude lower than the bulk conductivity in accordance with Ref. [16]. From the results in Ref. [132], the electrode double layer capacitance can be estimated to be  $\sim 1.6 \text{ Fm}^{-2}$  in case of 8 YSZ.

With these assumptions several electrode geometries were tested in terms of their ability to separate the different impedance contributions. The approach of pasting metal electrodes to the small faces of the sample [11–14, 43] will not be considered, as this leads to very pronounced stray capacitance effects. In Ref. [31] painted Ag-electrodes with a spacing of 2 mm were used and we consider such a geometry assuming that the entire

#### 4 The separation of grain and grain boundary impedance in thin YSZ layers

Table 4.1: Calculated capacitances for a 100 nm thick YSZ layer with a grain size of 20 nm and an electrical grain boundary width of 4 nm on a 0.5 mm thick sapphire single crystal. The capacitances are normalized to the electrode length.

Electrode geometry	$C_{Bulk}$ [pF/m]	$C_{GB}$ [pF/m]	$C_{Substrate}$ [pF/m]	$\frac{C_{GB}}{C_{Substrate}}$	$C_{Electrode}$ [μF/m]
(1) large area	0.012	0.060	17.4	0.003	6400
(2) wide stripes	0.352	1.76	74.9	0.023	160
(3) narrow stripes /interdigital	2.39	12.0	69.0	0.174	8.00

remaining surface is covered with silver as in Fig. 4.2(a): Geometry (1), large area). The electrodes used in Ref. [16] were stripes of 100 μm x 4 mm with a spacing of 68 μm and such a situation is represented by Geometry (2), in Fig. 4.2(c) (wide stripes). These two typical geometries are compared to one of the electrode designs used in this paper, namely 5 μm broad electrodes with a spacing of 10 μm; Several hundred 400 μm long parallel stripes are connected to an interdigital electrode with a total electrode length of more than 10 cm, cf. Fig. 4.2(c): Geometry (3), narrow stripes/interdigital).

In Table 4.1 the calculated capacitances are listed for all electrode configurations. Values are normalized to the electrode length. The geometric factor  $f_{geometry}$  needed in eq. 4.4 was numerically evaluated using finite element calculations.  $C_{Wiring}$  was assumed to be negligible. In Ref. [16] the substrate stray capacitance of geometry (2) was measured to be 80 pF/m, which is in good agreement with the calculated value in Table 4.1. The results in Table 4.1 clearly show that by using an optimized geometry the ratio of grain boundary to substrate stray capacitance can be significantly improved, and thus a separation of both effects becomes feasible even for very thin films and small grains. The electrode capacitance is at least five orders of magnitude larger than any other contributing capacitance, making it easily distinguishable. Fig. 4.3 displays the corresponding calculated impedance spectra. For better comparability the resistances of bulk and grain boundaries are set to the same values for all cases. The Nyquist plot in Fig. 4.3(a) does not show any clear difference between the spectra. The vertical response

4 The separation of grain and grain boundary impedance in thin YSZ layers

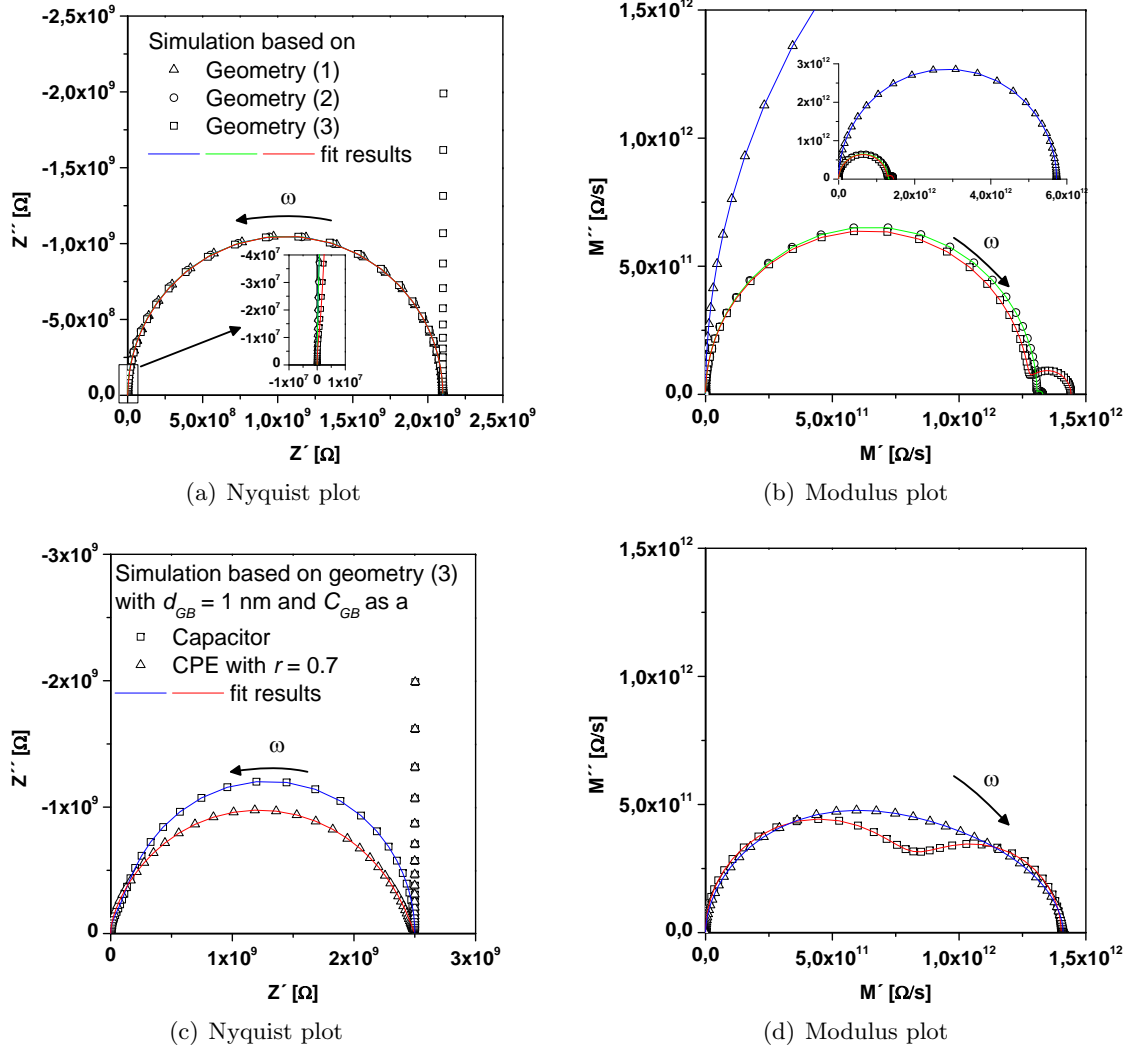


Figure 4.3: Simulated impedance spectra using the equivalent circuit in Fig. 4.1(b) in the frequency range from 1 MHz to 0.001 Hz with 10 points per decade for a 1 cm long electrode. The capacitances used in (a), (b) (c), and (d) are listed in Table 4.1. The bulk and grain boundary resistances for (a) and (b) were set to  $R_{Bulk} = 0.1 \text{ G}\Omega$  and  $R_{GB} = 2 \text{ G}\Omega$  and to  $R_{Bulk} = 0.5 \text{ G}\Omega$  and  $R_{GB} = 2 \text{ G}\Omega$  for (c) and (d). In (a) and (c) the Nyquist plots are shown. In (b) and (d) the complex modulus plots are depicted, the inset in (b) has another scaling to show all spectra in one graph. The red, blue, and green lines are fits to the equivalent circuit in Fig. 4.1(c).

#### 4 The separation of grain and grain boundary impedance in thin YSZ layers

at low frequencies is due to the large electrode capacitance and the semicircle diameter reflects the sum of the grain boundary ( $R_{GB} = 2 \text{ G}\Omega$ ) and bulk resistance ( $R_{Bulk} = 0.1 \text{ G}\Omega$ ). Also in the high frequency range almost no deviation from a semicircle can be seen, cf. inset in Fig. 4.3(a). Separation of grain and grain boundary effects seems to be impossible for all three geometries.

However, when looking at the complex modulus plot in Fig. 4.3(b) the effect of the different electrode geometries becomes obvious. While the grain boundary and bulk capacitances for geometry (1) are completely masked by the large stray capacitance, a very small additional semicircle can already be seen in the high frequency range for a setup with geometry (2). The most pronounced separation, however, is achieved with geometry (3). The high frequency arc in this modulus plot is mainly caused by the grain boundary capacitance. However, owing to the parallel connection of  $C_{GB}$  and  $C_{Stray}$ , the corresponding diameter is not given by  $(C_{GB})^{-1}$ . Obviously, even for a total grain boundary capacitance being a factor of 6 smaller than the substrate capacitance a very clear separation of bulk and grain boundaries becomes visible in the modulus plot, though not in the impedance (Nyquist) plot. Unfortunately, in real experiments the situation is less straightforward. First, the capacitive impedances hardly behave like ideal capacitors and for a better description, constant phase elements have to be used instead. Moreover, according to our experience keeping  $C_{Bulk}$  or the corresponding constant phase element in the equivalent circuit does not lead to any meaningful fitting values and unrealistic exponents  $r$  of the constant phase element  $CPE$  with impedance  $Z_{CPE} = Q^{-1}(i\omega)^{-r}$  of 0.1-0.5 are often found for our measurements. Accordingly  $C_{Bulk}$  (or  $CPE_{Bulk}$ ) is often simply used by the fit algorithm to optimize other parts of the spectrum. This was caused by the extremely low bulk capacitance compared to any  $C_{Stray}$  measured or considered in this study. Hence, a modified circuit with constant phase elements for grain boundaries and stray effects but without  $C_{Bulk}$ , see Fig. 4.1(c), is employed to fit measured as well as simulated spectra (see Fig. 4.3). Since electrode

#### 4 The separation of grain and grain boundary impedance in thin YSZ layers

contributions to the impedance spectra ( $C_{Electrode}$  and  $R_{Electrode}$ ) are well separated and not in the focus of our interest, the modified equivalent circuit does also not account for them. According to eq. 4.1  $C_{Wiring}$  and  $C_{Substrate}$  can be represented by one stray capacitance  $C_{Stray}$  or a corresponding constant phase element.

The effect of all these modifications will be demonstrated by using the reduced circuit in Fig. 4.1(c) to fit the data simulated with the circuit in Fig. 4.1(b). For the optimized electrode geometry (3) suggested here the deviation of fit results from the set values of the grain boundary capacitance is 13 % while 5 % result for the stray capacitance, which is acceptable. The grain boundary resistance is 4.3 % lower than the set value, which consequently causes the bulk resistance to be 43 % higher while the total resistance is fitted correctly. This is a considerable deviation and indicates that we are at the limit of a reasonable separation of bulk and grain boundary contributions by using the equivalent circuit in Fig. 4.1(c). On the other hand the results of the present study suggest an electric grain boundary width of only about 1 nm, causing the grain boundary capacitance to be almost equal to the stray capacitance for geometry (3). In such a case the separation of the arcs in the modulus plots is even better. Moreover, this leads to much lower relative errors, with the largest deviation of roughly 10 % for the bulk resistance.

In Fig. 4.3(c) and Fig. 4.3(d) further calculated spectra assuming equal grain boundary and stray capacitances are shown as Nyquist and modulus plots. Absolute capacitance values are listed in Table 4.1; grain and grain boundary resistances are 0.5 and 2 G $\Omega$  respectively. In these diagrams also the strong effect of the non-ideality of the grain boundary capacitance is illustrated. When using ideal capacitances the two arcs are very well separated in the modulus plot and even a slight shoulder can be seen in the Nyquist plot at high frequencies. When replacing the grain boundary capacitance in the circuit of Fig. 4.1(b) by a constant phase element and setting  $r$  to 0.7 the shape of the spectrum changes to a single depressed semicircle in the Nyquist plot and to much less

separated arcs in the modulus plot. However, the quality of the fit is not affected by this change and still grain and grain boundary contributions can be separated. These and many other simulations showed that for grain boundary capacitances being similar or higher than the stray capacitance, a separation of bulk and grain boundary becomes indeed possible and grain boundary contributions are easily visible in the modulus plot even for non-ideal grain boundary capacitances (i.e. constant phase elements). This will be exemplified in the following experimental study.

## 4.3 Experimental Results and Discussion

### 4.3.1 Microstructure of the YSZ thin films

Three YSZ layers were investigated and are denoted in the following as layer A, B, and C. The layer thicknesses determined by DHM were  $105 \pm 1$  nm for layer A,  $18 \pm 3$  nm for layer B, and  $32 \pm 1$  nm for layer C. The corresponding XRD patterns are shown in Fig. 4.4(a), (b) and (c). All layers are oriented in the (1 1 1) direction of the cubic fluorite structure. However, the signal intensity is much higher in case of the 105 nm thick layer A, cf. Fig. 4.4(a), which indicates a high crystallinity of this film. In Fig. 4.4(b) and (c) the patterns of the as-prepared samples are compared to those measured after annealing at 1000°C for 5 hours. The reduction of the half-width of the peaks is attributed to crystal growth during the heat treatment. Structure refinement suggests an increase of the crystallite size from 15 nm to 21 nm for layer B and from 22 nm to 43 nm for layer C. The crystallite size for layer A determined by structural refinement before any annealing was 72 nm. It is important to note that these crystallite sizes do not correspond to the grain sizes used in the discussion of the electrical properties. Due to the high texture of the layers and the use of the BRAGG-BRENTANO geometry, only statements can be made about the (1 1 1)-direction. YSZ layers prepared by PLD are expected to have columnar structure (see Ref. [23]), hence the crystallite sizes determined by XRD give an

#### 4 The separation of grain and grain boundary impedance in thin YSZ layers

information about the height of these columns, but not on their diameter. The increasing crystallite size (column height) fits well to the increasing film thickness of layers B, C, and A. The deviation of these crystallite sizes from the exact layer thicknesses determined by DHM may be related to strain present in the thin layers. However, these strain effects are not easily evaluated, due to the few peaks present in the XRD patterns. A slight shift to higher diffraction angles is observed in the patterns of the annealed samples, which indicates a decrease of the lattice parameter of the cubic YSZ. In layer B the parameter changes from 0.517 nm to 0.512 nm and in layer C from 0.516 nm to 0.512 nm. In layer A the lattice parameter is 0.515 nm. All these values are close to the lattice parameter of macroscopic polycrystalline 8 YSZ of 0.514 nm (see Ref. [106, 134]).

In order to probe the diameter of the PLD grown YSZ columns of the layers, AFM images were recorded. Fig. 4.5 shows the surface morphology of sample A. The very narrow size distribution of distinct grains allows an easy determination of the mean grain column diameter ( $19 \pm 3$  nm). AFM measurements on the very thin layers B and C revealed a trend towards smaller grain sizes, however, determination of quantitative values for the grain column diameters was not possible owing to the broad size distribution and partly insufficient contrast.

### 4.3.2 Electrical Measurements

#### Effect of electrode geometries

Interdigital electrodes were prepared with a broad current collector at both sides as sketched in Fig. 4.2(c) and shown in an image of the prepared electrodes in Fig. 4.6(c). Despite their large area the current collectors exhibit only a very small contribution to the overall substrate capacitance ( $< 5\%$ ). The effective length of the individual fingers was nominally 400  $\mu\text{m}$  and they ended at a distance of 50  $\mu\text{m}$  from the opposite current collector. Several different electrode configurations were deposited on layer A with 25  $\mu\text{m}$  or 10  $\mu\text{m}$  spacings ( $D$ ) between the electrodes and a stripe width ( $B$ ) of 10  $\mu\text{m}$  or 5  $\mu\text{m}$ .

#### 4 The separation of grain and grain boundary impedance in thin YSZ layers

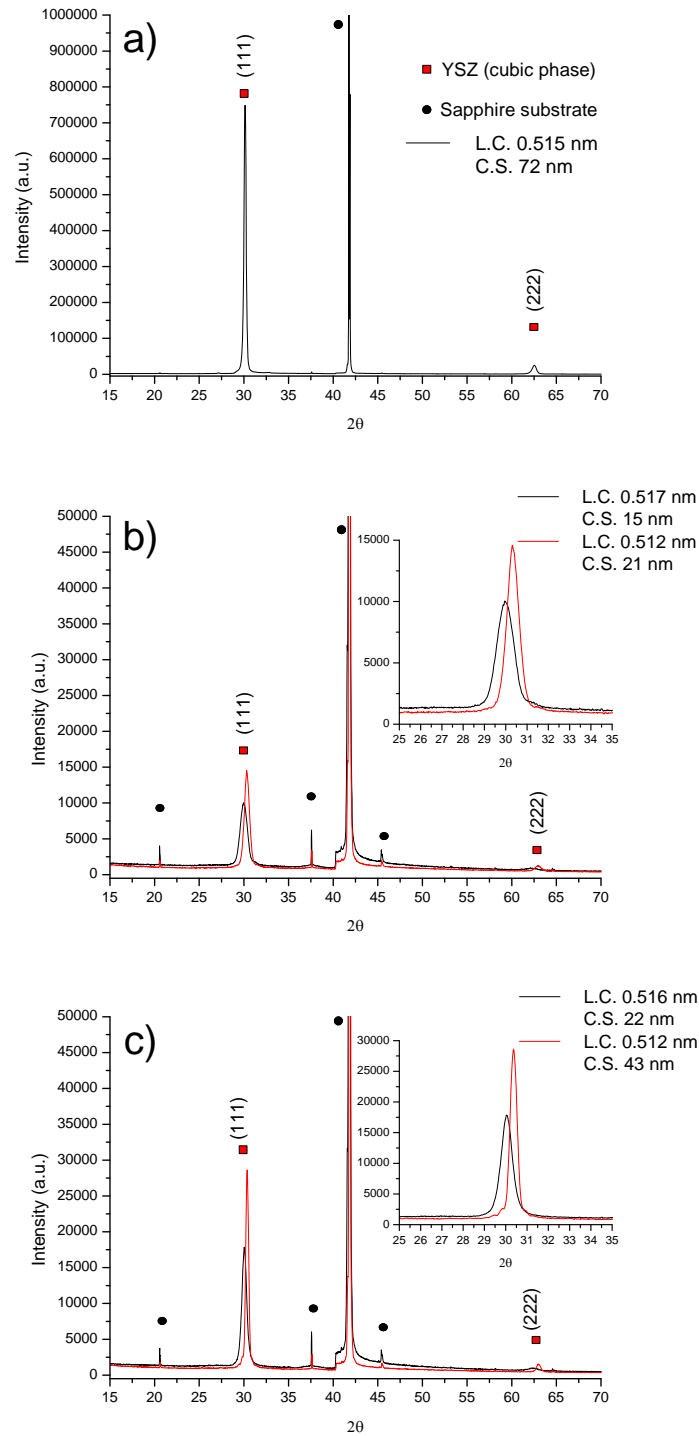


Figure 4.4: XRD patterns of as prepared (a) Layer A (105 nm thin), (b) Layer B (18 nm) and (c) Layer C (32 nm). In the legend L.C. means the lattice constant of the cubic YSZ layer and C.S. the crystallite size in the (111) direction. In (b) and (c) the red line corresponds to a measurement after annealing at 1000 °C for 5 h. The inlay in (b) and (c) shows a magnification of the (111) reflex.

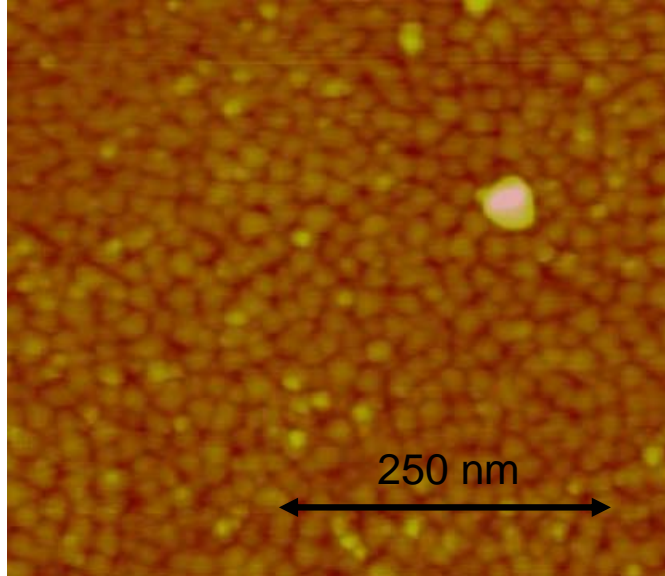


Figure 4.5: AFM image of the surface of layer A.

The effective length ( $L$ ) of the electrodes was calculated by multiplying the number of intact fingers with the length of an individual finger. For comparison also electrodes according to geometry (1) in Fig. 4.2(a) were deposited on the sample. These were intentionally poorly designed with a spacing of  $500\ \mu\text{m}$  and a total length of about 8 mm. The electrode width was approximately 5 mm, which is half the sample width.

Fig. 4.7 compares impedance data obtained for this geometry with those measured on electrodes designed according to geometry (3). The latter interdigital geometry was optimized as far as possible in terms of the stray capacitance and had a finger distance of  $10\ \mu\text{m}$ , an effective length of 14.40 cm, and an electrode width of  $5\ \mu\text{m}$ . The different shapes of the spectra clearly illustrate the effect of the reduced importance of the stray capacitance for electrodes manufactured according to geometry (3). The spectrum measured on the poorly designed electrode can be fitted to a simple  $R - CPE$  equivalent circuit, thus not allowing any separation of grain and grain boundary contributions. In case of the optimized electrode only the circuit in Fig. 4.1(c) leads to an acceptable fit result. A single  $R - CPE$  element severely fails in fitting the experimental data

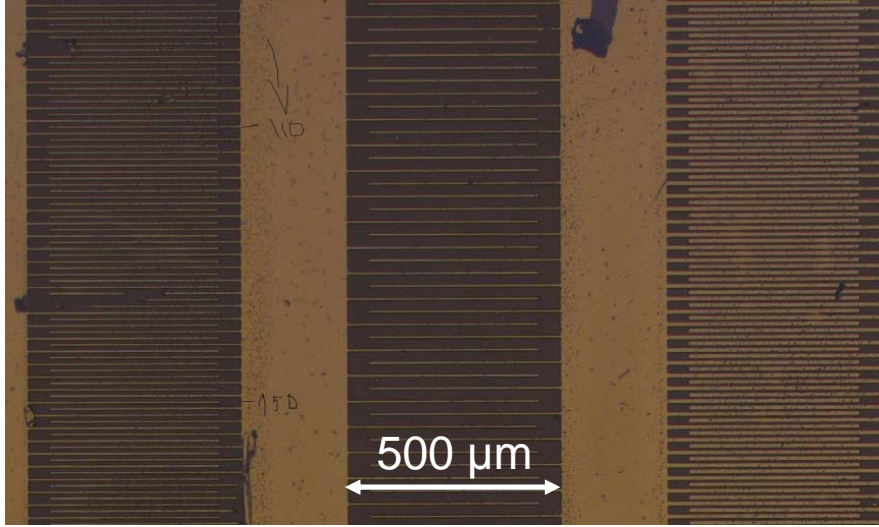


Figure 4.6: Several interdigit electrode geometries on layer A. The broad perpendicular stripes are the current collectors.

which is particularly visible in the modulus plot. Even when the geometry was less optimized (10  $\mu\text{m}$  broad, 25  $\mu\text{m}$  spaced electrodes), two contributions could be observed in the modulus plot and fitted to the circuit in Fig. 4.1(c).

Strongly overlapping rather than well separated arcs, cf. Fig. 4.3(d), can be attributed to the constant phase elements with exponents being smaller than 1. The values determined from the measurements usually varied between  $r = 0.7$  and 0.8 for the grain boundary capacitance, while for the substrate stray capacitance  $n$  was very close to 1. To calculate capacitances from the constant phase element of the grain boundaries

$$C_{GB} = (R_{GB}^{1-r} Q_{GB})^{\frac{1}{r}} \quad (4.6)$$

was used (see Ref. [135]). These observations already indicate a successful separation of grain and grain boundary effects. However, for further verification several different interdigital electrode geometries were investigated on layer A (105 nm thick). The results of the measured capacitances and the numerically calculated substrate capaci-

4 The separation of grain and grain boundary impedance in thin YSZ layers

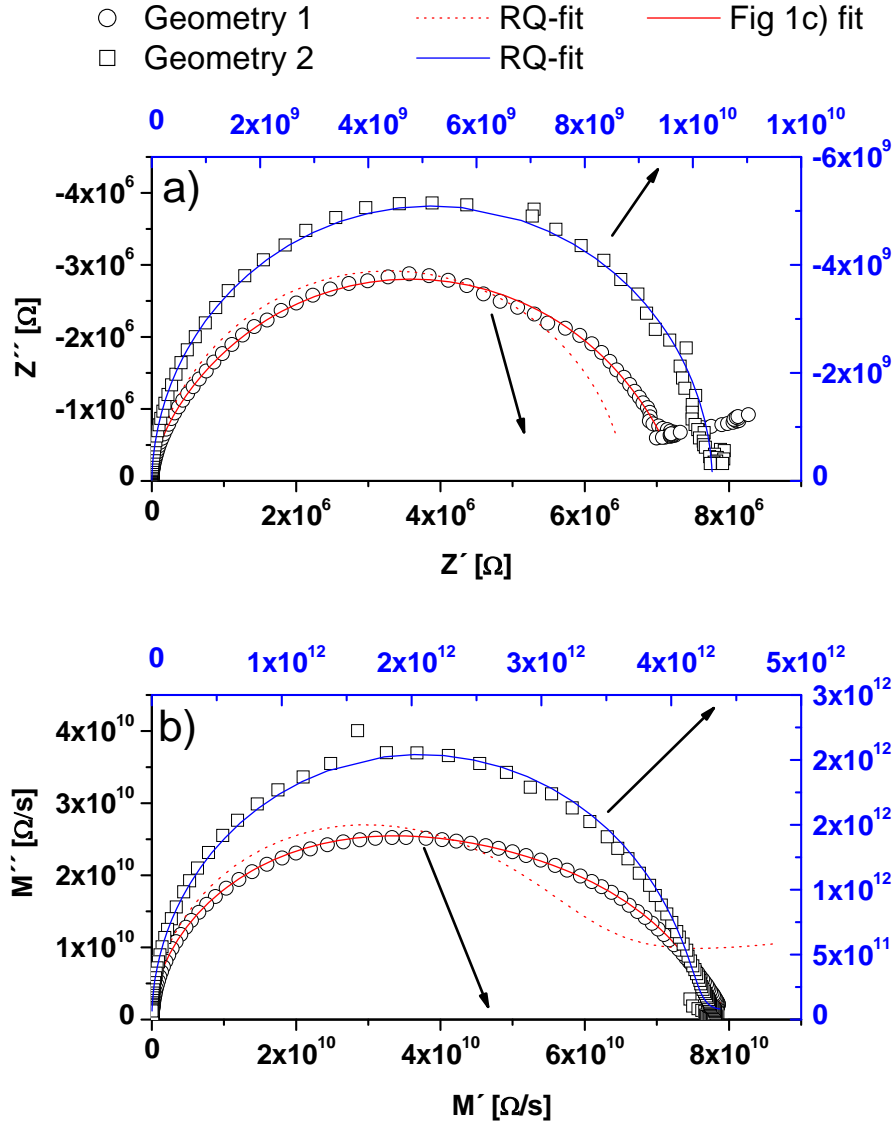


Figure 4.7: Impedance spectra measured on layer A (105 nm thin) with two different electrode geometries at 300°C. Frequency range was 1 MHz to 1 Hz with 10 points per decade. Diagram (a) is a Nyquist-plot, (b) is a modulus-plot of the data. Geometry (3) is an interdigital electrode, see Fig. 4.2(c), with 5  $\mu\text{m}$  broad fingers having a distance of 10  $\mu\text{m}$ , the effective electrode length was measured to be 14.40 cm. Geometry (1) consists of approximately 5 mm broad, 500  $\mu\text{m}$  spaced stripes of 8 mm length as in Fig. 4.2(a). For easier comparison of the different shapes of the spectra different scales are used for geometry (3) (black) and geometry (1) (blue). The red lines are fitting results for geometry (3) with an  $R - CPE$  equivalent circuit (dotted line) and the circuit in Fig. 4.1(c) (solid line). The solid blue line is a fit to data from geometry (1) with a single  $R - CPE$  equivalent circuit ( $r \approx 1$ ). The arrows indicate the appropriate axis scales.

#### 4 The separation of grain and grain boundary impedance in thin YSZ layers

tances are summarized in Table 4.2. For comparison, macroscopic measurements on a YSZ polycrystal and a YSZ single crystal are also included. The resulting conductivities are plotted in an ARRHENIUS diagram in Fig. 8. The appropriateness of the resulting geometry dependence of the fit elements will be discussed in the following.

Calculated and measured values for the stray capacitances are in acceptable agreement for all the geometries and follow the predicted trend, even though the simulated values are somewhat lower than the measured ones. This might be explained by two factors: Firstly, the calculated values are based on a two dimensional simulation, which neglects additional capacitive contributions of the interdigital design, for example caused by the current collectors. Secondly, the capacitive contribution of the surrounding air was not included in the simulation either. A combination of these effects can explain an underestimation of about 15 %, which is close to the measured deviation. Hence, we conclude that the simulation is very useful in predicting electrode configurations for which a separation becomes feasible and that the fit parameter  $C_{Stray}$  is indeed the stray capacitance.

According to eq. 4.3 the grain boundary capacitance should only depend on the spacing of the electrodes, when being normalized to the electrode length. When comparing the grain boundary capacitances in Table 4.2, the averaged measured ratio for 25  $\mu\text{m}$  and 10  $\mu\text{m}$  spaced electrodes is about 2. This shows the predicted trend of the electrode distance even though the value of 2.5 expected from eq. 4.3 is not exactly met. Partly this might be due to the simplified electrode geometry used in the modelling and eq. 4.3 (e.g. neglecting displacement current beneath the electrodes, see Refs. [130, 131]). Also neglecting  $C_{Bulk}$  in the equivalent circuit (see above) may play a role. The capacitance of the contacting needles and the setup ( $C_{Wiring}$ ) was measured to be 25 fF, which is at least two orders of magnitude smaller than the grain boundary capacitance; it should thus be of no importance in our case.

The grain boundary thickness was calculated from the measured values of  $C_{GB}$  in

Table 4.2: Capacitance values are averaged over the temperature range from 200°C to 400°C, resistance values obtained at 300°C and activation energies, all determined on layer A (105 nm thick) for different electrode geometries. For comparison, calculated substrate capacitances and activation energies of poly- and single crystalline YSZ are shown. Capacitances and resistances are normalized to the electrode length. Measured stray capacitances are averaged over values of  $Q$  with  $r > 0.98$  for the constant phase element in Fig. 4.1(c).

Electrode Geometry		$C_{GB}$	$C_{Stray}$	$C_{Substrate}$	$R_{Bulk}$	$R_{GB}$	$E_a$	$E_a$	
Distance	Width	Length		calculated	at 300°C	at 300°C	Bulk	GB	
[ $\mu\text{m}$ ]	[ $\mu\text{m}$ ]	[cm]	[pF/m]	[pF/m]	[M $\Omega\text{cm}$ ]	[M $\Omega\text{cm}$ ]	[eV]	[eV]	
10	5	14.40	$91 \pm 6$	$85 \pm 7$	$69$	$34.0 \pm 0.8$	$85 \pm 1$	0.99	1.10
10	10	12.76	$80 \pm 10$	$94 \pm 9$	$88$	$42.5 \pm 0.8$	$103 \pm 1$	0.98	1.14
25	5	10.08	$39 \pm 5$	$69 \pm 6$	$51$	$75 \pm 2$	$190 \pm 2$	0.95	1.17
25	10	9.2	$45 \pm 6$	$89 \pm 5$	$64$	$52 \pm 2$	$164 \pm 3$	0.97	1.14
500	5000	0.8	-	$33 \pm 4$	$47$	-	-	1.12	-
YSZ polycrystal			-	-	-	-	-	1.05	1.17
YSZ singlecrystal			-	-	-	-	-	1.11	-

#### 4 The separation of grain and grain boundary impedance in thin YSZ layers

Table 4.2 with eq. 4.3 and an averaged value of  $d_{GB} = 1.0$  nm results for the grain size  $d_G = 19$  nm. This value for the grain boundary thickness is in the range of the structural width of the interface and significantly smaller than values obtained on macroscopic samples and also on thicker layers: In Ref. [16]  $d_{GB} = 5.4$  nm for  $d_G \geq 232$  nm is reported. For polycrystalline samples the values are in the same range ( $d_{GB} = 5$  nm independent of  $d_G$  [73];  $d_{GB} = 5.4$  nm for  $d_G > 350$  nm [72]). Using the nano grain composite model  $d_{GB} = 4.2$  nm for  $d_G = 26$  nm is reported in Ref. [133]. However, in all these cases the grains are of more or less “isotropic” shape and randomly oriented, while in the present case highly textured columnar grains in PLD layers are studied. While inaccuracies in the measurements and the simplified model used for fitting the impedance data might contribute to the small value calculated in the present study, we would also not exclude that a grain boundary width of about 1 nm is indeed a true property of the layer. However, more experimental data is needed to confirm or reject this hypothesis.

The measured (fitted) grain and grain boundary resistances at 300°C as well as the corresponding activation energies are given in Table 4.2. Grain boundary and bulk resistances at the same temperatures and corrected to the electrode length are indeed almost indirectly proportional to the electrode distance. A resistance increase by a factor of approximately 1.9 for the grain boundaries and of 1.7 for the bulk is found. Deviations from the value of 2.5 (ratio of the electrode distance) might originate from slight temperature variations of a few degrees on the sample surface; also in this case the simplified model neglecting  $C_{Bulk}$  may have an effect, as well as the idealized treatment of the interdigital electrodes [130, 131].

The activation energy for ion conduction in the grain bulk of our film (ca. 0.98 eV) is in good agreement with the value of our macroscopic polycrystalline material of 1.05 eV

#### 4 The separation of grain and grain boundary impedance in thin YSZ layers

or 1.08 eV as given in Ref. [16]. The absolute value of the bulk conductivity, calculated from  $R_{Bulk}$  and the geometrical parameters  $H, D, L$  according to

$$\sigma_{Bulk} = \frac{1}{R_{Bulk}} \cdot \frac{D}{L \cdot H} \quad (4.7)$$

correlates quite well with macroscopic values of poly or single crystalline samples, see Fig. 4.8. This means that the lower overall conductivity of our YSZ films (indicated in Fig. 4.8 by the effective conductivities of geometry (2) with  $D = 500 \mu\text{m}$  and  $B = 5000 \mu\text{m}$ ) is indeed only due to blocking grain boundaries. Bulk properties are hardly changed even in a film of 100 nm thickness and a grain size of approximately 20 nm. The deviations obtained at higher temperatures are explained by the fact that the high relaxation frequencies of the bulk make the fit data less accurate.

Transport through the grain boundaries with an activation energy of 1.14 eV is in accordance with that of the macroscopic reference of 1.17 eV and the value in Ref. [16] of about 1.15 eV. The associated conductivity (Fig. 4.8) was calculated according to

$$\sigma_{GB} = \frac{1}{R_{GB}} \cdot \frac{D}{L \cdot H} \cdot \frac{d_{GB}}{d_G} \quad (4.8)$$

with  $d_G = 19 \text{ nm}$  and  $d_{GB} = 1.0 \text{ nm}$ . As in eqs. 4.3, (3) and (7) this relation neglects current beneath the electrodes but proves to be a good approximation for all films considered here ( $H \ll D$ ) [130, 131]. The grain boundary conductivity is about two orders of magnitude smaller than the corresponding bulk values, which is again the same ratio as in Ref. [16]. All together, the geometry dependence of all fit parameters, the absolute values of grain boundary thickness and bulk conductivity and the reasonable activation energies indicate that indeed bulk and grain boundaries were successfully separated in a 100 nm thick YSZ layer of 20 nm grain size.

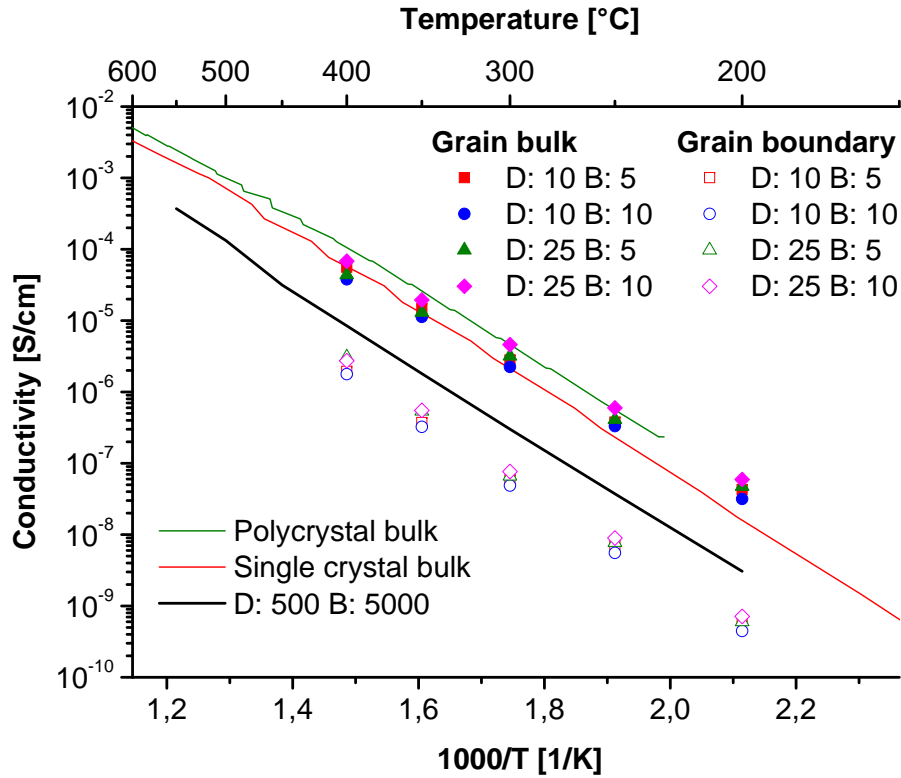


Figure 4.8: ARRHENIUS plot of the conductivities measured with different electrode geometries on layer A (105 nm thin). In the caption the corresponding distances ( $D$ ) and widths ( $B$ ) are specified in  $\mu\text{m}$ . The solid red (9.5% YSZ single crystal) and dotted green (8% YSZ polycrystal) lines are macroscopic bulk measurements plotted for comparison. The solid black line is the effective total conductivity of the film measured with geometry (1).

### **Effect of film thickness and crystallinity**

The following section illustrates the influence of grain size and film thickness on the capacitances and resistances in our system. The samples B (18 nm thick) and C (32 nm thick) were quartered and three of the equally sized pieces were annealed for 1, 3, and 5 hours at 1000°C. Subsequently, impedance spectra were recorded for each of these pieces. A geometry with 5 μm broad and 25 μm spaced interdigital electrodes was used in these investigations. As the measurements on the as-prepared (non-annealed) samples did not yield meaningful results in terms of grain and grain boundary separation, they are not included in the discussion. In Fig. 4.9 the spectra of layer C, annealed for 1 and 5 hours, are compared and the corresponding fit functions are plotted. Again a good approximation by the reduced equivalent circuit in Fig. 4.1(c) is possible and even a slight change in the overall shape of the spectra is visible.

The change of the grain boundary capacitances with annealing time is illustrated in Fig. 4.10(a). The capacitance increases with annealing time, probably due to an increase in grain size  $d_G$  caused by crystallization (see eq. 4.3). Since the increase of the grain boundary capacitance is about a factor of 2 for layer C, the grain size should also have doubled provided the grain boundary thickness remains constant. However, such an increase in grain size could not be verified by AFM. Thus, also chemical or crystallographic changes at the grain boundaries decreasing the electrical grain boundary width  $d_{GB}$  cannot be excluded. The ratio of the grain boundary capacitances for different film thickness but identical annealing times amounts to  $C_{GB}(C)/C_{GB}(B) = 1.4$  (1 hour) and 1.6 for (5 hours), and hence approaches the ratio of the layer thicknesses (1.8). This is a very reasonable result since exactly 1.8 can only be expected, if after annealing both layers had equal  $d_G/d_{GB}$  ratio.

The normalized stray capacitance is plotted in Fig. 4.10(b) and does not change with annealing time. This is in agreement with our model and eq. 4.4, where the stray capacitance only depends on the electrode geometry, which is the same for both layers. It

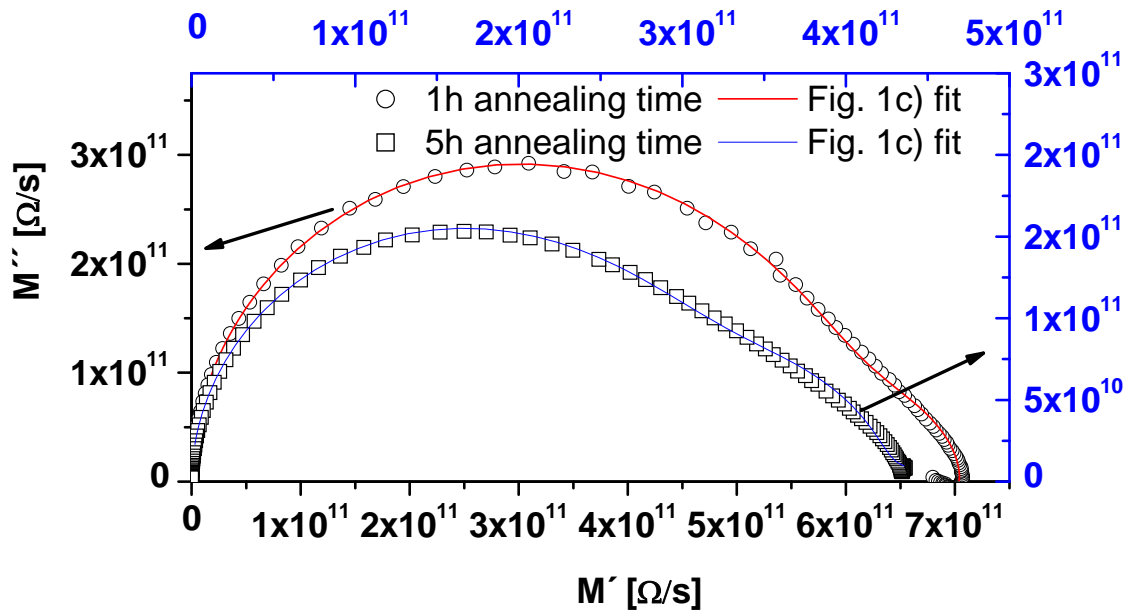
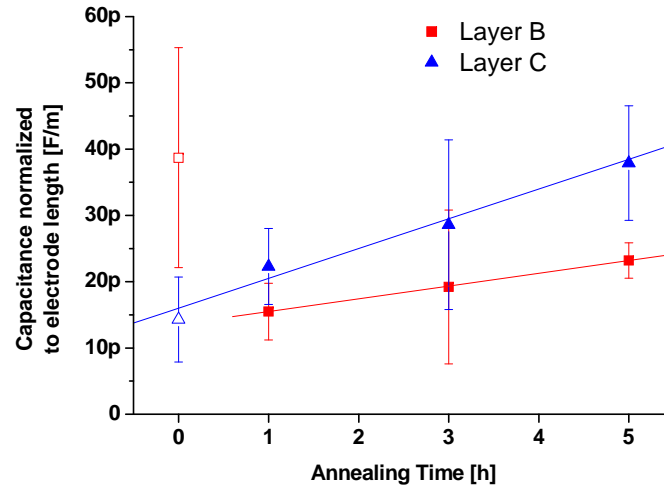
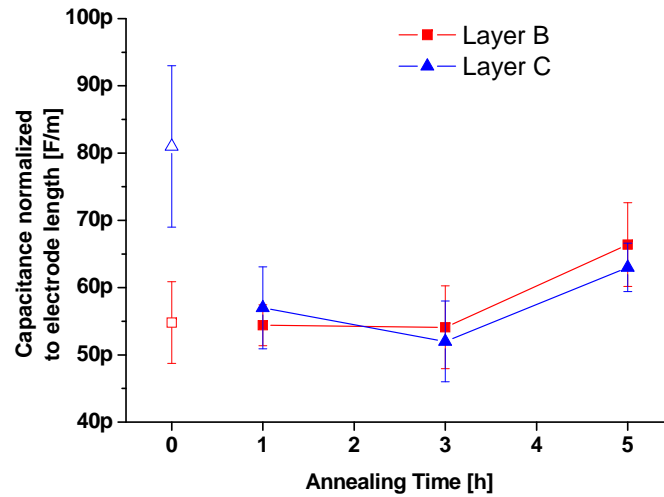


Figure 4.9: Modulus plot of impedance spectra recorded on layer C (32 nm thin) at 300°C. Please note the different scalings used for the spectra in order to allow easier comparison. The open circles (black axis scale) correspond to 1 h annealing time at 1000°C, the open squares (blue axis scale) to 5 h at 1000°C. The solid red and blue line represent the corresponding fit functions obtained by using the equivalent circuit depicted in Fig. 4.1(c). In both cases the electrode geometry consisted of 25  $\mu\text{m}$  spaced 5  $\mu\text{m}$  broad electrodes. The arrows indicate the appropriate axis scales.



(a) Grain boundary capacitance  $C_{GB}$



(b) Stray capacitance  $C_{Stray}$

Figure 4.10: (a) Change of grain boundary capacitance and (b) substrate stray capacitance with annealing time for layer B and C at 1000°C. The solid lines in (a) are linear fits of the data. The stray capacitances plotted in (b) are not calculated by eq. 4.6, but values of  $Q$  were taken for  $r > 0.98$ . The values and the error bars in (a) and (b) are calculated from several spectra recorded at temperatures from 250 to 550°C. The open symbols in (a) and (b) at 0 h annealing indicate that meaningful fit results could not be obtained in that case.

#### 4 The separation of grain and grain boundary impedance in thin YSZ layers

thus further supports the correct interpretation of the elements in the reduced equivalent circuit.

Comparing the resistances of the different annealing states of layer B and C is more complicated. Firstly, the layers may have crystallized to a different degree after the same annealing time and, secondly, grain size and thus also grain boundary width is unknown. The normalized resistances obtained after 1 and 5 ,hours of annealing at 1000°C for grain bulk and grain boundaries of layer B and C are listed in Table 4.3. The ratio of the bulk resistances,  $R_{Bulk}(C)/R_{Bulk}(B)$ , for the shorter annealing time is about 0.25, and therefore smaller than the ratio of the inverse layer thickness of about 0.56. However, for longer annealed samples, a ratio of 0.52 is measured, which suggests that then both layers have crystallized to a comparable degree and exhibit the same bulk conductivity. This is in very good agreement with the XRD analysis, which resulted in the same lattice parameter for both annealed samples. The ratio of normalized grain boundary resistances changes from 0.5 to 0.25 with increasing annealing time, which reflects an opposite trend compared to the bulk resistance. This means that the grain boundary resistance of the thinner layer is indeed larger, but does not simply scale with the inverse thickness. Rather, also the grain boundary conductivity might differ for annealed films of different thickness. Grain size and grain boundary thickness variations are less probable, because the capacitance ratio is almost correct.

The ARRHENIUS plot in Fig. 4.11 shows the bulk conductivities calculated from the fit results. The results after 5 hours annealing time are very close to the bulk conductivities of macroscopic samples again supporting the conclusion that the separation into resistive contributions works and that after 5 hours annealing at 1000°C films are sufficiently crystalline. Reasons for the deviation of the film conductivities from macroscopic samples at higher temperatures have already been mentioned above. Bulk as well as grain boundary activation energies are summarized in Table 4.3 and again reflect the trend well known from macroscopic polycrystals [85]: The grain boundary activation

Table 4.3: Stray and grain boundary capacitances as well as activation energies for transport through grain bulk and grain boundaries (GB) and the corresponding resistances at 300°C measured on layer B and C with different annealing times. Capacitances and resistances are normalized to the electrode length. Measured stray capacitances are averaged over values of  $Q$  with  $r > 0.98$  for the constant phase element in Fig. 4.1(c).

Sample	Annealing Time at 1000°C [h]	$C_{GB}$ [pF/m]	$C_{Stray}$ [pF/m]	$R_{Bulk}$ at 300°C [GΩcm]	$R_{GB}$ at 300°C [GΩcm]	$E_a$ Bulk [eV]	$E_a$ GB [eV]
B (18 nm thickness)	0	40 ± 20	55 ± 6	7.3 ± 0.1	7.9 ± 0.2	0.82	0.89
	1	16 ± 4	54 ± 3	1.95 ± 0.05	4.64 ± 0.05	0.99	1.12
	3	20 ± 10	54 ± 6	1.66 ± 0.05	5.75 ± 0.05	0.88	1.18
	5	23 ± 3	66 ± 6	0.69 ± 0.04	4.01 ± 0.06	0.87	1.10
	0	14 ± 6	81 ± 10	0.44 ± 0.05	5.11 ± 0.05	0.85	1.38
C (32 nm thickness)	1	22 ± 6	57 ± 6	0.53 ± 0.03	2.17 ± 0.03	0.88	1.21
	3	30 ± 10	52 ± 6	0.49 ± 0.02	1.46 ± 0.02	0.93	1.11
	5	38 ± 9	63 ± 4	0.36 ± 0.01	1.18 ± 0.01	0.91	1.13
	0	14 ± 6	81 ± 10	0.44 ± 0.05	5.11 ± 0.05	0.85	1.38

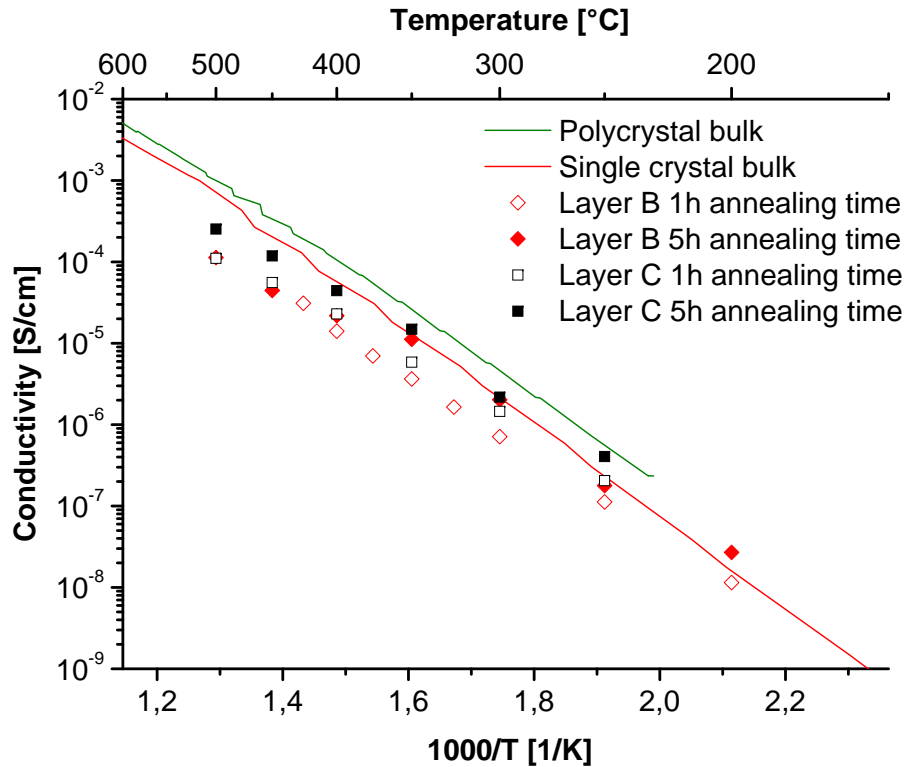


Figure 4.11: ARRHENIUS plot of the grain bulk conductivities measured on layer B (18 nm thickness) and C (32 nm) with different annealing times at 1000°C. Bulk conductivities of macroscopic samples are plotted for comparison (9.5 % YSZ single crystal and 8 % YSZ polycrystal).

energy of about 1.1 to 1.2 eV is larger than that of the bulk (ca. 0.9 eV). All together, also the measurements on films of different thickness and annealing time confirm that a separation into grain and grain boundary impedance contributions can be successful with optimized electrodes even on films as thin as ca. 18 nm.

## 4.4 Conclusions

Modeling with finite element calculations, analytical considerations and simulation of impedance spectra illustrate that measurements using the generally employed electrode geometries usually result in high stray capacitances, which hinder separation of grain and grain boundary effects. Such considerations also suggest that an optimized electrode

#### 4 *The separation of grain and grain boundary impedance in thin YSZ layers*

geometry may enable separation of grain and grain boundary contributions to electrical impedance spectra even for very thin ion conducting layers. The optimization strategy consists of preparing long, thin, and closely spaced stripe electrodes, which strongly reduce the masking effect of the substrate stray capacitance. This can most easily be realized when arranging the electrodes interdigital. Even though in Nyquist plots separation may not be seen, modulus plots show distinct grain and grain boundary contributions.

In order to experimentally test the suggested approach, YSZ thin films were deposited on sapphire single crystals using pulsed laser deposition and were characterized by impedance spectroscopy. The drastic effect of different electrode geometries on the stray capacitance, and thus on the shape of the spectrum (particularly in the modulus plot), was demonstrated on a fully crystalline layer. The influence of layer thickness and grain size was studied on films annealed for different times. All recorded spectra could be fitted by the suggested equivalent circuit, cf. Fig. 4.1(c), and the resulting bulk conductivities correlate well with bulk values obtained on macroscopic reference samples. The grain boundary capacitance showed the expected dependency on electrode geometry and film thickness and yielded a grain boundary thickness of 1 nm. The stray capacitance did only depend on electrode geometry and was neither influenced by the annealing time nor by the YSZ film thickness. Consequently, the properties of all fit elements support the initial considerations.

Hence, we conclude that a separation of grain and grain boundary effects can be achieved in YSZ layers as thin as 20 nm by means of impedance spectroscopy and that this method is a promising tool for further studies also on other ion conducting thin films.

# Chapter 5

## The grain and grain boundary impedance of sol-gel prepared thin layers of yttria stabilized zirconia (YSZ)

### 5.1 Introduction

In this chapter, the technique introduced in chapter 4 of using long, thin and closely spaced electrodes arranged interdigitally to separate bulk and grain boundary impedance in thin films is applied to YSZ layers prepared by the sol-gel route described in chapter 3.1. Grain and grain boundary conductivities are evaluated in the temperature range from 200 to 500°C and are compared for different layer thicknesses. This chapter is, by the time of this writing, submitted for publication as a scientific paper in the journal *Solid State Ionics* [19].

## 5.2 Experimental Results and Discussion

### 5.2.1 Microstructure of the YSZ films

#### Film Thickness

Five YSZ layers were prepared with different rotational speeds during spin coating (see chapter 3.1), hereafter denoted as A, B, C, D, and E, with A being the one prepared using the slowest speed. The rotational speeds during spin coating and the film thickness of each layer are given in Table 5.1.

As expected, there is an inverse relationship between rotational speed and YSZ film thickness. Layer E (28 nm), obtained after 50 % dilution of the sol, was half as thick as layer D (63 nm) for the same rotational speed.

#### AFM measurements

The grain sizes, also given in Table 5.1, were evaluated using the linear intercept method i.e. counting the grain boundaries along straight lines in the AFM images in Fig. 5.1 (a) to (d) and subsequent computer based statistical evaluation. Two different grain shapes can be distinguished in the AFM images in Fig. 5.1. Layer B, see Fig. 5.1(a), exhibits dome-shaped and rather symmetric grains of about 300 nm width. In Fig. 5.1(b) and (c), showing the thinner layers C and D, also a second grain morphology of asymmetric and flat grains emerges (marked by arrows), hence the grain size given in Table 5.1 is an average over both morphologies. The thinnest layer E (Fig. 5.1(d) 28 nm thin) consists only of very large and extremely flat grains. Also some pores can be seen which reach down to the substrate, see arrow in Fig. 5.1(d) . Unfortunately the AFM measurements of layer A were not suitable for grain size evaluation due to surface contaminations most likely from unremoved electrode material. AFM images of layer B to E were taken before electrode preparation.

Table 5.1: Physical and electrical parameters of the YSZ layers under investigation, as well as the activation energies of macroscopic reference samples for comparison. All thin films were annealed at 1200°C for 12 hours. GB means grain boundary,  $E_a$  activation energy.

Sample Name	Rotating speed [rpm]	Film thickness [nm]	Grain size [nm]	$E_a$ Total [eV]	$E_a$ Bulk [eV]	$E_a$ GB [eV]	GB thickness [nm]
Layer A	1800	168 ± 7	-	1.03 ± 0.03	0.92 ± 0.04	-	-
Layer B	3600	100 ± 7	310	1.09 ± 0.01	1.01 ± 0.01	1.11 ± 0.01	2.2 ± 0.1
Layer C	7200	95 ± 4	260	1.09 ± 0.01	0.99 ± 0.00	1.11 ± 0.01	2.4 ± 0.1
Layer D	12000	63 ± 3	260	1.10 ± 0.01	0.96 ± 0.02	1.13 ± 0.01	2.1 ± 0.1
Layer E	* 12000	28 ± 1	440	1.15 ± 0.01	1.20 ± 0.02	1.14 ± 0.02	3.5 ± 0.6
YSZ polycrystal	-	-	-	-	1.05	1.17	-
YSZ single crystal	-	-	-	-	1.11	-	-

\* Sol for the preparation of layer E was diluted 1:1 with 10 % vol. HNO<sub>3</sub> conc. in 2-propanol, see chapter 3.1

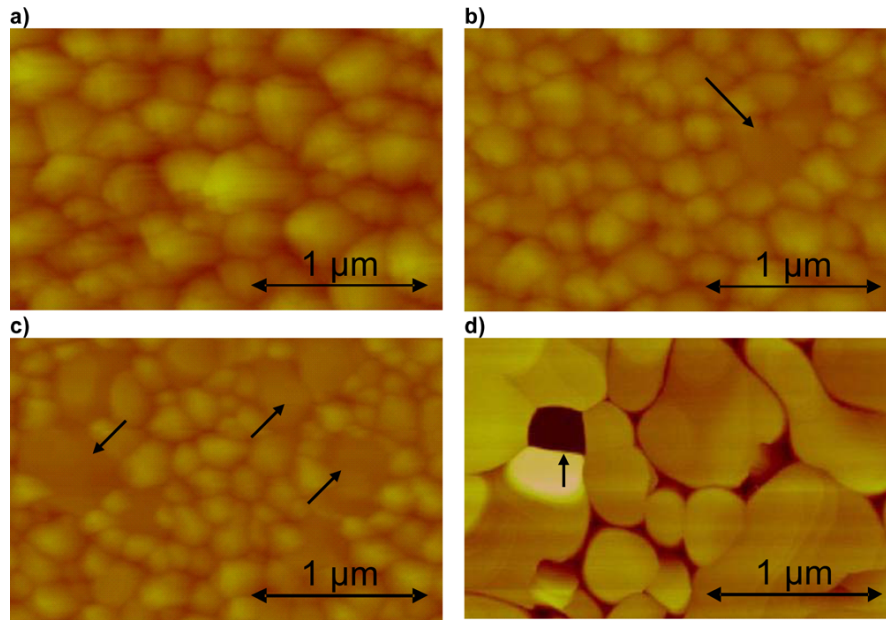


Figure 5.1: AFM images of the surfaces of (a) layer B, (b) layer C, (c) layer D, and (d) layer E. The arrows in (b) and (c) mark examples of different grain morphology. The arrow in (d) marks a pore.

### XRD measurements

The XRD patterns in Fig. 5.2 show magnifications of the YSZ (200), Fig. 5.2(a), and (111), Fig. 5.2(b), peaks recorded for all layers. Since the (200) and (100) plane are in parallel, only the latter is referred to in the following discussion. RIETVELD analysis of the XRD patterns showed an increasing texture parallel to the (100) plane with decreasing film thickness as can be seen in Fig. 5.2(a). The thinnest layer E is strongly oriented along the [100] direction with no other visible reflexes. On the other hand, there is a dominating texture in the [1 1 1] direction for the thicker layers, see Fig. 5.2(b). Only the thickest layer A is little textured, the grains being randomly orientated like in a sample prepared from powder. The experimental half-width of the high angle reflexes in the XRD pattern for the thinnest layer E could only be explained by including strain. However, for a reliable numeric evaluation more sophisticated XRD measurements are

required. Strain values of a very similar system published elsewhere are listed below [47].

These results suggest the existence of a strained region at the YSZ|Al<sub>2</sub>O<sub>3</sub> interface of all layers consisting of large epitaxially grown grains, which is in excellent agreement with the data shown in Ref. [136]. This two dimensional large island growth is favoured by the virtually defect free surface of the sapphire substrate. In contrast, surfaces with a higher defect density tend to form smaller grains with a (1 1 1) orientation [47]. A study modelling this behaviour can be found in Ref. [137]. On top of this interface region, a part of the layer is largely textured in the (1 1 1) direction and exhibits smaller grains. All material above this second textured region (layer A) is randomly oriented.

### 5.2.2 Electrical properties of the YSZ films

As shown in Ref. [18] and chapter 4, the special electrode configuration used here allows separation of bulk and grain boundary properties via impedance spectroscopy. In Fig. 5.3 an example of an impedance spectrum is shown, together with a fit result using the equivalent circuit in the inset of Fig. 5.3(b). An ARRHENIUS diagram of the grain and the grain boundary conductivities is given in Fig. 5.4(b), in Fig. 5.4(a) the total conductivity is plotted for comparison. The grain boundary values are normalized to the electric grain boundary width obtained from the grain boundary capacitance, see eq. 4.3 and chapter 4 for a detailed discussion. The activation energies of these measurements are given in Table 5.1, along with the electrically relevant width of the grain boundary.

The total conductivities plotted in Fig. 5.4(a) are all, with the exception of layer A, very similar and about one order of magnitude smaller than the bulk conductivity of a macroscopic polycrystal. At lower temperatures, layer A exhibits significantly higher conductivities and a lower activation energy than the other layers, which is most likely related to additional proton conductivity, cf. Refs. [138–141]. The fact that this feature is solely observed for layer A can be caused by macroscopically visible cracks, which offer

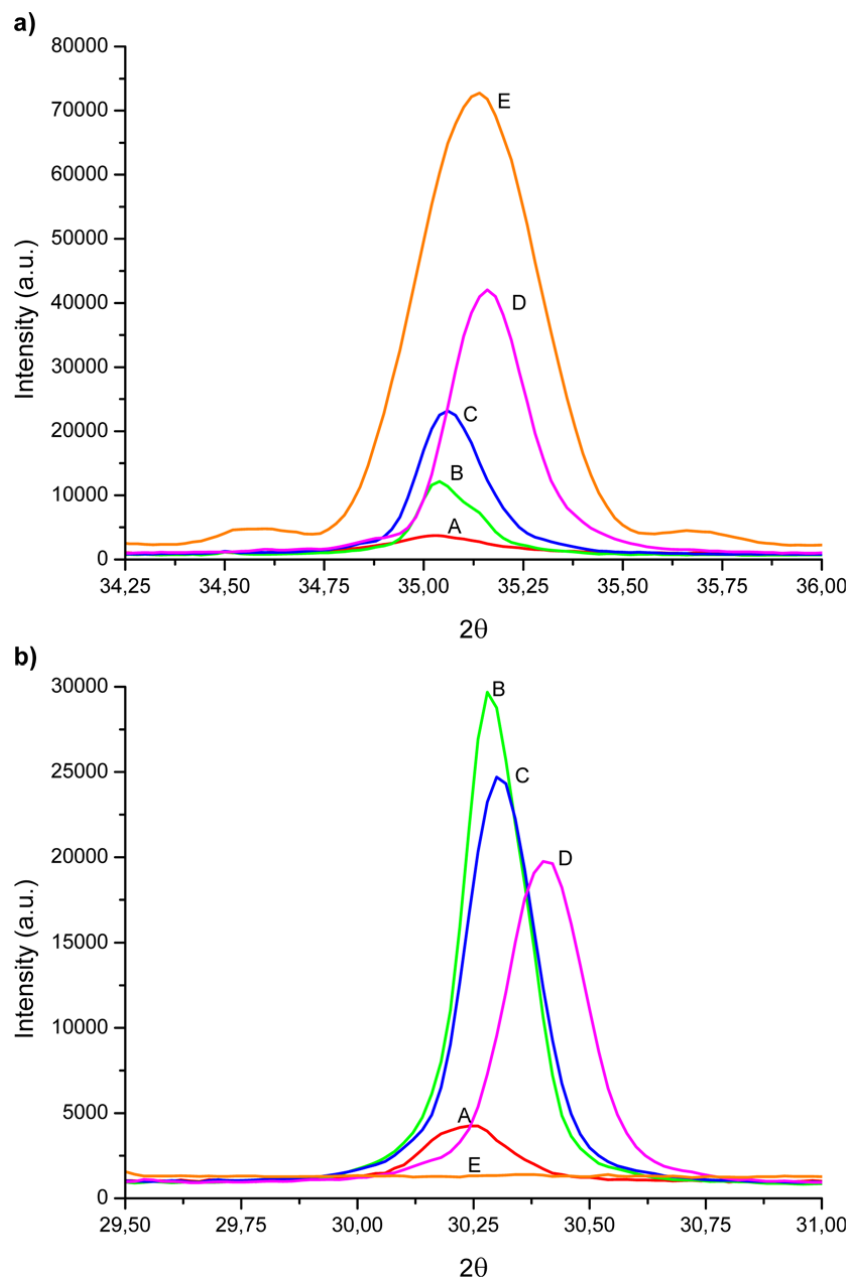


Figure 5.2: XRD patterns of the YSZ (a) (200), (b) (111) reflections of layers A to E.

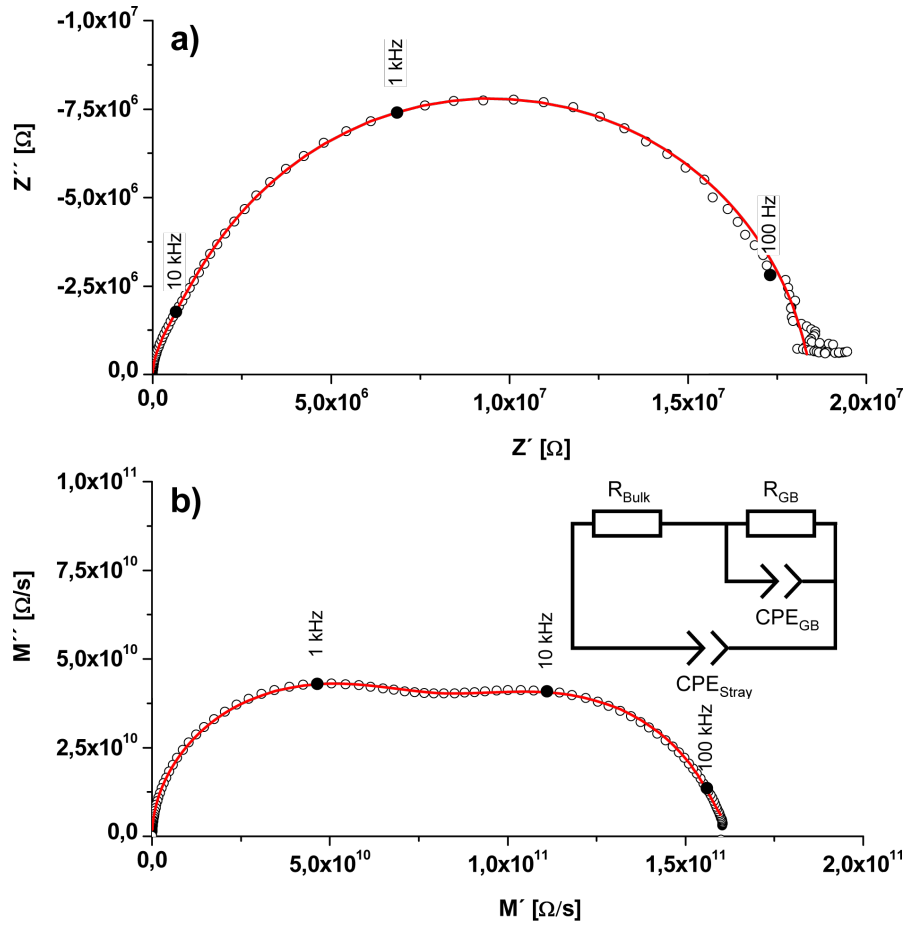


Figure 5.3: Impedance spectrum of layer D at 350°C in (a) Nyquist and (b) Modulus plots. The inset in (b) depicts the equivalent circuit to fit the data, see chapter 4.  $R_{Bulk}$  and  $R_{GB}$  are the resistances for bulk and grain boundaries in YSZ.  $CPE_{GB}$  and  $CPE_{Stray}$  are the constant phase elements used to model the grain boundary and stray capacitance, see Ref. [18] and chapter 4.

an additional adsorption area for ambient water and could lead to proton conducting paths [138]. All other layers exhibited no cracks visible under an optical microscope or in the AFM images.

The bulk conductivities of the layers, shown in Fig. 5.4(b) correlate very well to each other and also to the macroscopic reference samples (except layer A at lower temperatures, see above). The activation energies for ion conduction in the grain bulk of layers A to D (ca. 1.0 eV, for A only the highest temperatures are considered) are in good agreement with the value of our macroscopic polycrystalline material of 1.05 eV or to 1.08 eV as given in Ref. [16].

For layer E a higher bulk activation energy and a lower bulk conductivity for lower temperatures is evaluated which we attribute to the strain found in the XRD measurements. Particularly the higher activation energy cannot be caused by the certain porosity visible in Fig. 5.1(d). The influence of strain on oxygen ion transport in YSZ thin films has recently been dealt with in a series of experimental studies [15, 24, 29, 30, 142]. It was found that a tensile strain in YSZ increases the ionic conductivity in an interface region and decreases the activation energy of ion transport, while a compressive strain has the opposite effect. In Ref. [47] large heterogeneous strains of 6.8 % and -7.5 % have been evaluated for the b and c direction of large epitaxial (100) grains on a (0001) sapphire substrate, which is the case for layer E, therefore we expect similar values. However, the beneficial effect of a tensile strain has been calculated to have a maximum at about 4 % [25], hence the strain in layer E is expected to have only impeding influence on ion transport. The absolute value of the activation energy for grain bulk transport of about 1.2 eV is in good agreement with the values reported in Ref. [30], where it increases from 1.1 eV for small strains to almost 1.3 eV. However, one has to keep in mind that the latter values include both grain bulk and grain boundary conduction.

The grain boundary conductivities and the respective activation energies of all layers do not differ within the error margin. The absolute conductivities are about two orders

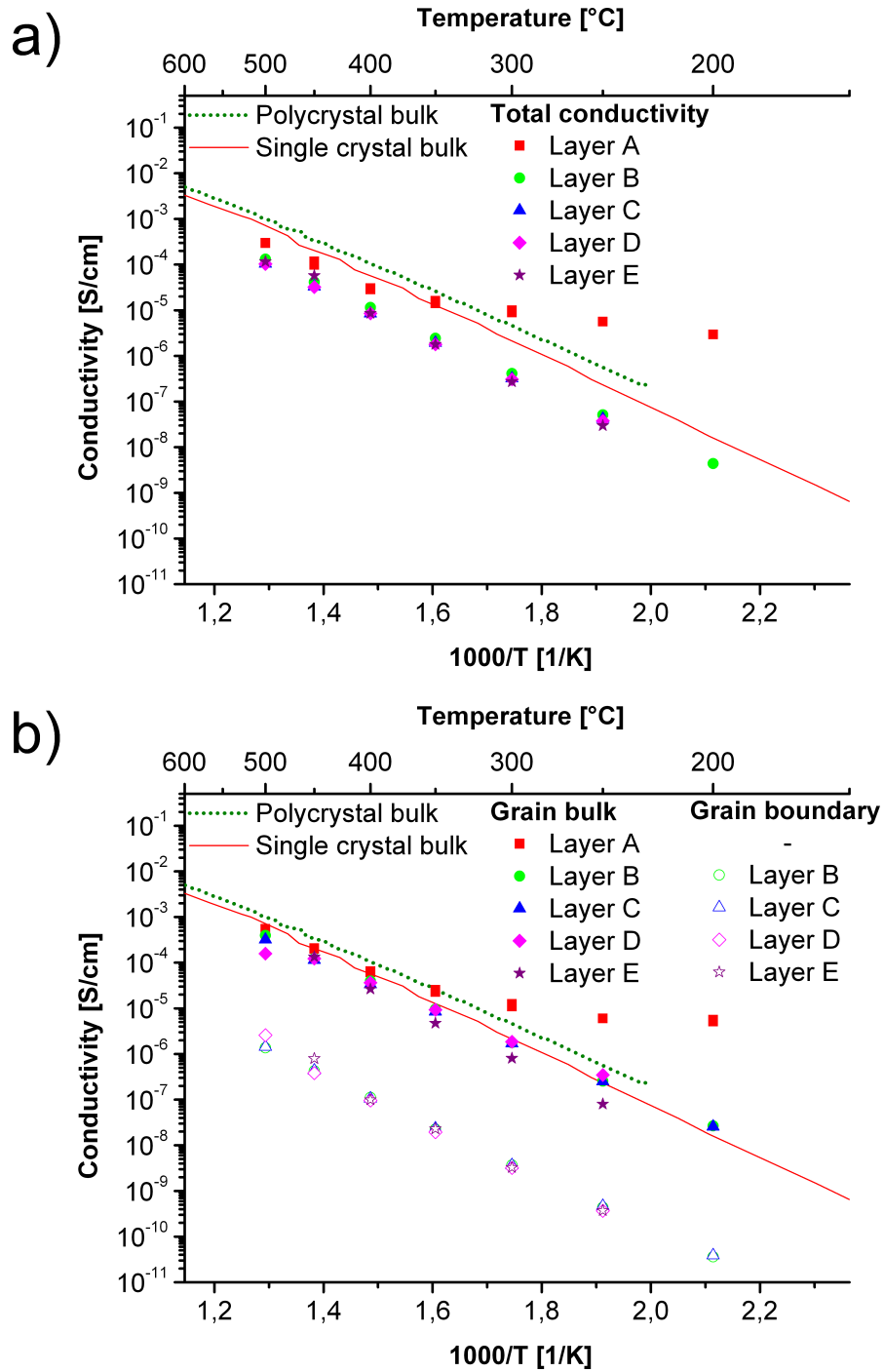


Figure 5.4: ARRHENIUS plots of (a) the total conductivities and (b) the grain and grain boundary conductivities measured on layers A to E. The red and green lines are macroscopic bulk measurements plotted for comparison.

of magnitude smaller than the bulk values, which is generally explained by depletion of oxygen vacancies in the space charge regions adjacent to the grain boundaries [85]. The activation energy of oxygen transport through the grain boundaries of about 1.10 eV compares well to 1.15 eV in Ref. [16] (thicker layers) or 1.14 eV in Ref. [18] (thin PLD layers). Hence, all these results are in good agreement with previous studies on thin films and macroscopic crystals [16–18, 85].

The electrically relevant thickness of the grain boundaries, given in Table 5.1, was calculated from the grain boundary capacitance and the grain size from AFM measurements (see eqs. 4.6 and 4.8). It does not include effects due to a possible variation of the grain-size perpendicular to the surface caused by the transition from (1 0 0) to (1 1 1) texture. Layers B to D all have a very similar grain boundary thickness of about 2.2 nm for grain sizes of 260 nm (layer C and (d) and 310 nm (layer B), which is about half the size usually obtained on macroscopic samples and also on thicker layers [16]. For layer E with a grain size of 440 nm, a larger grain boundary thickness of 3.5 nm is calculated. For comparable grain sizes, values of 5.4 nm - measured on several 100 nm thick layers [16] - and 5 nm [73] or 5.4 nm [72] - measured on macroscopic polycrystals - can be found. However, in contrast to our data on layers B to E all these results were obtained on samples showing no crystallographic texture. In a previous study, we reported a grain boundary thickness of merely 1.0 nm for YSZ layers thinner than 100 nm with a grain size of about 20 nm, which were grown by pulsed laser deposition and were strongly textured in the (1 1 1) direction [18], see chapter 4 and Table 4.2. Hence, the low grain boundary thickness especially of layers B to D might be due to the fact that these layers are also textured to a high degree in the (1 1 1) direction. However, in order to verify the assumption that the width of the electrically relevant grain boundary region depends on the orientation between two adjacent grains, further investigations are required.

### 5.3 Conclusions

Polycrystalline YSZ layers of thicknesses between about 30 and 170 nm were prepared on single crystalline sapphire substrates using a sol-gel route. AFM investigations revealed two different grain morphologies, which could be linked to two different textures found in subsequent XRD measurements: Large and flat grains textured in the (100) plane and small dome-shaped grains textured in the (111) plane. The (100) texture becomes more pronounced close to the layer|substrate interface, with the (111) grains growing on top of them. Thicker layers become increasingly untextured close to the surface. For the thinnest of the investigated layers XRD also revealed a strain, which can be correlated with an increased activation energy of oxygen ion transport in the grain bulk. Apart from that the conductivities of grain bulk and grain boundaries and the corresponding activation energies of all layers hardly differ from each other and from macroscopic reference samples. These results also further demonstrate the advantages of an optimized electrode geometry in separating grain bulk and grain boundary impedance even in very thin layers.

# Current driven tracer incorporation in thin films of YSZ

## 6.1 Introduction

In this chapter a two step method to measure lateral oxygen tracer diffusion profiles in thin film YSZ is introduced. It consists of a tracer incorporation step aided by a direct current at lower temperatures and a subsequent diffusion step at elevated temperatures. While the method proved successful it was tedious to reproduce. However, the results paved the way for the development of an easier incorporation step, which is introduced in chapter 7. The results on layer S have been published in Ref. [17].

## 6.2 Methodology

The following two step method was designed to investigate oxygen tracer diffusion in the YSZ films:

- $^{18}\text{O}$  tracer incorporation takes place at one electrode in  $^{18}\text{O}_2$  atmosphere under a continuous current flow between the two electrodes. Provided mixed conducting

electrodes with low polarization resistance are used, this electrochemical pumping should lead to a narrow region of high oxygen tracer concentration in the gap area close to the cathode, see Fig. 6.1. The reason for the limitation of the tracer incorporation to the edge region of the mixed conducting cathode is the very high lateral ohmic resistance of the film compared to the low oxygen incorporation resistance of the cathode. After tracer incorporation, the mixed conducting electrodes (here LSC, see chapter 3) are removed chemically and the resulting  $^{18}\text{O}$  profile is investigated by TOF-SIMS.

- The main diffusion experiment is then carried out in UHV at a temperature being higher than that used during oxygen incorporation (step one). The final  $^{18}\text{O}$  profile is measured after quenching the sample. Since the second step is performed in UHV  $^{18}\text{O}$  stays in the film during diffusion and a protection layer on YSZ is not needed. This gives a large flexibility in choosing or modifying the surface of the YSZ layer for the actual diffusion experiment.

### 6.3 Experimental results and discussion

Results from two samples are presented and are representative for a successful (layer S) and a failed experiment (layer F), which nonetheless helped to devise the strategy presented in chapter 7. Layer S was prepared by pulsed laser deposition (PLD) with a thickness of 145 nm, layer S, called layer B in Table 5.1, was prepared by a sol-gel route and is 100 nm thick, see chapter 5.

The samples were kept for 10 minutes at 300°C in an atmosphere of 200 mbar  $^{18}\text{O}_2$  to allow the fast oxygen exchanging LSC electrodes to equilibrate. Then a direct current of 500 nA (layer S, 5  $\mu\text{m}$  electrode spacing) or 1  $\mu\text{A}$  (layer F, 10  $\mu\text{m}$  electrode spacing) was applied to the electrodes for 20 minutes in order to locally pump  $^{18}\text{O}$  into the YSZ

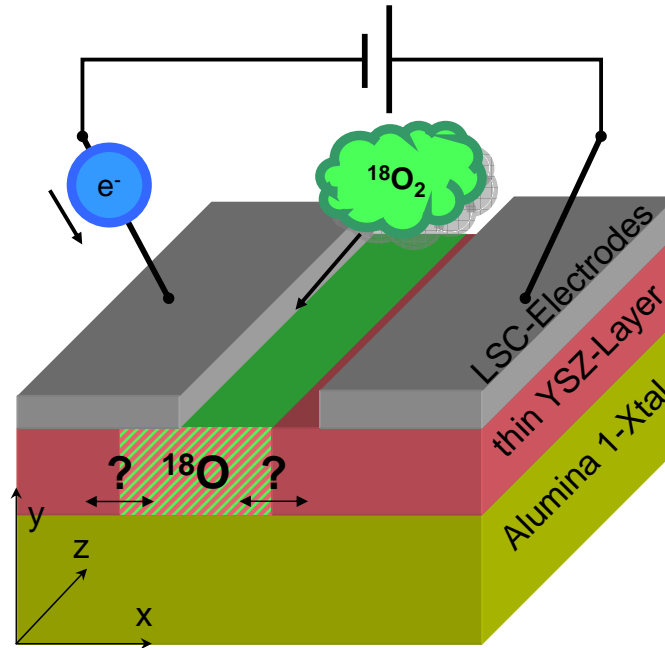


Figure 6.1: Sketch of the set-up for the current driven tracer incorporation. The question marks indicate that the exact implantation area is yet unknown

layer (see sketch in Fig. 6.1). Afterwards the samples were cooled to room temperature which completes the first step.

### 6.3.1 Results on layer S

#### Step 1: Current supported tracer incorporation

In Fig. 6.2 the lateral  $^{18}\text{O}$  concentration profile of layer S after the tracer incorporation is plotted, along with top-view and cross-sectional ion images. The ion images recorded by TOF-SIMS in Fig. 6.2(a) and (b) clearly display that a confined area of the YSZ layer between the LSC electrodes has been enriched with the oxygen tracer. The cross-sectional view of the profile in Fig. 6.2(a) illustrates that in this  $^{18}\text{O}$  “rectangle” the entire depth of the film (y-direction) is filled by a virtually constant  $^{18}\text{O}$  concentration. The top view image in Fig. 6.2(b) shows that the area is not of perfect rectangular shape, most likely due to non-ideal electrode edges. However, this roughness of about  $2.5\ \mu\text{m}$  is small

compared to the width of the final diffusion zone aimed at in step two. The resulting lateral concentration profile integrated over the entire  $z$ -direction of Fig. 6.2(a) is plotted in Fig. 6.2(c). The half width of the profile amounts to  $13\ \mu\text{m}$ , while the top plateau is  $8\ \mu\text{m}$  broad. The plateau concentration corresponds to about  $28\%$   $^{18}\text{O}$  with respect to the total oxygen content, cf. eq. 2.37. The width of the initial profile is somewhat surprising, since enrichment was only expected near the three phase boundary of the cathodically polarized LSC electrode. It is also larger than the nominal gap between the LSC electrodes. This broadening might be caused by some local reduction of YSZ due to the high electric field, or also a sufficiently high entropy driven tracer exchange of the free YSZ surface, cf. 7, but further investigations are necessary for final clarification. On the other hand, the almost rectangular shape of the resulting profile even simplified the analysis of the data obtained in the following second step of the experiment.

### **Step 2: Lateral tracer diffusion**

After removing the LSC electrodes and depositing a dense platinum layer perpendicular to the tracer enriched area (see Fig. 7.2(c) in chapter 7), the main diffusion step was carried out in the UHV of the TOF-SIMS instrument. The sample was placed on a heating stage, heated to  $500^\circ\text{C}$ , held at this temperature for 90 minutes and then cooled down to room temperature. Mass spectra were recorded both underneath the platinum layer and on the uncovered YSZ surface. The ion images in Fig. 6.3(a) and (b) illustrate, how the initial box-shaped profile has broadened during the heat treatment. Obviously, the two step tracer diffusion experiment was performed successfully. For the special case of diffusion from a rectangular initial distribution an analytical solution of FICK's second law of diffusion exists [105] and is given in eq. 7.3 in chapter 7. Owing to the similarity of the measured initial profile and a rectangular initial profile, the concentration profiles in Fig. 6.3(c) were fitted to eq. 7.3 with the diffusion time being set to 90 minutes and the initial concentration to  $28\%$   $^{18}\text{O}$ .

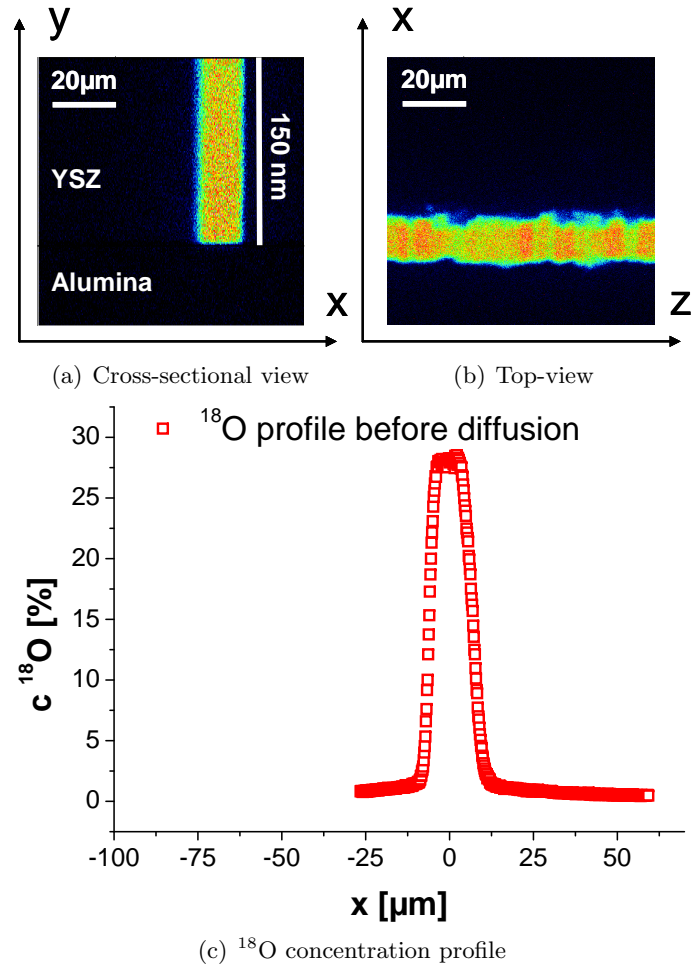


Figure 6.2: Situation after the tracer incorporation step: TOF-SIMS ion images of layer S in (a) side-view and (b) cross-sectional view of the  $^{18}\text{O}$  concentration  $c_{^{18}\text{O}}$  calculated by eq. 2.37. (c) Lateral concentration profile integrated along the x-axis. The x, y and z directions are the same as in Fig. 6.1.

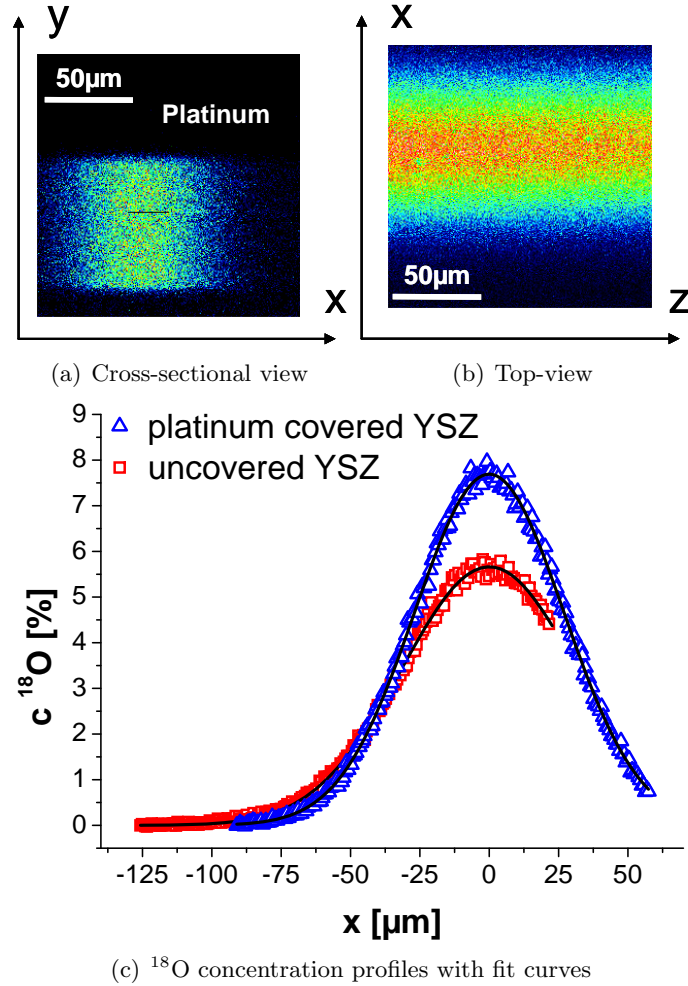


Figure 6.3: Situation after the tracer diffusion step: TOF-SIMS ion images of layer S in (a) side-view and (b) cross-sectional view of the  $^{18}\text{O}$  concentration  $c_{^{18}\text{O}}$  calculated by eq. 2.37. (c) Two lateral concentration profiles integrated along the x-axis measured under a free YSZ surface or a Pt-covered one, respectively. The black fit curves were calculated with eq. 7.3. The x, y and z directions are the same as in Fig. 6.1.

## 6 Current driven tracer incorporation in thin films of YSZ

The initial extensions of the tracer-enriched box  $2 \cdot h$  resulting from the fit (15.8 and 18.5  $\mu\text{m}$ ) are somewhat larger than the half width of 13  $\mu\text{m}$  measured before the diffusion experiment. However, since some broadening during heating to the actual diffusion temperature may play a role and a certain roughness or width variation of the initial profile can affect the results, this is a reasonable agreement. Comparing the profiles and the diffusion coefficients with ( $6.4 \cdot 10^{-10} \text{ cm}^2/\text{s}$ ) and without Pt top layer ( $9.0 \cdot 10^{-10} \text{ cm}^2/\text{s}$ ) it seems that the free surface slightly accelerates the effective oxygen diffusion. However, the findings in chapter 7 could not support this claim. Previously published tracer diffusion coefficients on bulk materials are in the same range. For example in Ref. [112] and [71] YSZ single crystals with 9.5 mol% yttria (9.5-YSZ) were investigated and both groups report a tracer diffusion coefficient  $D^*_{500^\circ\text{C}}$  of approximately  $5 \cdot 10^{-10} \text{ cm}^2/\text{s}$ , while in a similar study on 10-YSZ single crystals a  $D^*_{500^\circ\text{C}}$  of about  $9 \cdot 10^{-10} \text{ cm}^2/\text{s}$  was measured [113]. Results for 8-YSZ can be found in Ref. [76], where a  $D^*_{500^\circ\text{C}}$  of  $2.7 \cdot 10^{-10} \text{ cm}^2/\text{s}$  is reported for polycrystals with a grain size of about 50 nm. All these values are relatively close to each other and agree well with the results in the present study.

### 6.3.2 Results on layer F

After the success of the experiments on layer S, reproduction of the results on different layers unfortunately proved to be quite difficult. In Fig. 6.4 the lateral  $^{18}\text{O}$  concentration profile and ion images after the unsuccessful tracer incorporation experiment in layer F are shown. The LSC electrodes have been locally removed in the measured area with a small drop of hydrochloric acid, but most of the electrodes were still intact.

The cross-sectional ion image in Fig. 6.4(a) apparently shows a wavy interface between the YSZ layer and the sapphire substrate, while in Fig. 6.2(a) a sharp interface is visible, even though in both cases the same sapphire single crystals with polished surfaces have been used. However, the sol-gel prepared YSZ layers in this thesis generally exhibited

a slightly wavy surface morphology which developed in the spin-coating process, while the PLD grown layers are almost ideally flat. Due to the alternating sputtering and analysing during the TOF-SIMS measurement (see also chapter 2) the undulating surface morphology of the sol-gel prepared layers is projected onto the YSZ|substrate interface. The top-view in Fig. 6.2(b) and the lateral profile in (c) show that the  $^{18}\text{O}$  concentration is not confined to the gap area between the former LSC electrodes. On the contrary, a high concentration is found throughout the entire YSZ layer and only a comparatively small concentration difference between the plateau of about 10%  $^{18}\text{O}$  under the former LSC electrodes and 14%  $^{18}\text{O}$  in the gap area has formed. No well defined concentration box, i.e. with a steep concentration drop at the edges, could be achieved as shows in the lateral  $^{18}\text{O}$  profile in Fig. 6.2(c). Also the width of the non-ideal concentration box is close to 20  $\mu\text{m}$  and therefore considerably larger than the electrode spacing of nominally 10  $\mu\text{m}$ .

Such a profile is obviously not suitable in a meaningful subsequent diffusion experiment, as no defined boundary conditions can be deduced in order to employ eq. 7.3. However, since a significant amount of  $^{18}\text{O}$  tracer had been incorporated in the gap area and the LSC electrodes were still intact on most of the surface of the YSZ layer, the sample was heat treated for 10 minutes at 300°C on a hot stage. Since the mixed conducting LSC very quickly exchanges oxygen with ambient air at elevated temperatures, the idea behind this experiment was to reduce the  $^{18}\text{O}$  tracer concentration in the YSZ layer beneath the electrodes by using LSC as an oxygen drain. The  $^{18}\text{O}$  concentration in the uncovered YSZ film between the electrodes was expected to stay more or less constant, as YSZ has a very low surface exchange coefficient. Hopefully this would lead to a more defined starting profile of a more pronounced box shape.

The surprising result of the above experiment is presented in Fig. 6.5. The ion images in Fig. 6.5(a) and (b) show that the  $^{18}\text{O}$  concentration was dramatically reduced in the gap between the former LSC electrodes, which have again been locally removed before

the TOF-SIMS measurement. The bar-like  $^{18}\text{O}$  concentration profile initially aimed for is inverted. The width of the depleted region is  $10\ \mu\text{m}$ , which is exactly the spacing of the LSC electrodes. From the lateral concentration profile in Fig. 6.5(c) it is obvious that the  $^{18}\text{O}$  concentration underneath the former LSC electrodes is relatively stable at about 12%, which is even slightly higher than in Fig. 6.4(c). However, this could be caused by e.g. only local contacts of the LSC film to the current-collecting platinum plates and the resulting electronic sheet resistance of the mixed conducting electrodes [62]. Therefore it is not unlikely that the current density during the incorporation experiment was not constant over the length of the electrodes and marginally varying amounts of tracer have been incorporated in different areas. However, regardless of what the exact tracer concentration before the experiment might have been in this exact spot, the gap region between the former LSC electrodes lost at least 10 percentage points in tracer concentration compared to the situation before the heat treatment in Fig. 6.4(c). The  $^{18}\text{O}$  concentration in the YSZ layer beneath the electrodes, on the other hand, appears to have stayed largely unchanged. It seems as if the LSC electrodes have acted more like a protective layer than the desired oxygen drain. Moreover, the YSZ surface exchange coefficient proved high enough to extremely decrease the tracer concentration in the uncovered area of the YSZ layer.

## 6.4 Conclusions

The results presented in this chapter are kind of mixed. On the one hand, the successful experiments on layer S showed that it is indeed possible to conduct lateral diffusion experiments, i.e. to use current driven  $^{18}\text{O}$  tracer incorporation to achieve a high concentration box shaped profile at low temperatures in thin film YSZ. In a second step at elevated temperatures this “starting” profile then broadened into a diffusion profile, which can be excellently fit to an analytical solution of the diffusion problem.

On the other hand, the results on layer F illustrate that the first step is not easily

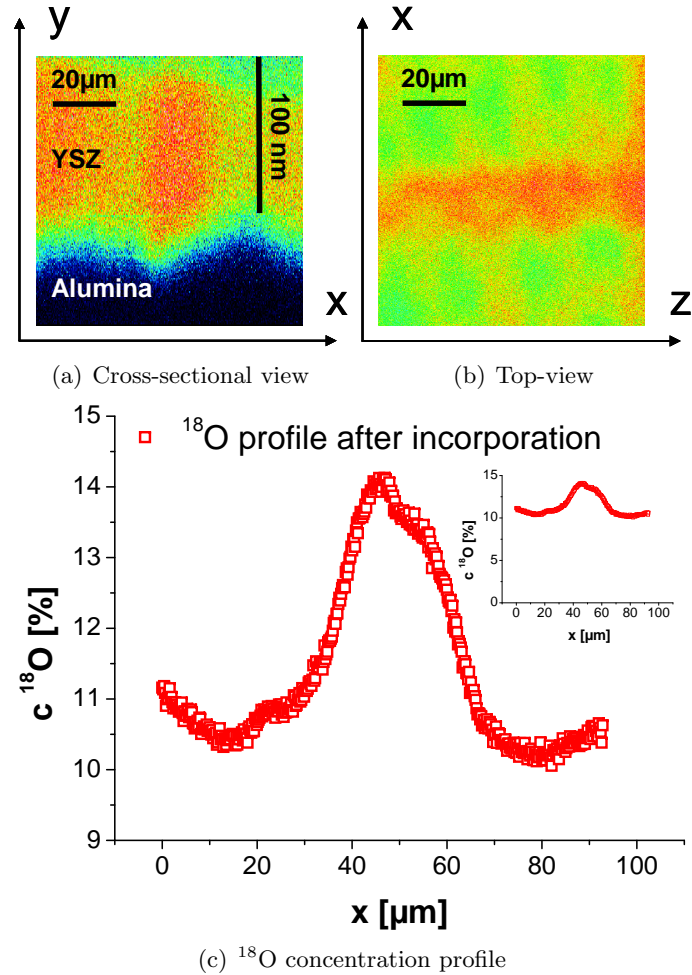


Figure 6.4: Situation after the tracer incorporation step: TOF-SIMS ion images of layer F in (a) side-view and (b) cross-sectional view of the  $^{18}\text{O}$  concentration  $c_{^{18}\text{O}}$  calculated by eq. 2.37. (c) Lateral concentration profile integrated along the x-axis, the inset shows the data with a different scaling of the y-axis. The x, y and z directions are the same as in Fig. 6.1.

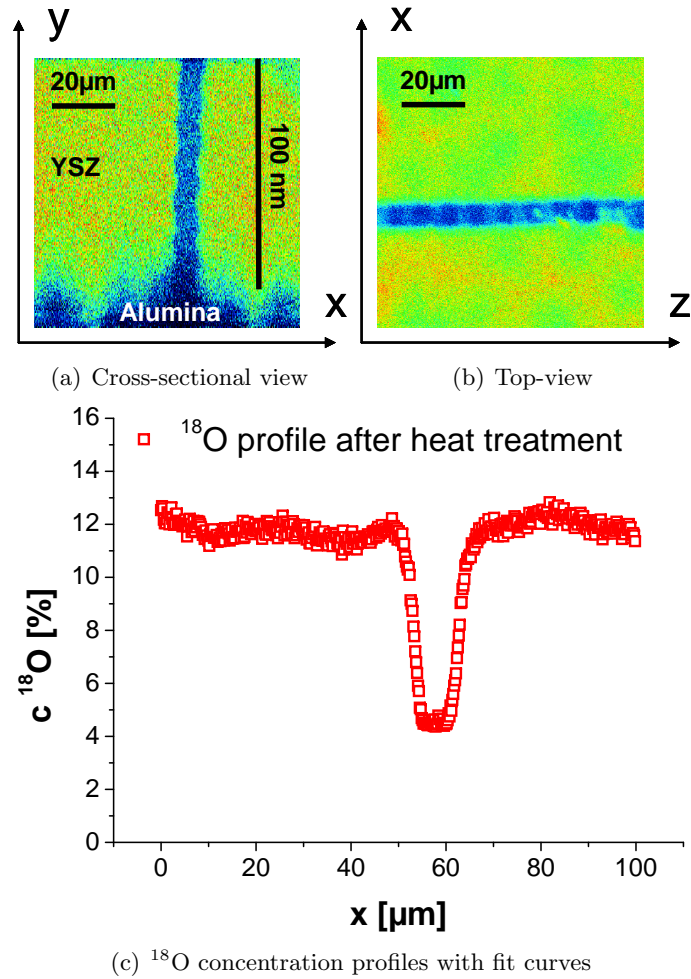


Figure 6.5: Situation after a 10 minute heat treatment at 300°C: TOF-SIMS ion images of layer F in (a) side-view and (b) cross-sectional view of the  $^{18}\text{O}$  concentration  $c_{^{18}\text{O}}$  calculated by eq. 2.37. (c) Lateral concentration profile integrated along the x-axis. The x, y and z directions are the same as in Fig. 6.1.

reproducible, as with similar starting conditions a completely different and, for our aims, useless profile was achieved after the tracer incorporation experiment. This has been a problem in several other attempts, which have not been included here, as they offer no additional information. No definite explanation can be given as to why these experiments were unable to produce such an excellent box profile as in layer S. However, in Ref. [66] it was shown how sensitive the oxygen exchange kinetics of PLD grown LSC electrodes react to changes in the temperature during laser deposition. Since almost no increase in  $^{18}\text{O}$  tracer concentration was found beneath the LSC electrodes in layer S, it seems a feasible hypothesis that these particular electrodes had a comparatively low surface exchange coefficient. Alternatively the surface exchange coefficient may have been reasonably large, but a high resistance at the LSC|YSZ interface may have prevented a significant tracer incorporation into the YSZ layer. Given the more numerous failed attempts it is most likely that the incorporation experiment in layer S was more of a lucky shot.

However, while being completely unexpected and unsuccessful, in terms of actually measuring lateral tracer diffusion coefficients, the findings on layer F still provided valuable input for further experiments: During the short heat treatment at a slightly elevated temperature, originally intended to achieve the desired box profile, a surprisingly large amount of  $^{18}\text{O}$  tracer was released through the plain YSZ surface resulting in an inverted box profile (see Fig. 6.5(c)). Therefore also a reversal of the process should be possible: By covering parts of the surface of the YSZ film with a gas tight protective layer a defined region could be enriched with the tracer ions. These protective layers can be prepared by magnetron sputtering of metals, a much faster and easier experiment than the tedious PLD process necessary for preparing LSC electrodes. Also, since no electrical contacting is necessary, it should be possible to perform the tracer incorporation step on several YSZ films simultaneously. In chapter 7 an in depth study of lateral tracer diffusion in thin YSZ layer is described, which also proves the above concept of purely entropy driven tracer gas exchange in the first step.

# Tracer diffusion studies in thin film YSZ

## 7.1 Introduction

In this chapter the conductivity data of YSZ thin films on different substrates, gathered using impedance spectroscopy, are compared to ionic diffusion coefficients obtained from complementary lateral tracer diffusion experiments. Combined with structural analysis, using atomic force microscopy and X-ray diffraction, it is aimed to clarify whether or not fast ion conduction is present in some of the YSZ layers. It also includes data demonstrating the feasibility of an improved version of two step tracer diffusion experiments in thin films (cf. chapter 6). This chapter is, by the time of this writing, submitted for publication in the journal *Physical Chemistry Chemical Physics* [143].

## 7.2 Theoretical considerations

YSZ has a rather small oxygen surface exchange coefficient compared to mixed conducting materials such as  $(\text{La,Sr})(\text{Co,Fe})\text{O}_3$  LSCF, e.g. Ref. [144–146]. The ionic conductivity, however, is very high. Therefore, tracer exchange experiments on YSZ are usually conducted at comparatively high temperatures and for long times in  $^{18}\text{O}_2$  enriched atmospheres to reach a satisfying tracer concentration level. Depth profiles in thin YSZ

layers are very difficult to realize [147]. Accordingly, mainly lateral (in-plane) diffusion is feasible and this requires very dense protection layers on YSZ to avoid surface exchange of oxygen on the top plane. In such a lateral one-dimensional diffusion experiment from a constant source, the resulting concentration can be described by [105, 112]

$$\frac{c(x, t) - c_{bg}}{c_{gas} - c_{bg}} = \operatorname{erfc}\left(\frac{x}{2\sqrt{D^* \cdot t}}\right) - \exp(h \cdot x + h^2 D^* \cdot t) \cdot \operatorname{erfc}\left(\frac{x}{2\sqrt{D^* \cdot t}} + h\sqrt{D^* \cdot t}\right). \quad (7.1)$$

Symbol  $c$  denotes the relative concentration of the tracer (tracer fraction),  $c_{bg}$  the relative background concentration of the tracer,  $c_{gas}$  the relative tracer concentration of the gas environment,  $x$  is the distance from the surface and  $t$  the diffusion time;  $h = k^*/D^*$  reflects the ratio of the surface tracer exchange coefficient  $k^*$  and the tracer diffusion coefficient  $D^*$ . Such in-plane tracer diffusion experiments are possible [36] but highly non-trivial.

In chapter 6 a two step diffusion experiment was suggested, involving current driven tracer implantation into a small, bar-like part of the film at lower temperatures and in-plane diffusion at higher temperatures. In this manner, the aforementioned limitations for in-plane diffusion experiments in the case of thin film YSZ [17] can be overcome. However, while shallow profiles with high tracer concentration could indeed be achieved, the current driven tracer implantation (step 1) proved to be again difficult and it would be advantageous to replace this first step by a more convenient thermal tracer exchange step. Owing to the low oxygen exchange coefficient of YSZ it may at first seem counter-intuitive that simply by entropy-driven thermal oxygen exchange at low temperatures a substantial tracer concentration can be achieved in parts of a YSZ film.

However, when indeed calculating profiles from available literature data of  $k^*$  and  $D^*$  values, a different picture results. A recent study published surface exchange and tracer diffusion coefficients of a 50 nm thin YSZ layer prepared with atomic layer de-

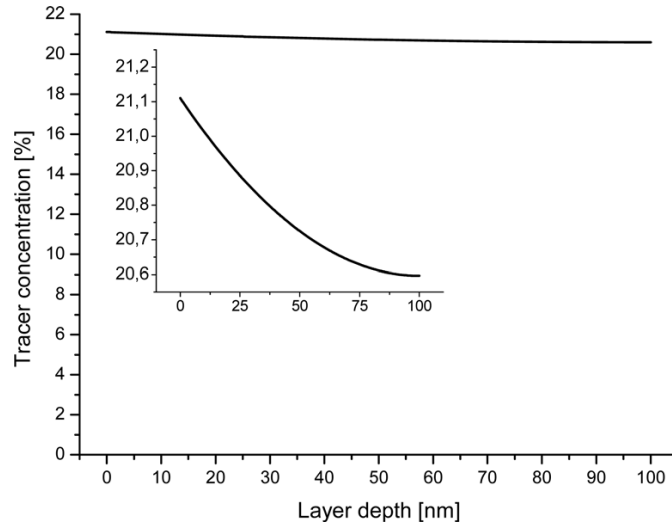


Figure 7.1: Depth profile of the  $^{18}\text{O}$  concentration of a hypothetical 100 nm thin YSZ layer after an entropy driven gas exchange for 30 minutes at  $300^\circ\text{C}$  (incorporation step), the inset shows a magnification of the same profile. Surface tracer exchange coefficient  $k^* = 1 \cdot 10^{-9}$  cm/s and tracer diffusion coefficient  $D^* = 1 \cdot 10^{-12}$  cm $^2$ /s were both taken from Ref. [148]. Background concentration was fixed to 0% and the gas was set to be 100%  $^{18}\text{O}_2$ . The substrate was assumed to be completely blocking for oxygen transport.

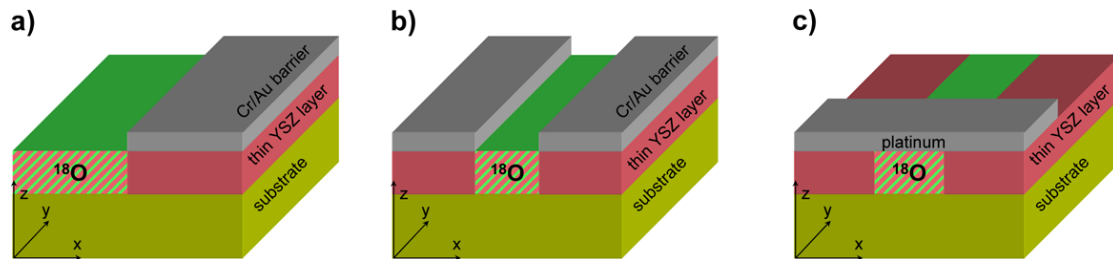


Figure 7.2: Sketches of the two different setups for the tracer incorporation and the tracer diffusion step: In (a) half of the YSZ layer is covered with a metallic barrier layer leading to enrichment of  $^{18}\text{O}$  in the other half. In (b) only a small region in the center of the YSZ layer is exposed to the gas phase leading to a bar-like enriched region. (c) After tracer implementation the barrier is removed and a part of the surface can be modified arbitrarily; here a platinum film is applied normal to the oxygen enriched region (exemplified with a bar-like profile). Then the diffusion step is performed in vacuum.

position on single crystalline YSZ substrates [148]. For 300°C the values of the surface exchange coefficient were approximately  $10^{-9}$  cm/s and the diffusion coefficient in YSZ bulk amounted to  $10^{-12}$  cm<sup>2</sup>/s.

The <sup>18</sup>O concentration depth profile in Fig. 7.1 was determined using these values and finite element calculations assuming a 100 nm thick YSZ layer and thermal exchange for 30 minutes. Obviously the YSZ layer is filled by more than 20 % of tracer ions with only a small variation of 0.5 % from surface to the substrate interface. This high concentration level is the result of the combination of a rather large diffusion coefficient, a small surface exchange coefficient and the relatively thin layer: On the one hand, tracer atoms are incorporated at a low rate and then quickly distributed over the whole film depth, leading to a constant concentration. On the other hand, due to the thin layer, the small total number of exchanged atoms still results in a large tracer concentration.

Lateral diffusion lengths of about 0.5 μm can be expected, which is still sufficiently small compared to diffusion lengths aimed at in the second diffusion step at higher temperatures. It can therefore be expected that by covering approximately half of the YSZ film with a dense barrier layer, cf. Fig 7.2(a), a well defined tracer concentration step can be created. In a subsequent diffusion experiment at higher temperatures, this may then be used to achieve in-plane profiles in thin films according to [105]

$$c(x, t) = \frac{c_0 - c_{bg}}{2} \cdot \operatorname{erf} \left( \frac{x}{2\sqrt{D^* \cdot t}} \right) + c_{bg} \quad (7.2)$$

with  $c_0$  being the height of the initial concentration after the first step. In Fig. 7.3(a) and (b), the calculated concentration profiles of our suggested two step process before and after the diffusion step as well as hypothetical profiles of standard one step in-plane diffusion are plotted. For the latter profiles, it is assumed that the whole film is covered with a dense barrier layer and oxygen is incorporated at the edges or in a scratch as in Ref. [36]. The comparison of the profiles illustrates the advantages of the two step process: It is possible to achieve higher concentrations and steeper concentration profiles

## 7 Tracer diffusion studies in thin film YSZ

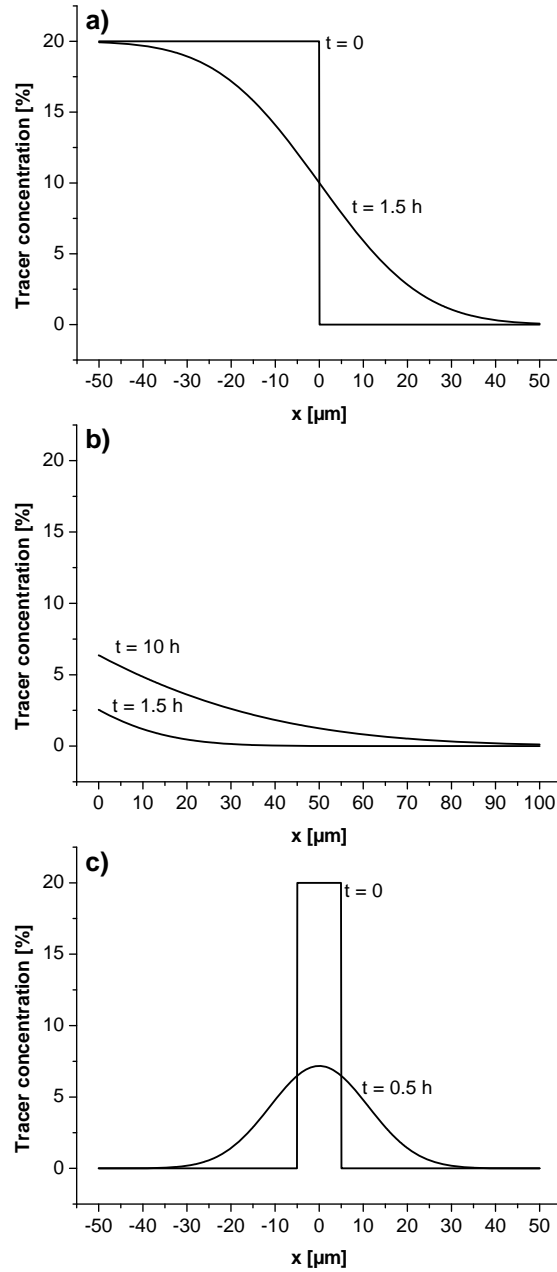


Figure 7.3: A comparison of different lateral diffusion profiles after specified diffusion times at 500°C. (a) An initial semi infinite concentration step is assumed; (b) surface exchange driven diffusion profile according to eq. 7.1, it is assumed that the gas exchange only takes place at the edge of the layer; (c) Profile resulting for an initial finite concentration box. The box width is set to 10  $\mu\text{m}$ . Surface tracer exchange coefficient  $k^* = 6 \cdot 10^{-9}$  cm/s and tracer diffusion coefficient  $D^* = 3 \cdot 10^{-10}$  cm<sup>2</sup>/s were both taken from Ref. [148]. The background concentration was fixed to 0% and the gas was set to be 100% <sup>18</sup>O<sub>2</sub>.

in a shorter experimental time. As a bonus one can also modify the surface of the YSZ film after the exchange step by different top layers instead of being limited to the oxygen diffusion barrier layer.

Alternatively, a box-like starting profile could be used, see Figs. 7.2(b) and 7.3(c). Diffusion of this tracer bar at higher temperatures leads to a concentration profile which can be described by [105]

$$c(x, t) = \frac{c_0 - c_{bg}}{2} \left( \operatorname{erf} \left( \frac{b+x}{2\sqrt{D^* \cdot t}} \right) + \operatorname{erf} \left( \frac{b-x}{2\sqrt{D^* \cdot t}} \right) \right) + c_{bg} \quad (7.3)$$

with  $2b$  being the width of the initial concentration box. The profile after diffusion in Fig. 7.3(c) has a lower maximum concentration than the semi-infinite problem in Fig. 7.3(a) but is still more favourable than the surface exchange controlled one step experiment shown in Fig. 7.3(b).

### 7.3 Experimental results and discussion

In total, eight YSZ layers on different single crystalline substrates have been prepared and analysed in the present study. On strontium titanate and magnesia substrates one layer was prepared by PLD and one by a sol-gel route, see chapter 3.1. On sapphire, two layers of different thickness were deposited by each preparation method. To simplify the following discussion, the films are referenced by substrate and preparation method, see Table 7.1. For the sol-gel prepared layers the YSZ sol was diluted 1:1 with a mixture of 10% vol.  $\text{HNO}_3$  conc. in 2-propanol and a rotation speed of 12000 rpm was applied, except one layer (Sap-SG 2), where the YSZ sol was used pure with a rotation speed of 7200 rpm. After preparation layer MgO-PLD was annealed at 1000°C for 16 hours, because first XRD results showed an insufficient crystallinity.

Table 7.1: Substrates, geometrical parameters and activation energies of bulk and grain boundary (GB) conductivities in the YSZ thin films used in this study. No microstructural features were observed in the AFM image of the surface of STO-PLD, hence the grain size is listed as infinitely large.

Sample	Substrate	Preparation method	Thickness [nm]	Grain size [nm]	$E_a$ Bulk [eV]	$E_a$ GB [eV]
MgO-PLD	MgO	PLD	65	90	0.92	1.3
MgO-SG	MgO	Sol-Gel	50	265	1.22	1.35
Sap-PLD 1	Al <sub>2</sub> O <sub>3</sub>	PLD	28	10	1.02	1.2
Sap-PLD 2	Al <sub>2</sub> O <sub>3</sub>	PLD	250	37	0.94	1.06
Sap-SG 1	Al <sub>2</sub> O <sub>3</sub>	Sol-Gel	28	440	1.20	1.14
Sap-SG 2	Al <sub>2</sub> O <sub>3</sub>	Sol-Gel	70	213	1.02	1.14
STO-PLD	SrTiO <sub>3</sub>	PLD	135	$\infty$	-	-
STO-SG	SrTiO <sub>3</sub>	Sol-Gel	80	265	-	-

### 7.3.1 Microstructure of the YSZ thin films

In Fig. 7.4, diffraction patterns of all investigated layers are shown. Except for layer Sap-SG 2, where also very minor (1 1 0) reflections were found, all layers reveal peaks of the (1 0 0) and (1 1 1) direction of the cubic fluorite structure. Two layers are textured in one orientation, namely Sap-SG 1 in the (1 0 0) and MgO-PLD in the (1 1 1) direction. The (1 1 1) reflection of MgO-PLD also shows by far the highest signal intensity of all observed layers. However, one has to keep in mind that layer MgO-PLD was annealed after preparation to increase the originally insufficient crystallinity. The lattice constants were calculated for each signal and are plotted in Fig. 7.5. While the results for the layers prepared on strontium titanate are quite close to the bulk literature value of 5.14 Å (see for example Refs. [106, 134]), the other layers show slight to strong deviations. The sol-gel synthesized films on sapphire exhibit significantly smaller lattice constants of roughly 5.12 Å, but do not vary much with thickness or direction. The PLD prepared layers on sapphire as well as the sol-gel prepared layer on magnesia show a strong anisotropic lattice distortion, having a much larger value along the (1 1 1) direction compared to the (1 0 0) direction. Also the individual constants for the (1 1 1) directions are well above

the macroscopic literature value of 5.14 Å. Finally, the PLD prepared layer on magnesia exhibits the highest lattice constant found in this study (5.20 Å). These results show that pronounced lattice strains normal to the lattice plane are present in the different YSZ films.

To determine the lateral grain sizes, AFM measurements were performed and are presented in Fig. 7.6. The most obvious observation when comparing the PLD grown layers in Fig. 7.6(a), c), (e) and (g) to their sol-gel prepared equivalents in Fig. 7.6(b), (d), (f) and (h) is the significantly larger grain size of the sol-gel layers. Thin films prepared by pulsed laser deposition usually consist of small columnar grains with a relatively narrow size distribution [23, 32]. This is indeed found for Sap-PLD 1 and 2. The film MgO-PLD exhibits somewhat larger grains than the other PLD prepared layers, which again can be explained by the heat treatment. A notable exception is the layer STO-PLD where no microstructural features can be observed in the AFM image in Fig. 7.6(c). This suggests an epitaxially grown YSZ (1 1 1) layer on SrTiO<sub>3</sub>, however, the XRD data revealed that a very small part of the layer is also oriented in the (1 0 0) direction.

The sol-gel synthesized layers show two different grain morphologies, a comparatively small-sized dome-like shape and large and flat grains. Examples are indicated in Fig. 7.6(d). While Sap-PLD 1 in Fig. 7.6(f) only exhibits the large and flat grain morphology, the other layers show both variants. In layer Sap-SG 2, also a third morphology is visible: In the grain boundaries between the larger grains, smaller crystallites are accumulated. In previous studies it was found that the large and flat grains are (1 0 0) oriented, while the smaller dome shaped ones are aligned in the (1 1 1) direction [19, 47, 137]. Therefore, one may suggest that the additional small-sized particles in Sap-SG 2 are linked to the (1 1 0) direction only found in this layer. However, verification of this assumption was beyond the scope of this study. All film thicknesses and grain sizes are summarized in Table 7.1.

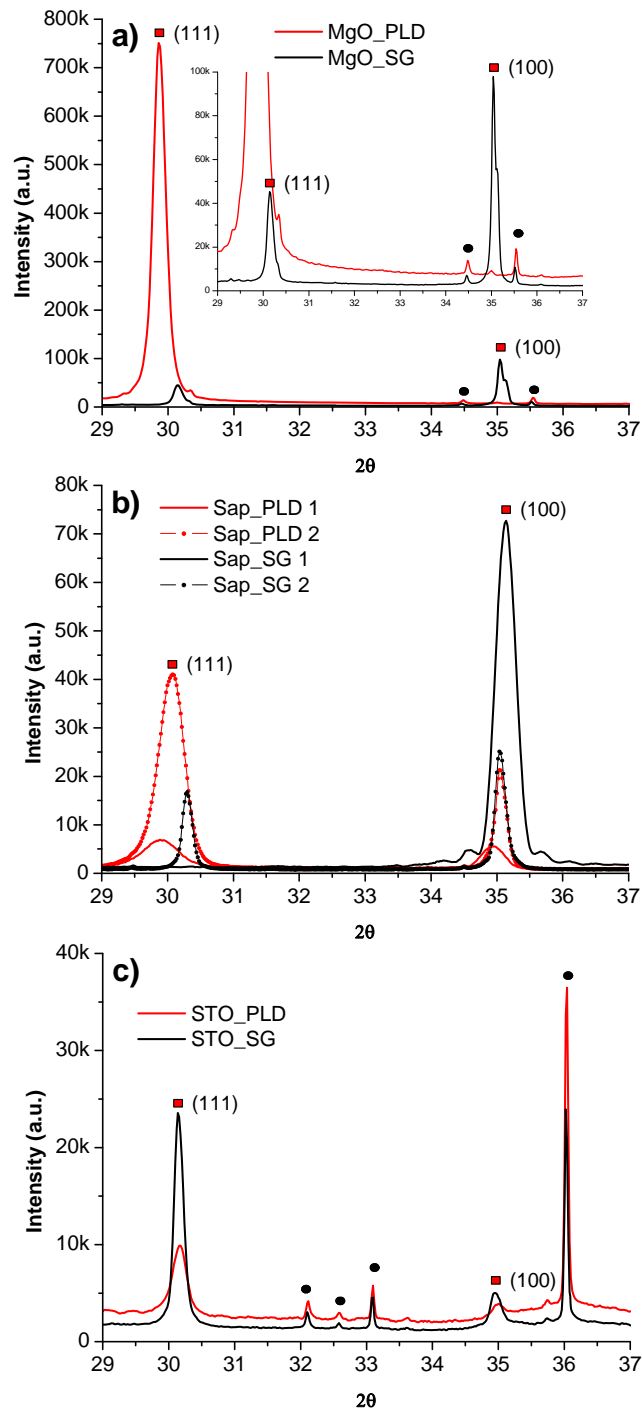


Figure 7.4: XRD patterns of the investigated YSZ layers on (a) sapphire; (b) magnesia; (c) strontium titanate. The black dots in (b) and (c) mark reflections caused by the corresponding substrates. Reflections marked (100) are actually (200) but obviously refer to the same crystallographic orientation. The individual structural parameters can be found in Table 7.1 and Fig. 7.5.

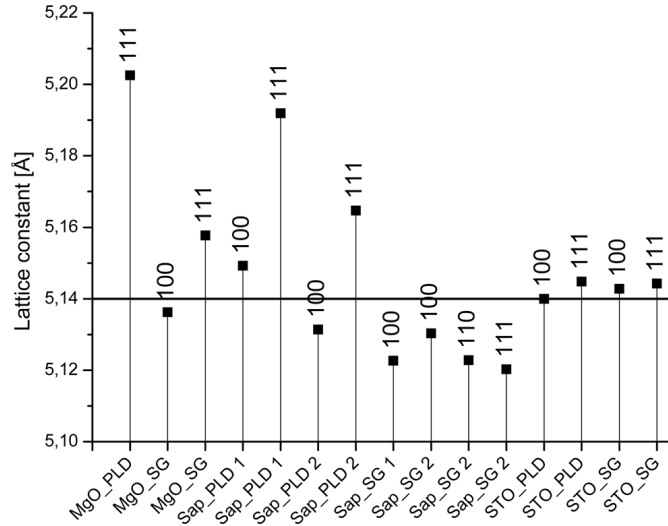


Figure 7.5: Lattice constants of the crystallographic orientations found in the investigated samples. It is important to note that each lattice plane presented here is parallel to the substrate interface plane. The solid line represents the literature value of a macroscopic powder sample, see e.g. Ref. [106].

### 7.3.2 Electrical impedance spectroscopy

In previous work [18], it was shown how long, thin and closely spaced metal electrodes arranged interdigitally can be used in impedance spectroscopic studies to separate grain bulk and grain boundary properties even in very thin layers. This method is again employed here and exemplarily Fig. 7.7 shows impedance spectra and fit curves to the given equivalent circuit. Particularly in the modulus plot the two arc-like features of the grain and grain boundaries become visible. For further information on such measurements and their analysis the reader is referred to Ref. [18] and chapter 4.

ARRHENIUS plots of the resulting grain and grain boundary conductivities are given in Fig. 7.8 for the YSZ films on the different substrates. Grain boundary conductivities are referred to grain boundary thicknesses (2 to 4 nm) deduced from the grain boundary capacitance and the grain size [128, 129].

For comparison, the bulk conductivities of macroscopic YSZ polycrystals are also plotted. For both measurements the activation energy is about 1.04 eV. The solid line

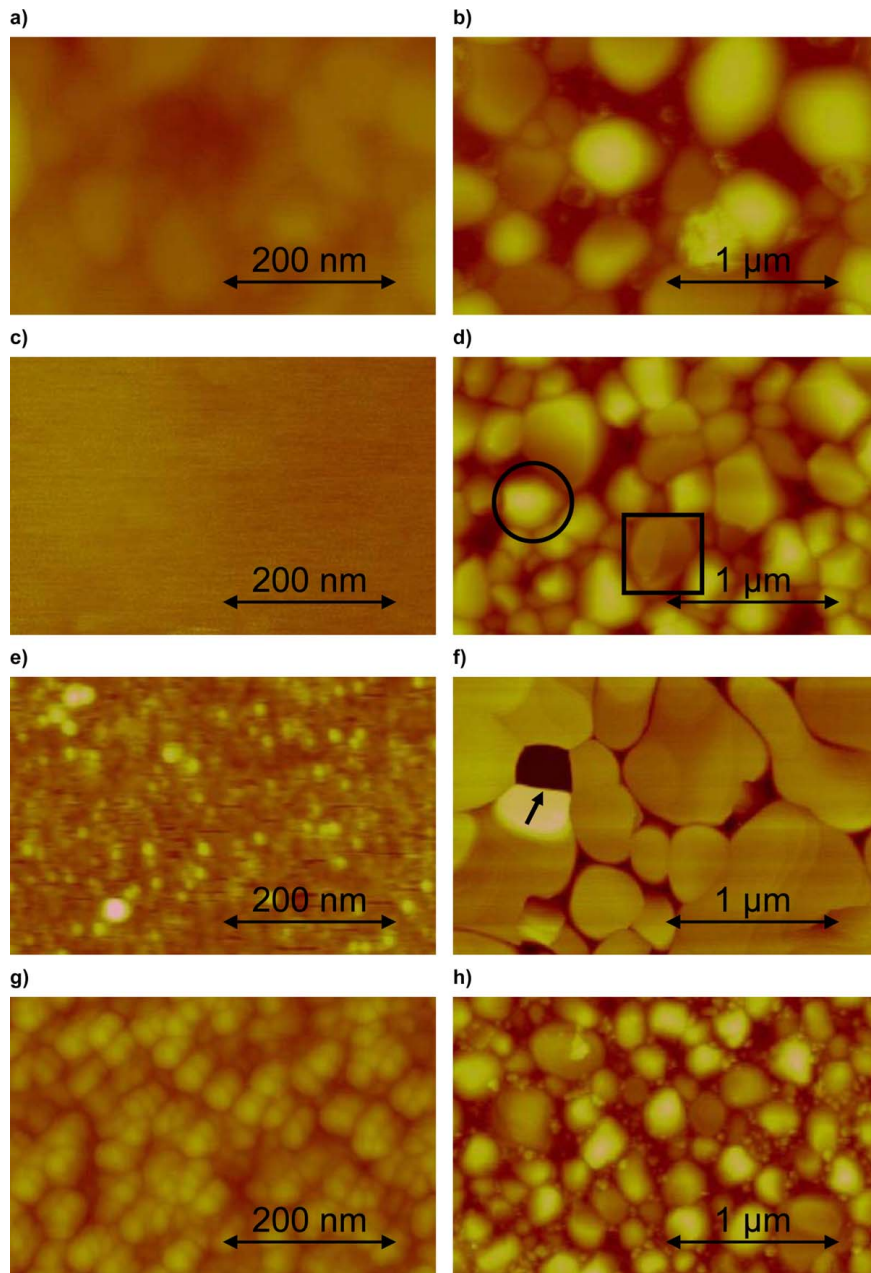


Figure 7.6: AFM images of the surfaces of layers (a) MgO-PLD; (b) MgO-SG; (c) STO-PLD; (d) STO-SG; (e) Sap-PLD 1; (f) Sap-SG 1; (g) Sap-PLD 2; (h) Sap-SG 2. The circle in (d) indicates a dome shaped (111) oriented grain, while the square marks a flat (100) oriented one. The arrow in (f) indicates a pore in the layer which reaches down to the interface.

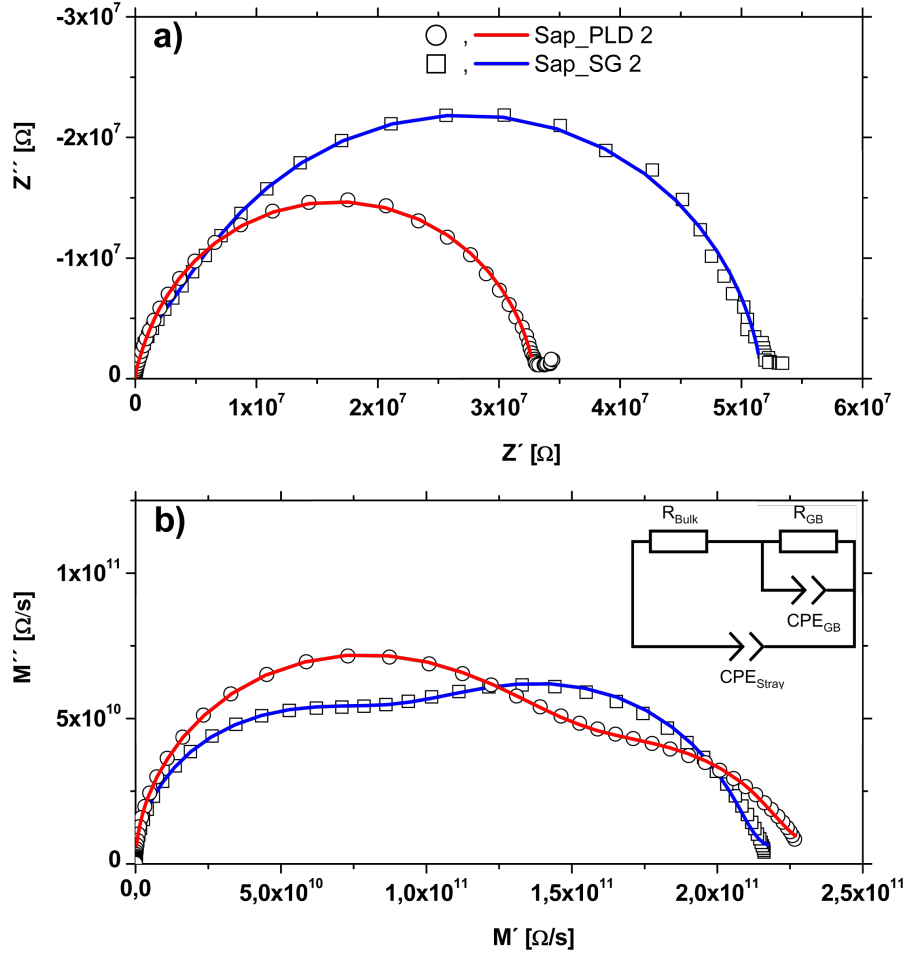


Figure 7.7: Impedance spectra (open symbols) along with the corresponding fit curves (red and blue lines) of Sap-PLD 2 and Sap-SG 2 at 300°C in (a) Nyquist and (b) Modulus plots. The inset in (b) depicts the equivalent circuit to fit the data.  $R_{Bulk}$  and  $R_{GB}$  are the resistances for bulk and grain boundaries in YSZ.  $CPE_{GB}$  and  $CPE_{Stray}$  are the constant phase elements used to model the grain boundary and stray capacitance, see Ref. [18] and chapter 4.

corresponds to a measurement in a tube furnace, hence any temperature error should be negligible. The dotted line is the result of a measurement using interdigital electrodes on a bipolished YSZ polycrystal positioned on the heating stage and thus in the setup also used for the thin film measurements. In this case, the set temperature of the heating stage is higher than that of the truly measured surface-near region of the polycrystal or the YSZ film, respectively. For the polycrystal this unavoidable temperature error amounts to about 30°C to 35°C, cf. Fig. 7.8. However, this rather large deviation may be seen as an upper limit for the thin film measurements, as the single crystalline substrates may have higher thermal conductivity than the YSZ polycrystal. Moreover, the mechanical contact to the heating stage was most probably better for the precisely cut and polished single crystal substrates. Owing to this temperature uncertainty, we always refer data to the set temperature of the heating stage.

In Fig. 7.8(a), the bulk and grain boundary conductivities of the two layers on magnesia are shown. The bulk conductivity of MgO-PLD has a lower activation energy of 0.9 eV compared to 1.3 eV for the sol-gel prepared layer MgO-SG and is larger, particularly in the lower temperature region. Compared to the macroscopic polycrystal, MgO-SG exhibits a significantly lower bulk conductivity. Since these two layers have very different crystallinity and texture, it is difficult to pinpoint the differences to one specific structural property. However, possible explanations include the strong dilative strain normal to the layer plane found in MgO-PLD, which has been shown to facilitate ion transport [29, 30]. Also magnesia has a considerably smaller lattice constant of 0.420 nm [149] than YSZ with nominally 0.514 nm [106]. Therefore the (111) orientation of MgO-PLD might better fit to the substrate than the (100) orientation which is predominant in MgO-SG. The grain boundary conductivities of both layers are quite similar and also the activation energies are comparable, being 1.3 eV in MgO-PLD and 1.4 eV in MgO-SG. While open questions remain, it can be concluded that compared to

7 Tracer diffusion studies in thin film YSZ

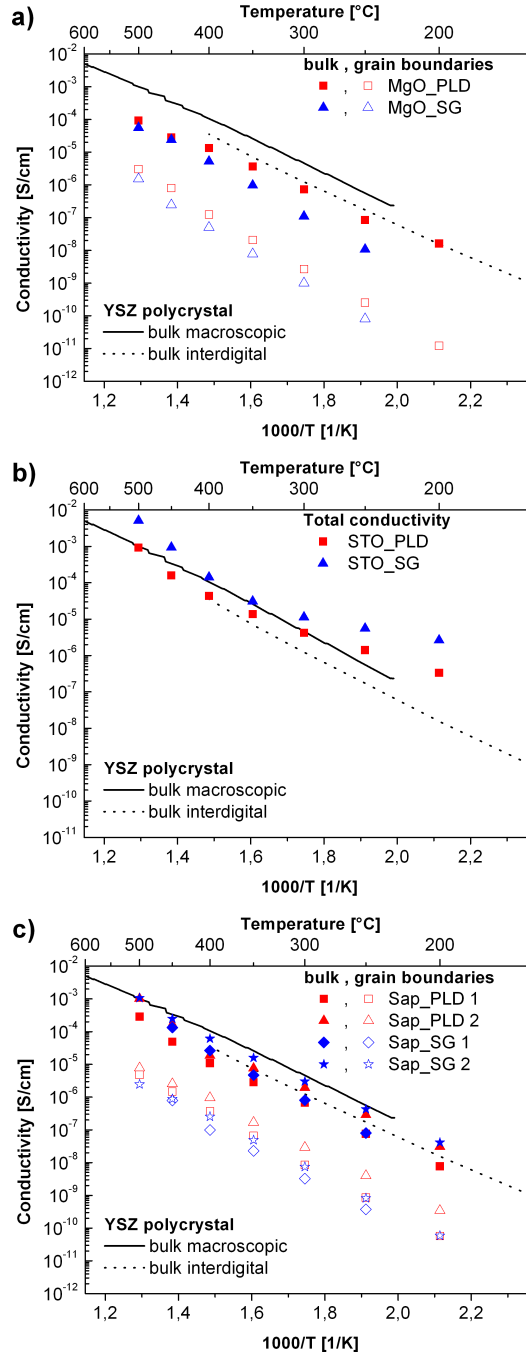


Figure 7.8: ARRHENIUS plots of the conductivities of grain and grain boundaries of the YSZ films on (a) magnesia; (b) strontium titanate; (c) sapphire. The two black lines in each plot are bulk conductivities of 8% YSZ polycrystals. The solid black line consists of data measured in a tube furnace, while the dotted line was measured with interdigital electrodes on a heating stage. In the latter case the geometrical factor relating resistance and conductivity was calculated by the finite element method.

polycrystals no increase in bulk, let alone total conductivity was measured for YSZ on MgO as opposed to Ref. [14].

The results of the YSZ films on strontium titanate in Fig. 7.8(b) show a completely different behaviour. No separation of grain bulk and grain boundaries was possible with impedance spectroscopy, despite using interdigital electrodes. Hence, only a total conductivity could be derived from the total resistance and the film geometry. For both PLD and sol-gel prepared films a change of activation energy from about 0.5 eV at lower temperatures to about 1.5 eV above 350°C is observed. If these effective transport properties truly corresponded to the YSZ layers, then a significant improvement of conductivity had been achieved, especially in the lower temperature region. However, it has to be taken into account that also conduction in the substrate is monitored by impedance spectroscopy. Electronic conduction in the strontium titanate substrate may even completely mask conductivity contributions of the YSZ film. A change in activation energy at about 350°C was also described for the grain boundaries in doped SrTiO<sub>3</sub> polycrystals in Ref. [150]. Moreover the activation energies match reasonably well to the results of conductivities in the space charges at grain boundaries in Refs. [150] and [78]. This already suggests that charge transport in the nominally undoped SrTiO<sub>3</sub> single crystals might contribute to the observed behaviour. A true increase of ionic conductivity in YSZ, as proposed in a similar experiment in Ref. [77], will indeed be refuted in the next chapter by tracer diffusion experiments.

In Fig. 7.8(c), the grain and grain boundary conductivities of the YSZ films on sapphire are plotted. The bulk conductivities and the activation energies of the thicker layers Sap-PLD 2 ( $E_a = 0.9$  eV) and Sap-SG 2 ( $E_a = 1.0$  eV) agree very well with each other and also with the macroscopic references. The thin layer Sap-PLD 1 (28 nm) has a lower bulk conductivity, which might be caused by a lower degree of crystallinity, cf. Fig. 7.4(a). The activation energy of 1.0 eV, however, is again close to that of the macroscopic references. On the thin layer Sap-SG 1, a small bulk conductivity at low temperatures

combined with a high activation energy of 1.2 eV was measured. In a detailed related study, this deviation was attributed to lattice strain in the large epitaxial grains, see Ref. [19]. The grain boundary conductivities of all different layers are similar, with the values for Sap-PLD 2 being somewhat higher than the others. The grain boundary activation energies are all between 1.1 eV and 1.2 eV, see Table 7.1

Using the NERNST-EINSTEIN relation (e.g. [39, 112])

$$\frac{D^\sigma}{k_B \cdot T} = \frac{\sigma}{4 \cdot n_O \cdot e^2} \quad (7.4)$$

the conductivity related diffusion coefficients  $D^\sigma$  at 500°C were calculated from the total conductivity  $\sigma$  of the layers and these values are given in Table 7.2. In eq. 7.4,  $k_B$  denotes the BOLTZMANN constant and  $T$  is the absolute temperature;  $n_O$  refers to the concentration of the oxygen sites and  $e$  to the elementary charge. In the following, these diffusion coefficients will be compared to those obtained from the complementary tracer diffusion experiments.

### 7.3.3 Tracer diffusion experiments

In Fig. 7.9, lateral  $^{18}\text{O}$  concentration profiles in Sap-PLD 1 and Sap-SG 1 measured by TOF-SIMS after the incorporation step and after the diffusion step are shown as an example. The profiles were accumulated along the x-axis of the displayed isotope distribution image and baseline corrected to account for the background concentration and a slight signal drift, see chapter 2.6.2. The integrated region along the z-axis, cf. Fig. 7.2, was chosen such that all signals could for sure be related to the YSZ layer. They did not include the topmost surface and bottommost interface regions of YSZ to avoid SIMS artefacts. A significant concentration variation in z-direction (see Fig. 7.2) was not observed, neither before nor after the actual diffusion step. It should be emphasized that any fast diffusion in interfacial regions would still be visible as high effective diffusion coefficients. This is due to the thinness and the correspondingly short across-plane

Table 7.2: Estimated surface exchange coefficients at 300°C and diffusion coefficients measured at 500°C of the layers used in this study. Diffusion problem “step” denotes an experiment with an incorporation of the tracer in half of the sample, cf. left column in Fig. 7.9 and Fig. 7.2(a). “Box” corresponds to an incorporation step as in the right column of Fig. 7.9 and Fig. 7.2(b). Conductivity based diffusion coefficients  $D^\sigma$  are compared to tracer diffusion coefficients  $D^*$  of uncovered (“free”) and Pt covered YSZ. The tracer diffusion coefficient listed in the last row was measured in a YSZ single crystal by depth profiling, see Ref. [148].

Sample	$k^*$ at 300°C [cm/s]	Diffusion problem	Diffusion time [s]	$D^\sigma$ [cm <sup>2</sup> /s]	$D^*_{\text{YSZ, free}}$ [cm <sup>2</sup> /s]	$H_R^{\text{YSZ, free}}$ [-]	$D^*_{\text{YSZ, Pt}}$ [cm <sup>2</sup> /s]	$H_R^{\text{YSZ, Pt}}$ [-]
MgO-PLD	6·10 <sup>-11</sup>	Box	1800	9.3·10 <sup>-11</sup>	6.2·10 <sup>-11</sup>	0.67	6.6·10 <sup>-11</sup>	0.71
MgO-SG	1·10 <sup>-11</sup>	-	-	6.7·10 <sup>-11</sup>	-	-	-	-
Sap-PLD 1	3·10 <sup>-11</sup>	Step	5400	5.5·10 <sup>-11</sup>	1.1·10 <sup>-10</sup>	2	1.1·10 <sup>-10</sup>	2
Sap-PLD 2	8·10 <sup>-10</sup>	Box	1800	1.8·10 <sup>-10</sup>	1.5·10 <sup>-10</sup>	0.83	9.8·10 <sup>-11</sup>	0.54
Sap-SG 1	9·10 <sup>-11</sup>	Box	2500	2.2·10 <sup>-10</sup>	2.7·10 <sup>-10</sup>	1.2	2.4·10 <sup>-10</sup>	1.1
Sap-SG 2	8·10 <sup>-11</sup>	Step	5400	4.5·10 <sup>-10</sup>	6.2·10 <sup>-10</sup>	1.4	3.6·10 <sup>-10</sup>	0.8
STO-PLD	3·10 <sup>-10</sup>	Box	1800	1.8·10 <sup>-9</sup>	1.6·10 <sup>-10</sup>	0.089	1.8·10 <sup>-10</sup>	0.1
STO-SG	6·10 <sup>-11</sup>	Step	5400	9.7·10 <sup>-9</sup>	1.1·10 <sup>-10</sup>	0.011	1.0·10 <sup>-10</sup>	0.01
Ref. [148]	1·10 <sup>-9</sup>	-	-	Single crystal:	3.2·10 <sup>-10</sup>	-	-	-

diffusion times in the YSZ films. In Fig. 7.9(a) and (b) the profiles after thermal exchange for 30 minutes at 300°C are plotted (incorporation step). In the case of Sap-PLD 1, half of the surface was covered by the Cr/Au protection layer, while for Sap-SG only a narrow stripe was uncovered and thus exposed to  $^{18}\text{O}_2$ , cf. Fig. 7.2(a) and (b). As predicted above, a significant enrichment of tracer ions was achieved in this first step. The maximum concentration of the semi-infinite step in Sap-PLD is about 5%, while the height of the finite box of Sap-SG 1 amounts to ca. 8%.

Using this maximum concentration  $c_0$  and assuming a constant increase of concentration over the whole thickness of the layer  $H$  during the exchange time  $t_{ex}$ , surface exchange coefficients were estimated by

$$k^* = \frac{(c_0 - c_{bg}) \cdot H}{c_{gas} \cdot t_{ex}} \quad (7.5)$$

and are given in Table 7.2. Eq. 7.5 results from the continuity equation and the assumption of a time independent driving force for tracer incorporation. These assumptions are reasonable as the maximum tracer concentrations in YSZ are below 10% and the layers are very thin, cf. Theoretical Considerations. Both maximum concentrations are significantly lower than the level of 20% calculated using the results of Ref. [148], see Fig. 7.1. Hence, the surface exchange coefficient is accordingly smaller in the present case. In both profiles, but particularly in Fig. 7.9(b), concentration spikes are found outside the uncovered YSZ part. These can be linked to pinholes in the barrier layer and are visible as spots of increased concentration in the ion images. This underlines the need for a reliable dense barrier in successful experiments. The diffusion profiles in Fig. 7.9(c) to (f) were recorded on different positions of the layers with less defects.

Fig. 7.9(c) and (d) show the diffusion profiles recorded on parts of the YSZ film not having been covered by Pt during the actual diffusion experiment. Both profiles can excellently be fit to eqs. 7.2 or 7.3 respectively. It should be noted that in the case of

## 7 Tracer diffusion studies in thin film YSZ

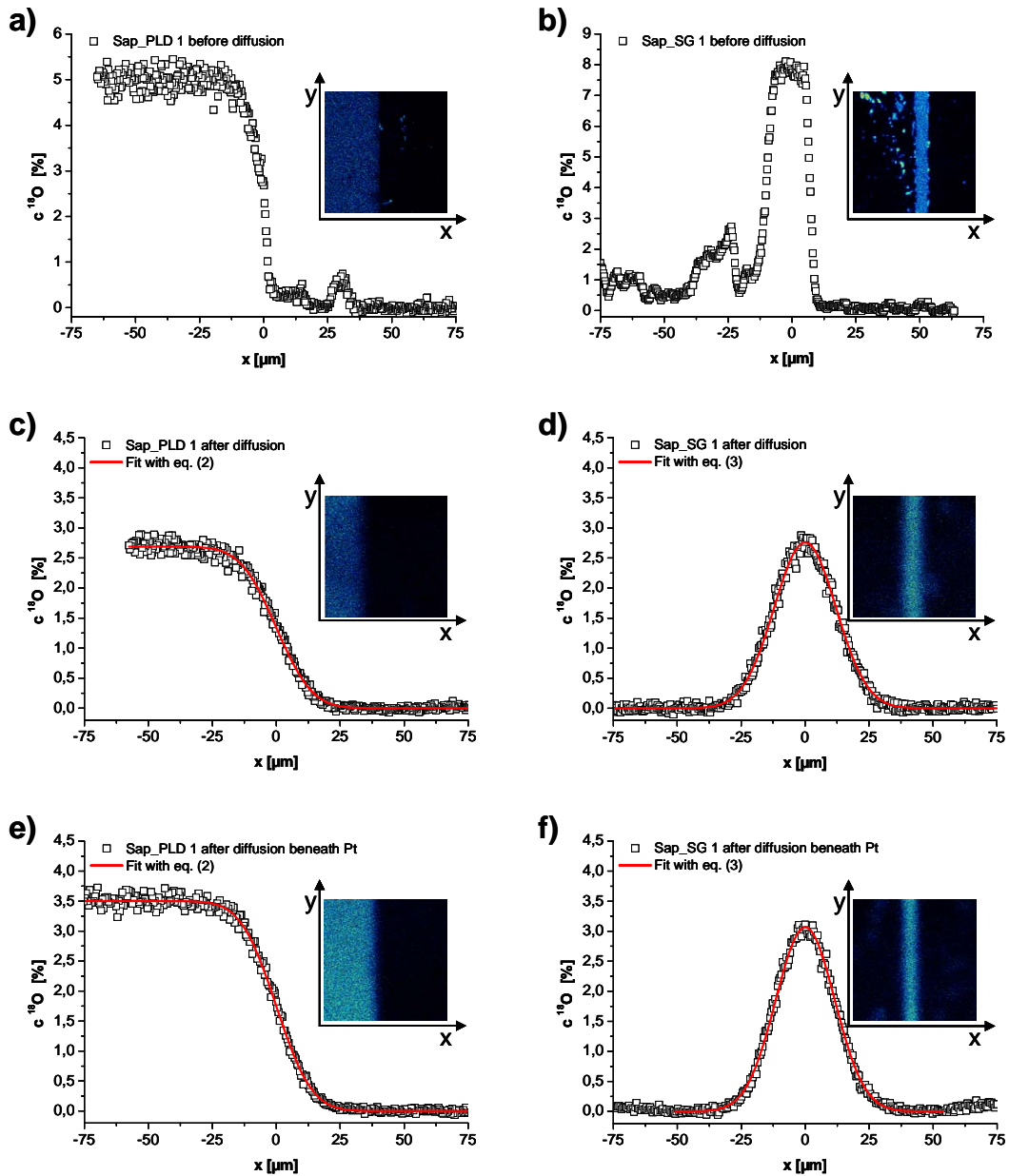


Figure 7.9: Lateral  $^{18}\text{O}$  concentration profiles of Sap-PLD 1 and Sap-SG 1, see Table 7.1 for more information on the layers. The Cr/Au gas diffusion barrier was removed before measurement of each profile. In (a) and (b) profiles are shown after the incorporation step, ie. after a thermal gas exchange at  $300^\circ\text{C}$  in 97%  $^{18}\text{O}_2$ . Graphs (c) to (f) display the diffusion profiles after diffusion at  $500^\circ\text{C}$  in ultra high vacuum. Diffusion times were 5400 s for Sap-PLD 1 (c) and (e)) and 2500 s for Sap-SG 1 (d) and (f). In (c) and (d) the diffusion profiles in YSZ with a free surface (vacuum-exposed) are plotted, while the profiles in (d) and (f) developed in YSZ under a Pt layer.

Sap-PLD 1 the height of the concentration step has decreased by about 2.5% compared to the profile before the diffusion. A comparison of the  $c_0$  parameter in eq. 7.3 obtained from fitting with the originally measured “box height” shows that this was not the case for Sap-SG 1.

Fig. 9e) and (f) display the diffusion profiles resulting in YSZ beneath the platinum film. Again a good fit to eqs. 7.2 or 7.3 was possible. However, again a decrease of the original concentration step in Sap-PLD 1 is observed, this time by 1.5%, while the  $c_0$  parameter of the  $^{18}\text{O}$  box in the platinum covered part of Sap-SG 1 corresponds to the measured starting height. It seems unlikely that this decrease in concentration took place during the UHV diffusion step at 500°C, since then an effect should also have been visible for Sap-SG 1. In comparison, the diffusion time of Sap-SG 1 is shorter by a factor of 2, but the surface exchange coefficient is three times larger than in Sap-PLD 1. Therefore, most likely, undeliberate and still unknown differences in the treatment of the layers caused the concentration drop. The resulting diffusion coefficients are thus regarded to be equally reliable.

In the same manner, all diffusion profiles were analysed. Unfortunately MgO-SG detached from the substrate and no measurement was possible there. In Table 7.2, the resulting tracer diffusion coefficients and estimated surface exchange coefficients are given for each layer. In previous studies [17, 151], it has been reported or suggested that ion transport on the YSZ surface is faster compared to the bulk. A significant difference in surface and film bulk diffusion coefficients should lead to different effective diffusion coefficients in YSZ beneath Pt and YSZ exposed to vacuum. A slightly faster diffusion of YSZ exposed to vacuum was indeed found for Sap-SG 2 and Sap-PLD 2. However, if this difference in the effective diffusion coefficients was due to a surface effect, it should have been much more pronounced in the thinner layers Sap-SG 1 and Sap-PLD 1, which is not the case. For all other investigated YSZ films both, tracer diffusion coefficients

with and without Pt agree excellently. Hence, a systematic enhancement of the free surface diffusion coefficient was not confirmed in our study.

Finally, one can compare the measured tracer diffusion coefficients to the conductivity based ones. These values are correlated by the HAVEN ratio [39, 112]

$$H_R = \frac{D^*}{D^\sigma} \quad (7.6)$$

In many cases, this ratio is assumed to be given by the crystal structure dependent correlation factor [39] and thus by 0.65 for cubic YSZ [112]. The values obtained in this study are summarized in Table 7.2. Since diffusion and conductivity experiments were conducted on different heating stages, slight temperature differences cannot be excluded. Hence, we regard  $H_R$  values between ca. 0.5 and 2 as indication for good agreement between ion transport data obtained from the two complementary experimental methods.

However, comparison of conductivity and tracer diffusion coefficients in the case of the YSZ films on strontium titanate reveals very pronounced differences and  $H_R$  values much smaller than 0.65. While the tracer diffusion coefficients are close to the values measured on sapphire, the conductivity based diffusion coefficients at 500°C are one or, in the case of STO-SG, even two orders of magnitude higher. Tracer diffusion only monitors ion transport in YSZ, while the resistances measured by impedance spectroscopy also include current via the STO substrate. Relevant levels of ion transport in strontium titanate were not detected in the tracer experiments. Hence, we conclude that electronic current in the STO substrates dominates the total current in impedance studies and pretends a high ionic conductivity in the YSZ films. Rather, the oxygen ion conductivity in the YSZ layers on strontium titanate remained similar to that on the other substrates. This supports earlier investigations [34] suggesting that the conductivity enhancements in YSZ|STO hetero-layers were not caused by an increased ionic conductivity.

## 7.4 Conclusions

Finite element calculations using previously published surface exchange and diffusion coefficients of YSZ suggest that a significant enrichment of an  $^{18}\text{O}$  tracer can be achieved in thin YSZ layers by entropy driven tracer exchange at temperatures as low as  $300^\circ\text{C}$ . Hence, two step tracer diffusion experiments become feasible: In an incorporation step, diffusion barrier layers covering parts of the films are used to obtain regions with high tracer concentration in the YSZ layer. Sharp steps between regions with and without tracer enrichment then allow lateral diffusion experiments in ultra high vacuum and can considerably alleviate problems of diffusion measurements in thin layers.

In combination with impedance measurements this method was employed to analyse mass and charge transport in YSZ thin films on sapphire, magnesia and strontium titanate single crystals prepared by means of pulsed laser deposition and a sol-gel route. XRD analysis revealed pronounced compressive and dilative changes of the lattice constant in the different layers. However, impedance spectroscopic measurements showed that in layers on sapphire and magnesia grain conductivities in the temperature range under consideration are not enhanced compared to known YSZ bulk conductivities i.e. are either unaffected by the substrate, or are even reduced. Grain boundaries turned out to be blocking. Only YSZ films on strontium titanate, revealed very high effective conductivities.

The complementary  $^{18}\text{O}$  tracer diffusion study on the same films supports the results obtained by impedance spectroscopy for the YSZ layers on sapphire and magnesia. Enhanced conductivities compared to bulk YSZ are not found. Diffusion coefficients of the YSZ layers on strontium titanate agree very well with the results on the other substrates. This conclusively proves that the high conductivity values found for YSZ on strontium titanate are due to, most likely, electronic conduction in the substrate, while no fast ion conduction path is present.

## Summary of the scientific achievements

Thin films of yttria stabilized zirconia (YSZ) of different thickness were prepared on three different single crystalline substrates, namely alumina, magnesia and strontium titanate. With pulsed laser deposition (PLD) and a sol-gel route using spin coating and subsequent high temperature annealing, two different preparation methods were used to synthesize the layers.

The layer thickness was measured by digital holographic microscopy (DHM) of sputter craters. To ensure that these craters exactly reached down to the YSZ|substrate interface, their preparation was controlled by time of flight secondary ion mass spectrometry (TOF-SIMS). The range of thickness for the PLD synthesized samples was between 30 and 250 nm and between 30 and 170 nm for the sol-gel prepared ones.

X-ray diffraction (XRD) patterns were recorded on each layer and revealed pronounced texturing in all PLD grown layers and also in the thinner of the sol-gel prepared ones. The thicker sol-gel films on alumina turned out to consist of several sub-layers with a different degree and direction of texture beginning with a highly textured region near the interface. Crystallographic strain was also found in numerous sol-gel and PLD prepared layers, however, exact quantification was out of scope of this work.

The top view images provided by measurements with atomic force microscopy (AFM)

allowed to quantify the lateral grain size of the YSZ layers investigated in this study. As prepared PLD grown thin films usually exhibited a small grain size of a few tens of nanometers. YSZ films prepared by the sol-gel route had a comparatively large lateral grain size of about 200 to 400 nm, which is considerably larger than the typical film thickness of around 100 nm. In combination with the XRD studies it was possible to link different grain morphologies to their crystallographic orientation.

Electrical impedance spectroscopy of the YSZ layers on the different substrates was a major part of the present thesis. In a detailed study on PLD prepared YSZ films on alumina substrates, it was shown that separation of grain bulk and grain boundary impedance can be achieved, even on very thin YSZ layers. Such measurements on thin films were not reported before and were made possible by using a special geometry of long, thin and closely spaced metal electrodes arranged interdigitally. By variation of geometrical parameters of the electrodes and the thin films, it could be shown that all parameters in a modified VOIGT equivalent circuit showed the expected changes. Thus it was concluded that the interpretation in terms of separated grain bulk and grain boundary impedances was correct.

The absolute values of grain bulk conductivity in PLD and sol-gel prepared layers on alumina agreed very well with the conductivities measured on macroscopic YSZ polycrystals. This also clearly proved the often discussed hypothesis that grain boundaries are the origin of the low lateral film conductivities reported in many studies.

The conductivities of the grain boundaries in the YSZ thin films on alumina were also in the range of those reported for macroscopic reference samples. However, the values measured in PLD grown films were higher than in the sol-gel prepared samples. This can be explained by the fewer grain boundaries in the sol-gel synthesized samples, due to the larger grain sizes, and therefore a higher impurity concentration in the grain boundaries. The crystallographic strain was, in one case, the reason for an elevated activation energy

## 8 Summary of the scientific achievements

of the grain bulk conductivity. All grain boundaries were found to be an impediment to oxygen ion transport.

In order to investigate possible effects of different YSZ|substrate interfaces and of the YSZ surface on lateral oxygen ion transport, an  $^{18}\text{O}$  tracer diffusion study was conducted. In this context, a novel method was introduced to perform tracer diffusion studies in thin films. In a first step, the tracer was incorporated in a well defined so called “starting” profile, which would, in a second annealing step, be broadened to a lateral diffusion profile. This second step was carried out at higher temperatures than the incorporation step and in ultra high vacuum to exclude tracer loss. The prerequisites for a usable starting profile are a high tracer concentration and a sharp concentration drop at its edges. This would allow well defined boundary conditions for the analytical evaluation of the diffusion profile measured in the second step by TOF-SIMS.

A well defined starting profile could be prepared by using current driven incorporation from an  $^{18}\text{O}_2$  atmosphere and mixed conducting electrodes with sharp edges. The resulting profile allowed first measurements of lateral tracer diffusion coefficients in a thin PLD prepared YSZ layer. However, reproduction of this incorporation step proved to be very difficult. Nevertheless, those experiments paved the way to developing a much easier entropy driven gas exchange step. In this new two-step process only parts of the surface of the YSZ layers were exposed to the tracer gas atmosphere, while the rest was covered by a well defined gas tight metal barrier. The barrier was removed afterwards and the surface of the YSZ film could be further modified.

The resulting tracer diffusion coefficients showed no significant difference, whether they were recorded under a free YSZ surface, or a platinum covered one. Hence, any promoting effect of the YSZ surface on ion transport could not be verified.

Finally, a comparison of tracer diffusion and conductivity measurements was done. For YSZ layers on alumina and magnesia the results for both experiments agree very well. Only, the conductivity for the YSZ films prepared on strontium titanate showed

## 8 *Summary of the scientific achievements*

surprisingly high values and no separation of grain and grain boundaries was possible, despite using interdigital electrodes. However, the tracer diffusion coefficients were very close to the values measured on the other substrates. Therefore, it can be concluded that the high conductivity was due to electronic conductivity in the strontium titanate substrate. Accordingly, an interface effect enhancing the ionic conductivity could also not be identified in the YSZ|SrTiO<sub>3</sub> system.

# Bibliography

- [1] N. Sata, K. Eberman, K. Eberl, and J. Maier. Mesoscopic fast ion conduction in nanometre-scale planar heterostructures. *Nature*, 408(6815):946–949, 2000.
- [2] H. B. Wang, C. R. Xia, G. Y. Meng, and D. K. Peng. Deposition and characterization of YSZ thin films by aerosol-assisted CVD. *Materials Letters*, 44(1):23–28, 2000.
- [3] A. Cheikh, A. Madani, A. Touati, H. Boussetta, and C. Monty. Ionic conductivity of zirconia based ceramics from single crystals to nanostructured polycrystals. *Journal of the European Ceramic Society*, 21(10-11):1837–1841, 2001.
- [4] S. Y. Chun and N. Mizutani. The transport mechanism of YSZ thin films prepared by MOCVD. *Applied Surface Science*, 171(1-2):82–88, 2001.
- [5] T. Suzuki, I. Kosacki, H. U. Anderson, and P. Colomban. Electrical conductivity and lattice defects in nanocrystalline cerium oxide thin films. *Journal of the American Ceramic Society*, 84(9):2007–2014, 2001.
- [6] T. Suzuki, I. Kosacki, and H. U. Anderson. Microstructure-electrical conductivity relationships in nanocrystalline ceria thin films. *Solid State Ionics*, 151(1-4):111–121, 2002.

- [7] L. Chen, C. L. Chen, X. Chen, W. Donner, S. W. Liu, Y. Lin, D. X. Huang, and A. J. Jacobson. Electrical properties of a highly oriented, textured thin film of the ionic conductor Gd : CeO<sub>2</sub>-delta on (001) MgO. *Applied Physics Letters*, 83(23):4737–4739, 2003.
- [8] G. Chiodelli, L. Malavasi, V. Massarotti, P. Mustarelli, and E. Quartarone. Synthesis and characterization of Ce<sub>0.8</sub>Gd<sub>0.2</sub>O<sub>2-y</sub> polycrystalline and thin film materials. *Solid State Ionics*, 176(17-18):1505–1512, 2005.
- [9] J. W. Fergus. Electrolytes for solid oxide fuel cells. *Journal of Power Sources*, 162(1):30–40, 2006.
- [10] K. Gmucova, M. Hartmanova, and F. Kundracik. Charge distribution at interface and in bulk of YSZ thin films deposited on Si substrate. *Ceramics International*, 32(2):105–109, 2006.
- [11] J. H. Joo and G. M. Choi. Electrical conductivity of scandia-stabilized zirconia thin film. *Solid State Ionics*, 179(21-26):1209–1213, 2008.
- [12] J. H. Joo and G. M. Choi. Electrical conductivity of thin film ceria grown by pulsed laser deposition. *Journal of the European Ceramic Society*, 27(13-15):4273–4277, 2007.
- [13] J. H. Joo and G. M. Choi. Electrical conductivity of YSZ film grown by pulsed laser deposition. *Solid State Ionics*, 177(11-12):1053–1057, 2006.
- [14] I. Kosacki, C. M. Rouleau, P. F. Becher, J. Bentley, and D. H. Lowndes. Nanoscale effects on the ionic conductivity in highly textured YSZ thin films. *Solid State Ionics*, 176(13-14):1319–1326, 2005.
- [15] A. Peters, C. Korte, D. Hesse, N. Zakharov, and J. Janek. Ionic conductivity and activation energy for oxygen ion transport in superlattices - The multilayer system CSZ (ZrO<sub>2</sub>+CaO)/Al<sub>2</sub>O<sub>3</sub>. *Solid State Ionics*, 178(1-2):67–76, 2007.

- [16] C. Peters, A. Weber, B. Butz, D. Gerthsen, and E. Ivers-Tiffée. Grain-Size Effects in YSZ Thin-Film Electrolytes. *Journal of the American Ceramic Society*, 92(9):2017–2024, 2009.
- [17] M. Gerstl, T. Froemling, A. Schintlmeister, H. Hutter, and J. Fleig. Measurement of  $^{18}\text{O}$  tracer diffusion coefficients in thin yttria stabilized zirconia films. *Solid State Ionics*, 184:23–26, 2011.
- [18] M. Gerstl, E. Navickas, G. Friedbacher, F. Kubel, M. Ahrens, and J. Fleig. The separation of grain and grain boundary impedance in thin yttria stabilized zirconia (YSZ) layers. *Solid State Ionics*, 185:32–41, 2011.
- [19] M. Gerstl, E. Navickas, M. Leitgeb, G. Friedbacher, F. Kubel, and J. Fleig. The grain and grain boundary impedance of sol-gel prepared thin layers of yttria stabilized zirconia (YSZ). *Solid State Ionics*, page submitted, 2011.
- [20] X. D. He, B. Meng, Y. Sun, B. C. Liu, and M. W. Li. Electron beam physical vapor deposition of YSZ electrolyte coatings for SOFCs. *Applied Surface Science*, 254(22):7159–7164, 2008.
- [21] S. Heiroth, T. Lippert, A. Wokaun, and M. Dobeli. Microstructure and electrical conductivity of YSZ thin films prepared by pulsed laser deposition. *Applied Physics a-Materials Science & Processing*, 93(3):639–643, 2008.
- [22] S. Heiroth, T. Lippert, A. Wokaun, M. Dobeli, J. L. M. Rupp, B. Scherrer, and L. J. Gauckler. Yttria-stabilized zirconia thin films by pulsed laser deposition: Microstructural and compositional control. *Journal of the European Ceramic Society*, 30(2):489–495, 2010.
- [23] A. Infortuna, A. S. Harvey, and L. J. Gauckler. Microstructures of CGO and YSZ thin films by pulsed laser deposition. *Advanced Functional Materials*, 18(1):127–135, 2008.

- [24] C. Korte, A. Peters, J. Janek, D. Hesse, and N. Zakharov. Ionic conductivity and activation energy for oxygen ion transport in superlattices - the semicoherent multilayer system YSZ ( $\text{ZrO}_2+9.5 \text{ molY}_2\text{O}_3$ )/ $\text{Y}_2\text{O}_3$ . *Physical Chemistry Chemical Physics*, 10(31):4623–4635, 2008.
- [25] A. Kushima and B. Yildiz. Oxygen ion diffusivity in strained yttria stabilized zirconia: Where is the fastest strain? *Journal of Materials Chemistry*, 20(23):4809–4819, 2010.
- [26] U. P. Muecke, D. Beckel, A. Bernard, A. Bieberle-Hutter, S. Graf, A. Infortuna, P. Muller, J. L. M. Rupp, J. Schneider, and L. J. Gauckler. Micro Solid Oxide Fuel Cells on Glass Ceramic Substrates. *Advanced Functional Materials*, 18(20):3158–3168, 2008.
- [27] N. Pryds, J. Schou, and S. Linderoth. Large-area production of yttria-stabilized zirconia by pulsed laser deposition. *COLA'05: 8th International Conference on Laser Ablation*, 59:140–143 777, 2007.
- [28] N. Pryds, B. Toftmann, J. B. Bilde-Sorensen, J. Schou, and S. Linderoth. Thickness determination of large-area films of yttria-stabilized zirconia produced by pulsed laser deposition. *Applied Surface Science*, 252(13):4882–4885, 2006.
- [29] N. Schichtel, C. Korte, D. Hesse, and J. Janek. Elastic strain at interfaces and its influence on ionic conductivity in nanoscaled solid electrolyte thin films-theoretical considerations and experimental studies. *Physical Chemistry Chemical Physics*, 11(17):3043–3048, 2009.
- [30] N. Schichtel, C. Korte, D. Hesse, N. Zakharov, B. Butz, D. Gerthsen, and J. Janek. On the influence of strain on ion transport: microstructure and ionic conductivity of nanoscale YSZ vertical bar  $\text{Sc}_2\text{O}_3$  multilayers. *Physical Chemistry Chemical Physics*, 12(43):14596–14608, 2010.

- [31] M. Sillassen, P. Eklund, M. Sridharan, N. Pryds, N. Bonanos, and J. Bottiger. Ionic conductivity and thermal stability of magnetron-sputtered nanocrystalline yttria-stabilized zirconia. *Journal of Applied Physics*, 105(10):–, 2009.
- [32] T. Lippert, S. Heiroth, R. Frison, J. L. M. Rupp, E. J. B. Meier, E. M. Gubler, M. Dobeli, K. Conder, A. Wokaun, and L. J. Gauckler. Crystallization and grain growth characteristics of yttria-stabilized zirconia thin films grown by pulsed laser deposition. *Solid State Ionics*, 191(1):12–23, 2011.
- [33] J. S. Park, Y. B. Kim, J. H. Shim, S. Kang, T. M. Gur, and F. B. Prinz. Evidence of Proton Transport in Atomic Layer Deposited Yttria-Stabilized Zirconia Films. *Chemistry of Materials*, 22(18):5366–5370, 2010.
- [34] A. Cavallaro, M. Burriel, J. Roqueta, A. Apostolidis, A. Bernardi, A. Tarancón, R. Srinivasan, S. N. Cook, H. L. Fraser, J. A. Kilner, D. W. McComb, and J. Santiso. Electronic nature of the enhanced conductivity in YSZ-STO multilayers deposited by PLD. *Solid State Ionics*, 181(13-14):592–601, 2010.
- [35] Q. L. Xiao, H. B. He, S. Y. Shao, J. Shao, and Z. X. Fan. Influences of deposition rate and oxygen partial pressure on residual stress and microstructure of YSZ thin films. *Thin Solid Films*, 517(15):4295–4298, 2009.
- [36] L. Wang, R. Merkle, J. Maier, T. Acarturk, and U. Starke. Oxygen tracer diffusion in dense Ba<sub>0.5</sub>Sr<sub>0.5</sub>Co<sub>0.8</sub>Fe<sub>0.2</sub>O<sub>3-δ</sub> films. *Applied Physics Letters*, 94(7):–, 2009.
- [37] H. L. Tuller, S. J. Litzelman, and W. Jung. Micro-ionics: next generation power sources. *Physical Chemistry Chemical Physics*, 11(17):3023–3034, 2009.
- [38] W. Jung, J. L. Hertz, and H. L. Tuller. Enhanced ionic conductivity and phase meta-stability of nano-sized thin film yttria-doped zirconia (YDZ). *Acta Materialia*, 57(5):1399–1404, 2009.

- [39] J. Maier. *Physical Chemistry of Ionic Materials*. John Wiley & Sons Ltd, 2004.
- [40] Igor Kosacki, Toshio Suzuki, Vladimir Petrovsky, and Harlan U. Anderson. Electrical conductivity of nanocrystalline ceria and zirconia thin films. *Solid State Ionics*, 136-137:1225–1233, 2000.
- [41] I. Kosacki and H. U. Anderson. Mixed conductivity in nanocrystalline oxide thin films. *Ionic and Mixed Conducting Ceramics Iv*, 2001(28):238–251 428, 2002.
- [42] I. Kosacki, H. U. Anderson, Y. Mizutani, and K. Ukai. Nonstoichiometry and electrical transport in Sc-doped zirconia. *Solid State Ionics*, 152:431–438, 2002.
- [43] I. Kosacki. Nanoscaled oxide thin films for energy conversion. *Fuel Cell Technologies: State and Perspectives*, 202:395–416 429, 2005.
- [44] H. Kahlert, F. Frey, H. Boysen, and K. Lassak. Defect structure and diffuse scattering of zirconia single crystals at elevated temperatures and simultaneously applied electric field. *Journal of Applied Crystallography*, 28:812–819, 1995.
- [45] S. Heiroth, J. Koch, T. Lippert, A. Wokaun, D. Gunther, F. Garrelie, and M. Guillermin. Laser ablation characteristics of yttria-doped zirconia in the nanosecond and femtosecond regimes. *Journal of Applied Physics*, 107(1):–, 2010.
- [46] J. Lappalainen, H. L. Tuller, and V. Lantto. Electronic conductivity and dielectric properties of nanocrystalline CeO<sub>2</sub> films. *Journal of Electroceramics*, 13(1-3):129–133, 2004.
- [47] R. Bachelet, A. Boule, B. Soulestin, F. Rossignol, R. Guinebretiere, and A. Dager. Two-dimensional versus three-dimensional post-deposition grain growth in epitaxial oxide thin films: Influence of the substrate surface roughness. *Thin Solid Films*, 515(18):7080–7085, 2007.

- [48] B. Butz, H. Stormer, D. Gerthsen, M. Bockmeyer, R. Kruger, E. Ivers-Tiffée, and M. Luysberg. Microstructure of nanocrystalline yttria-doped zirconia thin films obtained by sol-gel processing. *Journal of the American Ceramic Society*, 91(7):2281–2289, 2008.
- [49] R. Guinebretiere, B. Soulestin, and A. Dauger. XRD and TEM study of heteroepitaxial growth of zirconia on magnesia single crystal. *Thin Solid Films*, 319(1-2):197–201, 1998.
- [50] S. G. Kim, S. W. Nam, S. P. Yoon, S. H. Hyun, J. Han, T. H. Lim, and S. A. Hong. Sol-gel processing of yttria-stabilized zirconia films derived from the zirconium n-butoxide-acetic acid-nitric acid-water-isopropanol system. *Journal of Materials Science*, 39(8):2683–2688, 2004.
- [51] Shunyan Tao, Bo Liang, Jianhua Yu, and Yun. Liu. Thermal barrier coating materials. In *Surf. Modif. Mater. Coat. Films*, pages 277–302. Research Signpost, 2009.
- [52] W. Ma and H. Dong. Ceramic thermal barrier coating materials. In *Therm. Barrier Coat.*, pages 25–52. Woodhead Publishing Ltd., 2011.
- [53] R. T. Wu. Substrate and bond coat related failure of thermal barrier coatings. In *Therm. Barrier Coat.*, pages 263–293. Woodhead Publishing Ltd., 2011.
- [54] H. Guo, R. Yao, and L. Zhou. Plasma-sprayed thermal barrier coatings with segmentation cracks. In *Therm. Barrier Coat.*, pages 161–174. Woodhead Publishing Ltd., 2011.
- [55] J. Chevalier and L. Gremillard. Zirconia ceramics. In *Bioceram. Their Clin. Appl.*, pages 243–265. Woodhead Publishing Ltd., 2008.
- [56] Michael Hisbergues, Sophie Vendeville, and Philippe Vendeville. Zirconia: established facts and perspectives for a biomaterial in dental implantology. *Journal*

- of Biomedical Materials Research, Part B: Applied Biomaterials*, 88B(2):519–529, 2009.
- [57] Vanni Lughì and Valter. Sergio. Low temperature degradation aging of zirconia: A critical review of the relevant aspects in dentistry. *Dental Materials*, 26(8):807–820, 2010.
- [58] Fernando Zarone, Simona Russo, and Roberto. Sorrentino. From porcelain-fused-to-metal to zirconia: Clinical and experimental considerations. *Dental Materials*, 27(1):83–96, 2011.
- [59] R. Moos. A brief overview on automotive exhaust gas sensors based on electroceramics. *International Journal of Applied Ceramic Technology*, 2(5):401–413, 2005.
- [60] S. B. Adler. Factors governing oxygen reduction in solid oxide fuel cell cathodes. *Chemical Reviews*, 104(10):4791–4843, 2004.
- [61] Frank Stephan Baumann. *Oxygen reduction kinetics on mixed conducting SOFC model cathodes*. PhD thesis, Max Planck Institut, 2006.
- [62] F. S. Baumann, J. Fleig, H. U. Habermeier, and J. Maier. Impedance spectroscopic study on well-defined (La,Sr)(Co,Fe)O<sub>3-δ</sub> model electrodes. *Solid State Ionics*, 177(11-12):1071–1081, 2006.
- [63] D. Beckel, A. Bieberle-Huetter, A. Harvey, A. Infortuna, U. P. Muecke, M. Prestat, J. L. M. Rupp, and L. J. Gauckler. Thin films for micro solid oxide fuel cells. *Journal of Power Sources*, 173(1):325–345, 2007.
- [64] J. Fleig and J. Maier. The influence of inhomogeneous potential distributions on the electrolyte resistance in solid oxide fuel cells. *Proceedings of the Fifth International Symposium on Solid Oxide Fuel Cells (Sofc-V)*, 97(40):1374–1383 1398, 1997.

- [65] Shiqiang Hui, Justin Roller, Sing Yick, Xinge Zhang, Cyrille Deces-Petit, Yongsong Xie, Radenka Maric, and Dave Ghosh. A brief review of the ionic conductivity enhancement for selected oxide electrolytes. *Journal of Power Sources*, 172(2):493–502, 2007.
- [66] J. Januschewsky, M. Ahrens, A. Opitz, F. Kubel, and J. Fleig. Optimized  $\text{La}_{0.6}\text{Sr}_{0.4}\text{CoO}_3$ -delta Thin-Film Electrodes with Extremely Fast Oxygen-Reduction Kinetics. *Advanced Functional Materials*, 19(19):3151–3156, 2009.
- [67] D. E. Vladikova, Z. B. Stoyanov, A. Barbucci, M. Viviani, P. Carpanese, J. A. Kilner, S. J. Skinner, and R. Rudkin. Impedance studies of cathode/electrolyte behaviour in SOFC. *Electrochim. Acta*, 53(25):7491–7499, 2008.
- [68] J. Will, A. Mitterdorfer, C. Kleinlogel, D. Perednis, and L. J. Gauckler. Fabrication of thin electrolytes for second-generation solid oxide fuel cells. *Solid State Ionics*, 131(1-2):79–96, 2000.
- [69] S. P. S. Badwal and K. Foger. Solid oxide electrolyte fuel cell review. *Ceramics International*, 22(3):257–265, 1996.
- [70] U. Brossmann, G. Knoner, H. E. Schaefer, and R. Wurschum. Oxygen diffusion in nanocrystalline  $\text{ZrO}_2$ . *Reviews on Advanced Materials Science*, 6(1):7–11, 2004.
- [71] G. Knoner, K. Reimann, R. Rower, U. Sodervall, and H. E. Schaefer. Enhanced oxygen diffusivity in interfaces of nanocrystalline  $\text{ZrO}_2$  center dot  $\text{Y}_2\text{O}_3$ . *Proceedings of the National Academy of Sciences of the United States of America*, 100(7):3870–3873, 2003.
- [72] M. J. Verkerk, B. J. Middelhuis, and A. J. Burggraaf. Effect of Grain-Boundaries on the Conductivity of High-Purity  $\text{ZrO}_2$ - $\text{Y}_2\text{O}_3$  Ceramics. *Solid State Ionics*, 6(2):159–170, 1982.

- [73] X. Guo and Z. L. Zhang. Grain size dependent grain boundary defect structure: case of doped zirconia. *Acta Materialia*, 51(9):2539–2547, 2003.
- [74] X. J. Ning, C. X. Li, C. J. Li, and G. J. Yang. Modification of microstructure and electrical conductivity of plasma-sprayed YSZ deposit through post-densification process. *Materials Science and Engineering a-Structural Materials Properties Microstructure and Processing*, 428(1-2):98–105, 2006.
- [75] X. Guo, W. Sigle, J. Fleig, and J. Maier. Role of space charge in the grain boundary blocking effect in doped zirconia. *Solid State Ionics*, 154:555–561, 2002.
- [76] R. A. De Souza, M. J. Pietrowski, U. Anselmi-Tamburini, S. Kim, Z. A. Munir, and M. Martin. Oxygen diffusion in nanocrystalline yttria-stabilized zirconia: the effect of grain boundaries. *Physical Chemistry Chemical Physics*, 10(15):2067–2072, 2008.
- [77] J. Garcia-Barriocanal, A. Rivera-Calzada, M. Varela, Z. Sefrioui, E. Iborra, C. Leon, S. J. Pennycook, and J. Santamaria. Colossal Ionic Conductivity at Interfaces of Epitaxial ZrO<sub>2</sub>:Y<sub>2</sub>O<sub>3</sub>/SrTiO<sub>3</sub> Heterostructures. *Science (Washington, DC, U. S.)*, 321(5889):676–680, 2008.
- [78] X. Guo. Comment on "Colossal Ionic Conductivity at Interfaces of Epitaxial ZrO<sub>2</sub>:Y<sub>2</sub>O<sub>3</sub>/SrTiO<sub>3</sub> Heterostructures". *Science*, 324(5926):–, 2009.
- [79] J. Garcia-Barriocanal, A. Rivera-Calzada, M. Varela, Z. Sefrioui, E. Iborra, C. Leon, S. J. Pennycook, and J. Santamaria. Response to Comment on "Colossal Ionic Conductivity at Interfaces of Epitaxial ZrO<sub>2</sub>:Y<sub>2</sub>O<sub>3</sub>/SrTiO<sub>3</sub> Heterostructures". *Science*, 324(5926):–, 2009.
- [80] X. Guo. Can we achieve significantly higher ionic conductivity in nanostructured zirconia? *Scripta Materialia*, 65(2):96–101, 2011.

- [81] H. R. Kim, J. C. Kim, K. R. Lee, H. I. Ji, H. W. Lee, J. H. Lee, and J. W. Son. 'Illusional' nano-size effect due to artifacts of in-plane conductivity measurements of ultra-thin films. *Physical Chemistry Chemical Physics*, 13(13):6133–6137, 2011.
- [82] W. Araki and Y. Arai. Optimum strain state for oxygen diffusion in yttria-stabilised zirconia. *Solid State Ionics*, 190(1):75–81, 2011.
- [83] Xin Guo, Enrique Vasco, Shaobo Mi, Kristof Szot, Eric Wachsman, and Rainer Waser. Ionic conduction in zirconia films of nanometer thickness. *Acta Materialia*, 53(19):5161–5166, 2005.
- [84] X. Guo. Physical Origin of the Intrinsic Grain-Boundary Resistivity of Stabilized-Zirconia - Role of the Space-Charge Layers. *Solid State Ionics*, 81(3-4):235–242, 1995.
- [85] X. Guo and R. Waser. Electrical properties of the grain boundaries of oxygen ion conductors: Acceptor-doped zirconia and ceria. *Progress in Materials Science*, 51(2):151–210, 2006.
- [86] N. Navickas, M. Gerstl, G. Friedbacher, F. Kubel, and Fleig J. Measurement of the across-plane conductivity of YSZ thin films on silicon. *Solid State Ionics*, In print, 2012.
- [87] Chunwen Sun and Ulrich Stimming. Recent anode advances in solid oxide fuel cells. *Journal of Power Sources*, 171(2):247 – 260, 2007.
- [88] Chunwen Sun, Rob Hui, and Justin Roller. Cathode materials for solid oxide fuel cells: a review. *Journal of Solid State Electrochemistry*, 14:1125–1144, 2010.
- [89] Norbert Menzler, Frank Tietz, Sven Uhlenbruck, Hans Buchkremer, and Detlev Stöver. Materials and manufacturing technologies for solid oxide fuel cells. *Journal of Materials Science*, 45:3109–3135, 2010.

- [90] M. Gerstl. Stromgetriebener Einbau und Diffusion von Tracerionen in Yttrium stabilisiertem Zirconiumdioxid. Master's thesis, Vienna University of Technology, 2008.
- [91] David Lide, editor. *Handbook of Chemistry and Physics*. CRC Press, Washington D.C., 2004.
- [92] Wolfgang G. Bessler, Marcel Vogler, Heike Stormer, Dagmar Gerthsen, Annika Utz, Andre Weber, and Ellen Ivers-Tiffée. Model anodes and anode models for understanding the mechanism of hydrogen oxidation in solid oxide fuel cells. *Phys. Chem. Chem. Phys.*, 12:13888–13903, 2010.
- [93] Lorenzo Malavasi, Craig A. J. Fisher, and M. Saiful Islam. Oxide-ion and proton conducting electrolyte materials for clean energy applications: structural and mechanistic features. *Chem. Soc. Rev.*, 39:4370–4387, 2010.
- [94] M. Riordan and L. Hoddeson. The origins of the pn junction. *Spectrum, IEEE*, 34(6):46–51, jun 1997.
- [95] F. A. Kroger and H. J. Vink. Relations between concentrations of imperfections in crystalline solids. *Solid State Physics*, 3:307–435, 1956.
- [96] Wikipedia. Frenkel defect — Wikipedia, the free encyclopedia. [Online; accessed 6-January-2012], 2011. [http://en.wikipedia.org/w/index.php?title=Frenkel\\_defect&oldid=464877261](http://en.wikipedia.org/w/index.php?title=Frenkel_defect&oldid=464877261).
- [97] Wikipedia. Schottky defect — Wikipedia, the free encyclopedia. [Online; accessed 6-January-2012], 2011. [http://en.wikipedia.org/w/index.php?title=Schottky\\_defect&oldid=460763067](http://en.wikipedia.org/w/index.php?title=Schottky_defect&oldid=460763067).
- [98] Junichiro Mizusaki, Hideomi Koinuma, Junichi Shimoyama, Masashi Kawasaki, and Kazuo. Fueki. High temperature gravimetric study on nonstoichiometry and

- oxygen adsorption of tin dioxide. *Journal of Solid State Chemistry*, 88(2):443–50, 1990.
- [99] K. Persels Constant, T. O. Mason, and J. L. Routbort. Nonstoichiometry, electrical properties, and cation diffusion in highly non-stoichiometric cobalt oxide (Co<sub>1-x</sub>O). II. Modeling the defect structure. *Journal of Physics and Chemistry of Solids*, 53(3):413–18, 1992.
- [100] K. Persels Constant, T. O. Mason, S. J. Rothman, and J. L. Routbort. Nonstoichiometry, electrical properties, and cation diffusion in highly non-stoichiometric cobalt oxide (Co<sub>1-x</sub>O). I. Experimental. *Journal of Physics and Chemistry of Solids*, 53(3):405–11, 1992.
- [101] Juergen Fleig. *Electrical and Electrochemical Investigation of Inhomogeneities in Solid State Ionics*. 2002.
- [102] Yet Ming Chiang, Dunbar III Birnie, and W. David Kingery. *Physical Ceramics*. John Wiley & Sons, Inc., 1997.
- [103] H. L. Tuller and A. S. Nowick. Defect Structure and Electrical Properties of Nonstoichiometric CeO<sub>2</sub> Single Crystals. *Journal of The Electrochemical Society*, 126(2):209–217, 1979.
- [104] Adolf Fick. Ueber Diffusion. *Annalen der Physik*, 170(1):59–86, 1855.
- [105] John Crank. *The Mathematics of Diffusion*. Oxford University Press, 1980.
- [106] G. J. McCarthy, D. E. Pfoertsch, and M. T. Davidson. Development of Supercalcine Formulations for Solidification of High-Level Nuclear Wastes. *American Ceramic Society Bulletin*, 56(3):338–338, 1977.
- [107] H. G. Scott. Phase relationships in the zirconia-yttria system. *Journal of Materials Science*, 10:1527–1535, 1975.

- [108] University of Cambridge DoITPoMS. YSZ. [Online; accessed 6-January-2012]. [http://www.doitpoms.ac.uk/tlplib/fuel-cells/figures/YSZ\\_sml.png](http://www.doitpoms.ac.uk/tlplib/fuel-cells/figures/YSZ_sml.png).
- [109] Shyh Lung Hwang and I. Wei. Chen. Grain size control of tetragonal zirconia polycrystals using the space charge concept. *Journal of the American Ceramic Society*, 73(11):3269–77, 1990.
- [110] J. Jamnik, J. Maier, and S. Pejovnik. Interfaces in solid ionic conductors: equilibrium and small signal picture. *Solid State Ionics*, 75:51–8, 1995.
- [111] J. Fleig and J. Maier. Finite-element calculations on the impedance of electroceramics with highly resistive grain boundaries: I- laterally inhomogeneous grain boundaries. *Journal of the American Ceramic Society*, 82(12):3485–3493, 1999.
- [112] P. S. Manning, J. D. Sirman, R. A. DeSouza, and J. A. Kilner. The kinetics of oxygen transport in 9.5 mol stabilised zirconia. *Solid State Ionics*, 100(1-2):1–10, 1997.
- [113] M. Weller, R. Herzog, M. Kilo, G. Borchardt, S. Weber, and S. Scherrer. Oxygen mobility in yttria-doped zirconia studied by internal friction, electrical conductivity and tracer diffusion experiments. *Solid State Ionics*, 175(1-4):409–413, 2004.
- [114] J. Ross Macdonald, editor. *Impedance Spectroscopy*. John Wiley & Sons, Inc., 1987.
- [115] Z. Stoyanov and Vladikova D. *Differential Impedance analysis*. Marin Drinov Academic Publishing House, 2005.
- [116] Alexander K. Opitz, Alexander Lutz, Markus Kubicek, Frank Kubel, Herbert Hutter, and Juergen. Fleig. Investigation of the oxygen exchange mechanism on Pt—yttria stabilized zirconia at intermediate temperatures: Surface path versus bulk path. *Electrochimica Acta*, 56(27):9727–9740, 2011.

- [117] Alexander Karl Opitz, Arno Schintlmeister, Herbert Hutter, and Juergen. Fleig. Visualization of oxygen reduction sites at Pt electrodes on YSZ by means of  $^{18}\text{O}$  tracer incorporation: the width of the electrochemically active zone. *Physical Chemistry Chemical Physics*, 12(39):12734–12745, 2010.
- [118] C. Hamann and W. Vielstich. *Elektrochemie*. 2005.
- [119] R. Meyer, X. Guo, and R. Waser. Nonlinear electrical properties of grain boundaries in oxygen ion conductors - Modeling the varistor behavior. *Electrochemical and Solid State Letters*, 8(10):E67–E69, 2005.
- [120] X. Guo, S. B. Mi, and R. Waser. Nonlinear electrical properties of grain boundaries in oxygen ion conductors: Acceptor-doped ceria. *Electrochemical and Solid State Letters*, 8(1):J1–J3, 2005.
- [121] M. L. Pacholski and N. Winograd. Imaging with Mass Spectrometry. *Chemical Reviews (Washington, D. C.)*, 99(10):2977–3005, 1999.
- [122] T. Froemling. *Oxide Ion Transport in Donor Doped Lead Zirconate Titanate*. PhD thesis, Technische Universität Wien, 2011.
- [123] Ming L. Yu. Work-function dependence of negative-ion production during sputtering. *Physical Review Letters*, 40(9):574–7, 1978.
- [124] A. Schintlmeister. PhD thesis, Technische Universität Wien, 2012.
- [125] Reinhard Schwarz. PLD. [Online; accessed 6-January-2012]. [http://groups.ist.utl.pt/rschwarz/rschwarzgroup\\_files/PLD\\_files/PLD\\_schem.jpg](http://groups.ist.utl.pt/rschwarz/rschwarzgroup_files/PLD_files/PLD_schem.jpg).
- [126] Crystec GmbH. *Data Sheet for Sapphire for Research and Development*. Crystec, Koepenicker Str. 325, Berlin, Germany.
- [127] J. E. Bauerle. Study of Solid Electrolyte Polarization by a Complex Admittance Method. *Journal of Physics and Chemistry of Solids*, 30(12):2657–&, 1969.

- [128] J. Maier. On the Conductivity of Polycrystalline Materials. *Berichte Der Bunsen-Gesellschaft-Physical Chemistry Chemical Physics*, 90(1):26–33, 1986.
- [129] J. Fleig and J. Maier. The impedance of ceramics with highly resistive grain boundaries: Validity and limits of the brick layer model. *Journal of the European Ceramic Society*, 19(6-7):693–696, 1999.
- [130] N. J. Kidner, Z. J. Homrighaus, T. O. Mason, and E. J. Garboczi. Modeling interdigital electrode structures for the dielectric characterization of electroceramic thin films. *Thin Solid Films*, 496(2):539–545, 2006.
- [131] N. J. Kidner, A. Meier, Z. J. Homrighaus, B. W. Wessels, T. O. Mason, and E. J. Garboczi. Complex electrical (impedance/dielectric) properties of electroceramic thin films by impedance spectroscopy with interdigital electrodes. *Thin Solid Films*, 515(11):4588–4595, 2007.
- [132] M. G. H. M. Hendriks, J. E. ten Elshof, H. J. M. Bouwmeester, and H. Verweij. The electrochemical double-layer capacitance of yttria-stabilised zirconia. *Solid State Ionics*, 146(3-4):211–217, 2002.
- [133] N. H. Perry, S. Kim, and T. O. Mason. Local electrical and dielectric properties of nanocrystalline yttria-stabilized zirconia. *Journal of Materials Science*, 43(14):4684–4692, 2008.
- [134] J. W. Jang, H. K. Kim, and D. Y. Lee. The effect of tetravalent dopants on the unit cell volume of 2Y-TZP and 8Y-SZ. *Materials Letters*, 58(7-8):1160–1163, 2004.
- [135] J. Fleig. The grain boundary impedance of random microstructures: numerical simulations and implications for the analysis of experimental data. *Solid State Ionics*, 150(1-2):181–193, 2002.
- [136] G. Garcia, J. Santiso, J. A. Pardo, and A. Figueras. Epitaxial growth of YSZ films

- prepared by pulsed injection MOCVD. *Applied Surface Science*, 233(1-4):191–196, 2004.
- [137] F. Lallet and N. Olivi-Tran. Sol-gel obtained YSZ nanocrystals on a substrate: A Monte Carlo approach of the crystallographic orientation. *Journal of Luminescence*, 129(12):1767–1770, 2009.
- [138] S. Raz, K. Sasaki, J. Maier, and I. Riess. Characterization of adsorbed water layers on Y<sub>2</sub>O<sub>3</sub>-doped ZrO<sub>2</sub>. *Solid State Ionics*, 143(2):181–204, 2001.
- [139] S. Kim, H. J. Avila-Paredes, S. Z. Wang, C. T. Chen, R. A. De Souza, M. Martin, and Z. A. Munir. On the conduction pathway for protons in nanocrystalline yttria-stabilized zirconia. *Physical Chemistry Chemical Physics*, 11(17):3035–3038, 2009.
- [140] H. J. Avila-Paredes, E. Barrera-Calva, H. U. Anderson, R. A. De Souza, M. Martin, Z. A. Munir, and S. Kim. Room-temperature protonic conduction in nanocrystalline films of yttria-stabilized zirconia. *Journal of Materials Chemistry*, 20(30):6235–6238, 2010.
- [141] H. J. Avila-Paredes, J. F. Zhao, S. Z. Wang, M. Pietrowski, R. A. De Souza, A. Reinholdt, Z. A. Munir, M. Martin, and S. Kim. Protonic conductivity of nano-structured yttria-stabilized zirconia: Dependence on grain size. *Journal of Materials Chemistry*, 20(5):990–994, 2010.
- [142] B. Butz, P. Kruse, H. Stormer, D. Gerthsen, A. Muller, A. Weber, and E. Ivers-Tiffée. Correlation between microstructure and degradation in conductivity for cubic Y<sub>2</sub>O<sub>3</sub>-doped ZrO<sub>2</sub>. *Solid State Ionics*, 177(37-38):3275–3284, 2006.
- [143] M. Gerstl, E. Navickas, G. Friedbacher, F. Kubel, M. Ahrens, and J. Fleig. The relevance of interfaces for oxide ion conduction and diffusion in yttria stabilized zirconia (YSZ) thin films. *Phys. Chem. Chem. Phys.*, submitted, 2012.

- [144] K. Sasaki and J. Maier. Chemical surface exchange of oxygen on Y<sub>2</sub>O<sub>3</sub>-stabilized ZrO<sub>2</sub>. *Solid State Ionics*, 161(1-2):145–154, 2003.
- [145] A.V. Berenov, A. Atkinson, J.A. Kilner, E. Bucher, and W. Sitte. Oxygen tracer diffusion and surface exchange kinetics in La<sub>0.6</sub>Sr<sub>0.4</sub>CoO<sub>3</sub>. *Solid State Ionics*, 181(17-18):819 – 826, 2010.
- [146] Marcus Rohnke, Jürgen Janek, John A Kilner, and Richard J Chater. Surface oxygen exchange between yttria-stabilised zirconia and a low-temperature oxygen rf-plasma. *Solid State Ionics*, 166(1-2):89 – 102, 2004.
- [147] J. Fleig. Voltage-assisted O-18 tracer incorporation into oxides for obtaining shallow diffusion profiles and for measuring ionic transference numbers: basic considerations. *Physical Chemistry Chemical Physics*, 11(17):3144–3151, 2009.
- [148] H. Huang, J. H. Shim, C. C. Chao, R. Pornprasertsuk, M. Sugawara, T. M. Gur, and F. B. Prinz. Characteristics of Oxygen Reduction on Nanocrystalline YSZ. *Journal of the Electrochemical Society*, 156(3):B392–B396, 2009.
- [149] J. D. Hanawalt, H. W. Rinn, and L. K. Frevel. Chemical analysis by x-ray diffraction - Classification and use of x-ray diffraction patterns. *Industrial and Engineering Chemistry-Analytical Edition*, 10:0457–0512, 1938.
- [150] M. Vollmann, R. Hagenbeck, and R. Waser. Grain-boundary defect chemistry of acceptor-doped titanates: Inversion layer and low-field conduction. *Journal of the American Ceramic Society*, 80(9):2301–2314, 1997.
- [151] J. J. Zhu, J. G. van Ommen, H. J. M. Bouwmeester, and L. Lefferts. Activation of O<sub>2</sub> and CH<sub>4</sub> on yttrium-stabilized zirconia for the partial oxidation of methane to synthesis gas. *Journal of Catalysis*, 233(2):434–441, 2005.

# List of Constants

$e$	Elementary charge, $e = 1.602 \cdot 10^{-19}$ C
$e$	EULER's number, $e = 2.718 \dots$
$\varepsilon_0$	Electric constant (vacuum permittivity), $\varepsilon_0 = 8.854 \cdot 10^{-12}$ F/m
$F$	FARADAY's constant, $F = 96485.3366$ C/mol
$i$	Imaginary number, $i^2 = -1$
$k_B$	BOLTZMANN's constant, $k_B = 8.617 \cdot 10^{-5}$ eV/K = $1.381 \cdot 10^{-23}$ J/K
$N_A$	AVOGADRO's constant, $N_A = 6.022 \cdot 10^{23}$ mol <sup>-1</sup>
$\pi$	Pi, $\pi = 3.142 \dots$
$R_G$	Ideal gas constant, $R_G = 8.314$ J·mol <sup>-1</sup> K <sup>-1</sup>

# List of Abbreviations

1-xtal	Single crystal
AC	Alternating current
AFM	Atomic force microscopy
CPE	Constant phase element
C.S.	Crystallite size
CSZ	Calcia stabilized zirconia
DC	Direct current
DHM	Digital holographic microscopy
FEM	Finite element method
GB	Grain boundary
GDC	Gadolinia doped ceria
L.C.	Lattice constant
LSC	Lanthanum strontium cobalt oxide
LSCF	Lanthanum strontium cobalt iron oxide
LSM	Lanthanum strontium manganite
PLD	Pulsed laser deposition
SIMS	Secondary ion mass spectrometry
SOFC	Solid oxide fuel cell

SSZ	Scandia stabilized zirconia
STO	Strontium titanate
TOF	Time of flight
UHV	Ultra high vacuum
XRD	X-ray diffraction
YSZ	Yttria stabilized zirconia

# List of Symbols

$a_k$	Activation term of species $k$
$\alpha$	Charge transfer coefficient
$A$	Electrode area
$B$	Electrode width
$b$	Width of initial tracer concentration box profile
$c_{gas}$	Relative tracer concentration in the gas phase
$c_i$	Volume concentration of species $i$
$c(x, t)$	Relative tracer concentration, dependent on time and position
$c_0$	Initial concentration of the tracer enriched area
$c_{18O}$	Relative $^{18}O$ concentration
$c_{bg}$	Tracer background concentration
$C$	Capacitance or Capacitor
$C_{Bulk}$	Bulk capacitance
$C_{Electrode}$	Electrode capacitance
$C_{GB}$	Grain boundary capacitance
$C_{Stray}$	Total stray capacitance
$C_{Substrate}$	Substrate stray capacitance
$C_{Wiring}$	Stray capacitance of wiring and setup

$CPE_{Bulk}$	CPE modelling the bulk capacitance
$CPE_{GB}$	CPE modelling the grain boundary capacitance
$CPE_{Stray}$	CPE modelling the total stray capacitance
$d_G$	Lateral grain size
$d_{GB}$	Width of the electrically relevant grain boundary
$\delta$	Partial pressure dependent parameter of non stoichiometry
$D$	Electrode spacing
$D^*$	Tracer diffusion coefficient
$D^\sigma$	Conductivity based diffusion coefficient
$D_k$	Self diffusion coefficient of particle $k$
$\Delta G_D$	Free enthalpy of defect formation
$\Delta G_R$	Free enthalpy of reaction
$\Delta H_D$	Enthalpy of defect formation
$\Delta H_R$	Enthalpy of reaction
$\Delta S_D$	Entropy of defect formation
$\Delta S_R$	Entropy of reaction
$e^- , e'$	Electron
$\varepsilon_r$	Relative permittivity of species $r$
$\eta$	Overpotential
$E_0$	Standard potential
$E_a$	Activation energy
$f_{Geometry}$	Geometric correction factor
$h$	$h = \frac{k^*}{D^*}$
$H$	Film thickness
$H_R$	HAVEN ratio: $H_R = \frac{D^*}{D^\sigma}$
$I$	Current
$I(t)$	Alternating current

$\hat{I}$	Amplitude of an alternating current
$j$	Current density
$j_0$	Exchange current density
$J_k$	Flux of species $k$
$k^*$	Surface tracer exchange coefficient
$L$	Electrode length
$L_a$	Length of fixed flight path in TOF-SIMS
$m$	Mass
$\mu_0$	Standard chemical potential
$\mu_k$	Chemical potential of species $k$
$\tilde{\mu}_k$	Electrochemical potential of species $k$
$M$	Modulus
$M'$	Real part of the modulus
$M''$	Imaginary part of the modulus
$n_i$	Volume concentration of lattice positions of species $i$
$\omega$	Angular frequency
$\omega_{Peak}$	Peak frequency of an RC equivalent circuit
$p_k$	Partial pressure of species $k$
$\phi$	Electric potential
$P$	Product of resistance and capacitance in an RC equivalent circuit: $P = R \cdot C$
$P_B$	$P$ for the grain bulk RC equivalent circuit
$P_{GB}$	$P$ for the grain boundary RC equivalent circuit
$q$	Charge of an ion
$Q$	Factor in the impedance of a CPE: $Z_{CPE} = Q^{-1} (i \cdot \omega)^{-r}$
$Q_{GB}$	Parameter $Q$ of a CPE modelling the grain boundary capacitance
$r$	See definition of $Q$
$R$	Resistance or Resistor

$R_{Bulk}$	Bulk resistance
$R_{GB}$	Grain boundary resistance
$\sigma_0$	Pre-exponential factor in the ARRHENIUS equation for the conductivity
$\sigma_{Bulk}$	Bulk conductivity
$\sigma_{GB}$	Grain boundary conductivity
$\sigma_k$	Conductivity of species $k$
$S_i$	Signal intensity of species $i$ measured in TOF-SIMS
$t$	Time
$t_{ex}$	Exchange time in a tracer exchange experiment
$t_F$	Time of flight in a TOF-SIMS analysis
$\theta$	Incident angle in a diffraction pattern
$T$	Absolute temperature
$u_k$	Mobility of species $k$
$U$	Voltage
$U(t)$	Alternating voltage
$\hat{U}$	Amplitude of an alternating voltage
$U(t)$	Alternating voltage
$U_A$	Voltage accelerating ions the TOF-SIMS machine
$v$	Velocity
$Z$	Impedance
$Z'$	Real part of the impedance
$Z''$	Imaginary part of the impedance
$z_k$	Charge number of species $k$

# List of Figures

2.1	Sketch of a working solid oxide fuel cell (SOFC). While anode and cathode have to be conducting for both electrons and oxygen ions, it is imperative that the electrolyte is blocking to electronic current, otherwise there is an internal short circuit and the power output is decreased dramatically. Further information about the cermet Ni/YSZ and lanthanum strontium manganate (LSM) as examples for anode and cathode materials are found in [87–89]. Image modified from Ref. [90]. . . . .	6
2.2	Intrinsic point defects visualized on the (1 0 0) plane of a cubic AgCl single crystal. $\text{Ag}^+$ ions are represented by the red and $\text{Cl}^-$ ions by the green dots. Images adapted from Refs. [96, 97] . . . . .	9
2.3	BROUWER diagrams of the point defect concentrations for an (a) undoped and (b) a negatively doped metal oxide of type $\text{MO}_{1-\delta}$ . In (c) the conductivities of the point defects of the metal oxide in (b) are plotted. Images adapted from Ref. [101]. . . . .	12

2.4	Phase diagram of YSZ in the zirconia rich portion of the zirconia-yttria system. Note that the x-axis indicates the mole percent of $YO_{1.5}$ rather than $Y_2O_3$ . Non-equilibrium homogeneous phases are indicated at the lower margin. The symbols indicate phases found at room temperature: Open circles for the cubic, filled circles for the tetragonal and squares for the monoclinic phase. The hatched region indicates a non-equilibrium monoclinic-tetragonal transition, see image source in Ref. [107]. . . . .	17
2.5	Fluorite type crystal structure of cubic zirconia and a graphic visualization of the generation of oxygen vacancies by yttria doping. Image source: Ref. [108] . . . . .	17
2.6	Schematic representation of the oxygen vacancy concentration change across a grain boundary in YSZ according to Ref. [85]. The shaded region highlights the grain boundary space charge region with the electric grain boundary width $d_{GB}$ . . . . .	19
2.7	Schematic representations of measurements of phenomenological diffusion coefficients according to Ref. [39]: (a) conductivity experiment, (b) tracer exchange experiment, (c) partial pressure change experiment. . . . .	20
2.8	Graphical representations of impedance data in NYQUIST (a),(c), and modulus plots (b), (d). The equivalent circuits with their respective values are given in each diagram, the arrow denotes the direction of decreasing frequency. Note how the diameters of the semi-circles in the NYQUIST plots in (a) and (c) directly represent a resistance in the equivalent circuit. In the modulus plot in (b) the diameter of the semi-circle gives the inverse of $C_1$ , while in (d) the rightmost intercept is equal to $(C_1 + C_2)^{-1}$ . . . .	27

2.9	Graphic representation of the BUTLER-VOLMER equation in eq. 2.35. The blue line represents the anodic current in the first term, while the green one gives the cathodic current in the second term of eq. 2.35. The red line is the sum of both currents. The dashed black line is a linear approximation close to $\eta = 0$ . . . . .	30
2.10	Mass spectra of the (a) $^{16}\text{O}$ and (b) $^{18}\text{O}$ signals recorded in a typical measurement (Sample Sap-PLD 2; lateral diffusion under the free YSZ Surface, see Table 7.2). The $^{18}\text{O}$ signal in (b) is of ideal box-shape with a length equal to the primary ion pulse duration of 90 ns. The red and blue lines correspond to partial evaluations of the top or bottom regions in the lateral intensity images in Fig. 2.11, while the black line represents the total area. Due to the high signal count, the black lines scale with the right y-axis. The rectangular boxes highlight the integrated area of 20 ns used for calculating $c_{^{18}\text{O}}$ with eq. 2.37. Note the different scaling of the x-axis. . . . .	32
2.11	Lateral intensity distributions of the (a) $^{16}\text{O}$ , (b) $^{18}\text{O}$ signals and the (c) normalized concentration $c_{^{18}\text{O}}$ according to eq. 2.37 (Sample Sap-PLD 2; lateral diffusion under the free YSZ surface, see Table 7.2). The red and blue rectangles in (a) and (b) highlight the regions used to illustrate the signal shift between top and bottom region in Fig. 2.10. The two red boxes in (c) mark the integrated area for the lateral diffusion profiles in Fig. 2.12; the slightly distorted rectangular shape was necessary to exactly align with the $c_{^{18}\text{O}}$ box profile, see also chapter 7. . . . .	33

2.12	Lateral diffusion profiles of a typical sample (Layer Sap-PLD 2; lateral diffusion under the free YSZ surface, see Table 7.2) (a) without and (b) with baseline correction. The data was extracted from the highlighted area in Fig. 2.11(c). The blue line in (a) is the manually drawn baseline, which has been subtracted in (b). The fit curve in (b) was calculated by eq. 7.3. . . . . .	34
3.1	Sketch of the pulsed laser deposition (PLD) setup used. Image slightly modified from Ref. [125]. . . . .	37
3.2	Spin coating of the substrate (green) and pre-baking of the photoresist (orange) → Exposure of the photoresist to UV light through a photomask → Parts of the resist have polymerized (toughened) → Removal of the unexposed photoresist with developing agent → Application of Cr/Au double layer → Removal of exposed resist with acetone . . . . .	38
3.3	Example of a grain size evaluation using intercepts (red vertical lines) on reference lines (blue). The yellow areas of the reference lines outside the AFM image were not considered in the automated calculation. Example image taken from layer B, see Table 5.1 . . . . .	40
3.4	Impedance spectra in (a) NYQUIST and (b) modulus plots of a 28 nm YSZ thin film with 440 nm grain size (Sap-SG 1 in Table 7.1 or layer E in Table 5.1) at 300°C. The spectrum recorded with a 0.1 V amplitude (red line) shows significantly more data scattering than the spectrum recorded with a 1 V amplitude (blue line), but no systematic deviation is found. Both spectra were recorded on the same interdigital electrodes with a 25 μm spacing, 10 μm width and a total length of 9.0 cm. Data points at 50 and 100 Hz are removed as extreme outliers. . . . .	42

3.5	Cross section of a potential distribution of an electrode finger with 5 $\mu\text{m}$ width and 10 $\mu\text{m}$ spacing. The dimension of the x- and y-axis dimension is in meters, the colour code defines the potential in volts. . . . .	45
4.1	(a) Sketch of the measurement setup. $L$ denotes the length of the electrodes, $B$ their width, and $D$ the distance between them. The thickness of the layer is referred to as $H$ , the grain size is labelled $d_G$ , and the electrical grain boundary thickness as $d_{GB}$ . (b) Equivalent circuit representing a thin ion conducting layer on an insulating substrate. (c) Modified equivalent circuit used to fit all recorded impedance spectra in this study; capacitances are replaced by constant phase elements. . . . .	47
4.2	Schematic sketches of the different electrode geometries, images are not to scale. (a) Geometry (1) according to Ref. [31]: two large area electrodes that cover the whole sample surface (1 x 1 $\text{cm}^2$ ), except a gap of 2 mm. A similar geometry is used in the present experimental work with a spacing of only 500 $\mu\text{m}$ . (b) Geometry (2) according to Ref. [16]: two wide electrodes (4 mm long, 100 $\mu\text{m}$ wide) with a spacing of 68 $\mu\text{m}$ . (c) Geometry (3) applied in the present experimental study: Narrow interdigital stripe electrodes connected to current collectors. Effective length of the individual finger is 400 $\mu\text{m}$ . Spacings are 25 $\mu\text{m}$ or 10 $\mu\text{m}$ and electrode width 10 $\mu\text{m}$ or 5 $\mu\text{m}$ . Usually several hundred fingers are connected in parallel leading to effective lengths of about 10 cm. . . . .	50

4.3	Simulated impedance spectra using the equivalent circuit in Fig. 4.1(b) in the frequency range from 1 MHz to 0.001 Hz with 10 points per decade for a 1 cm long electrode. The capacitances used in (a), (b) (c), and (d) are listed in Table 4.1. The bulk and grain boundary resistances for (a) and (b) were set to $R_{Bulk} = 0.1 \text{ G}\Omega$ and $R_{GB} = 2 \text{ G}\Omega$ and to $R_{Bulk} = 0.5 \text{ G}\Omega$ and $R_{GB} = 2 \text{ G}\Omega$ for (c) and (d). In (a) and (c) the Nyquist plots are shown. In (b) and (d) the complex modulus plots are depicted, the inset in (b) has another scaling to show all spectra in one graph. The red, blue, and green lines are fits to the equivalent circuit in Fig. 4.1(c). . . . .	52
4.4	XRD patterns of as prepared (a) Layer A (105 nm thin), (b) Layer B (18 nm) and (c) Layer C (32 nm). In the legend L.C. means the lattice constant of the cubic YSZ layer and C.S. the crystallite size in the (1 1 1) direction. In (b) and (c) the red line corresponds to a measurement after annealing at 1000 °C for 5 h. The inlay in (b) and (c) shows a magnification of the (1 1 1) reflex. . . . .	57
4.5	AFM image of the surface of layer A. . . . .	58
4.6	Several interdigit electrode geometries on layer A. The broad perpendicular stripes are the current collectors. . . . .	59

- 4.7 Impedance spectra measured on layer A (105 nm thin) with two different electrode geometries at 300°C. Frequency range was 1 MHz to 1 Hz with 10 points per decade. Diagram (a) is a Nyquist-plot, (b) is a modulus-plot of the data. Geometry (3) is an interdigital electrode, see Fig. 4.2(c), with 5  $\mu\text{m}$  broad fingers having a distance of 10  $\mu\text{m}$ , the effective electrode length was measured to be 14.40 cm. Geometry (1) consists of approximately 5 mm broad, 500  $\mu\text{m}$  spaced stripes of 8 mm length as in Fig. 4.2(a). For easier comparison of the different shapes of the spectra different scales are used for geometry (3) (black) and geometry (1) (blue). The red lines are fitting results for geometry (3) with an  $R - CPE$  equivalent circuit (dotted line) and the circuit in Fig. 4.1(c) (solid line). The solid blue line is a fit to data from geometry (1) with a single  $R - CPE$  equivalent circuit ( $r \approx 1$ ). The arrows indicate the appropriate axis scales. . . . . 60
- 4.8 ARRHENIUS plot of the conductivities measured with different electrode geometries on layer A (105 nm thin). In the caption the corresponding distances ( $D$ ) and widths ( $B$ ) are specified in  $\mu\text{m}$ . The solid red (9.5 % YSZ single crystal) and dotted green (8 % YSZ polycrystal) lines are macroscopic bulk measurements plotted for comparison. The solid black line is the effective total conductivity of the film measured with geometry (1). . . . . 65
- 4.9 Modulus plot of impedance spectra recorded on layer C (32 nm thin) at 300°C. Please note the different scalings used for the spectra in order to allow easier comparison. The open circles (black axis scale) correspond to 1 h annealing time at 1000°C, the open squares (blue axis scale) to 5 h at 1000°C. The solid red and blue line represent the corresponding fit functions obtained by using the equivalent circuit depicted in Fig. 4.1(c). In both cases the electrode geometry consisted of 25  $\mu\text{m}$  spaced 5  $\mu\text{m}$  broad electrodes. The arrows indicate the appropriate axis scales. . . . . 67

4.10	(a) Change of grain boundary capacitance and (b) substrate stray capacitance with annealing time for layer B and C at 1000°C. The solid lines in (a) are linear fits of the data. The stray capacitances plotted in (b) are not calculated by eq. 4.6, but values of $Q$ were taken for $r > 0.98$ . The values and the error bars in (a) and (b) are calculated from several spectra recorded at temperatures from 250 to 550°C. The open symbols in (a) and (b) at 0 h annealing indicate that meaningful fit results could not be obtained in that case. . . . .	68
4.11	ARRHENIUS plot of the grain bulk conductivities measured on layer B (18 nm thickness) and C (32 nm) with different annealing times at 1000°C. Bulk conductivities of macroscopic samples are plotted for comparison (9.5% YSZ single crystal and 8% YSZ polycrystal). . . . .	71
5.1	AFM images of the surfaces of (a) layer B, (b) layer C, (c) layer D, and (d) layer E. The arrows in (b) and (c) mark examples of different grain morphology. The arrow in (d) marks a pore. . . . .	76
5.2	XRD patterns of the YSZ (a) (200), (b) (111) reflections of layers A to E.	78
5.3	Impedance spectrum of layer D at 350°C in (a) Nyquist and (b) Modulus plots. The inset in (b) depicts the equivalent circuit to fit the data, see chapter 4. $R_{Bulk}$ and $R_{GB}$ are the resistances for bulk and grain boundaries in YSZ. $CPE_{GB}$ and $CPE_{Stray}$ are the constant phase elements used to model the grain boundary and stray capacitance, see Ref. [18] and chapter 4. . . . .	79
5.4	ARRHENIUS plots of (a) the total conductivities and (b) the grain and grain boundary conductivities measured on layers A to E. The red and green lines are macroscopic bulk measurements plotted for comparison. . .	81

6.1	Sketch of the set-up for the current driven tracer incorporation. The question marks indicate that the exact implantation area is yet unknown .	86
6.2	Situation after the tracer incorporation step: TOF-SIMS ion images of layer S in (a) side-view and (b) cross-sectional view of the $^{18}\text{O}$ concentration $c_{^{18}\text{O}}$ calculated by eq. 2.37. (c) Lateral concentration profile integrated along the x-axis. The x, y and z directions are the same as in Fig. 6.1. . . . .	88
6.3	Situation after the tracer diffusion step: TOF-SIMS ion images of layer S in (a) side-view and (b) cross-sectional view of the $^{18}\text{O}$ concentration $c_{^{18}\text{O}}$ calculated by eq. 2.37. (c) Two lateral concentration profiles integrated along the x-axis measured under a free YSZ surface or a Pt-covered one, respectively. The black fit curves were calculated with eq. 7.3. The x, y and z directions are the same as in Fig. 6.1. . . . .	89
6.4	Situation after the tracer incorporation step: TOF-SIMS ion images of layer F in (a) side-view and (b) cross-sectional view of the $^{18}\text{O}$ concentration $c_{^{18}\text{O}}$ calculated by eq. 2.37. (c) Lateral concentration profile integrated along the x-axis, the inset shows the data with a different scaling of the y-axis. The x, y and z directions are the same as in Fig. 6.1. . . . .	93
6.5	Situation after a 10 minute heat treatment at 300°C: TOF-SIMS ion images of layer F in (a) side-view and (b) cross-sectional view of the $^{18}\text{O}$ concentration $c_{^{18}\text{O}}$ calculated by eq. 2.37. (c) Lateral concentration profile integrated along the x-axis. The x, y and z directions are the same as in Fig. 6.1. . . . .	94

7.1	Depth profile of the $^{18}\text{O}$ concentration of a hypothetical 100 nm thin YSZ layer after an entropy driven gas exchange for 30 minutes at 300°C (incorporation step), the inset shows a magnification of the same profile. Surface tracer exchange coefficient $k^* = 1 \cdot 10^{-9}$ cm/s and tracer diffusion coefficient $D^* = 1 \cdot 10^{-12}$ cm <sup>2</sup> /s were both taken from Ref. [148]. Background concentration was fixed to 0% and the gas was set to be 100% $^{18}\text{O}_2$ . The substrate was assumed to be completely blocking for oxygen transport. . . . .	98
7.2	Sketches of the two different setups for the tracer incorporation and the tracer diffusion step: In (a) half of the YSZ layer is covered with a metallic barrier layer leading to enrichment of $^{18}\text{O}$ in the other half. In (b) only a small region in the center of the YSZ layer is exposed to the gas phase leading to a bar-like enriched region. (c) After tracer implementation the barrier is removed and a part of the surface can be modified arbitrarily; here a platinum film is applied normal to the oxygen enriched region (exemplified with a bar-like profile). Then the diffusion step is performed in vacuum. . . . .	98
7.3	A comparison of different lateral diffusion profiles after specified diffusion times at 500°C. (a) An initial semi infinite concentration step is assumed; (b) surface exchange driven diffusion profile according to eq. 7.1, it is assumed that the gas exchange only takes place at the edge of the layer; (c) Profile resulting for an initial finite concentration box. The box width is set to 10 $\mu\text{m}$ . Surface tracer exchange coefficient $k^* = 6 \cdot 10^{-9}$ cm/s and tracer diffusion coefficient $D^* = 3 \cdot 10^{-10}$ cm <sup>2</sup> /s were both taken from Ref. [148]. The background concentration was fixed to 0% and the gas was set to be 100% $^{18}\text{O}_2$ . . . . .	100

7.4	XRD patterns of the investigated YSZ layers on (a) sapphire; (b) magnesia; c) strontium titanate. The black dots in (b) and c) mark reflections caused by the corresponding substrates. Reflections marked (100) are actually (200) but obviously refer to the same crystallographic orientation. The individual structural parameters can be found in Table 7.1 and Fig. 7.5. . . . . .	104
7.5	Lattice constants of the crystallographic orientations found in the investigated samples. It is important to note that each lattice plane presented here is parallel to the substrate interface plane. The solid line represents the literature value of a macroscopic powder sample, see e.g. Ref. [106]. . . . .	105
7.6	AFM images of the surfaces of layers (a) MgO-PLD; (b) MgO-SG; c) STO-PLD; (d) STO-SG; (e) Sap-PLD 1; (f) Sap-SG 1; (g) Sap-PLD 2; (h) Sap-SG 2. The circle in (d) indicates a dome shaped (111) oriented grain, while the square marks a flat (100) oriented one. The arrow in (f) indicates a pore in the layer which reaches down to the interface. . . . .	106
7.7	Impedance spectra (open symbols) along with the corresponding fit curves (red and blue lines) of Sap-PLD 2 and Sap-SG 2 at 300°C in (a) Nyquist and (b) Modulus plots. The inset in (b) depicts the equivalent circuit to fit the data. $R_{Bulk}$ and $R_{GB}$ are the resistances for bulk and grain boundaries in YSZ. $CPE_{GB}$ and $CPE_{Stray}$ are the constant phase elements used to model the grain boundary and stray capacitance, see Ref. [18] and chapter 4.	107

7.8	ARRHENIUS plots of the conductivities of grain and grain boundaries of the YSZ films on (a) magnesia; (b) strontium titanate; (c) sapphire. The two black lines in each plot are bulk conductivities of 8% YSZ polycrystals. The solid black line consists of data measured in a tube furnace, while the dotted line was measured with interdigital electrodes on a heating stage. In the latter case the geometrical factor relating resistance and conductivity was calculated by the finite element method. . . . .	109
7.9	Lateral $^{18}\text{O}$ concentration profiles of Sap-PLD 1 and Sap-SG 1, see Table 7.1 for more information on the layers. The Cr/Au gas diffusion barrier was removed before measurement of each profile. In (a) and (b) profiles are shown after the incorporation step, ie. after a thermal gas exchange at 300°C in 97% $^{18}\text{O}_2$ . Graphs (c) to (f) display the diffusion profiles after diffusion at 500°C in ultra high vacuum. Diffusion times were 5400 s for Sap-PLD 1 (c) and (e)) and 2500 s for Sap-SG 1 (d) and (f). In (c) and (d) the diffusion profiles in YSZ with a free surface (vacuum-exposed) are plotted, while the profiles in (d) and (f) developed in YSZ under a Pt layer.	114

# List of Tables

2.1	Short list and description of electronic components used to design equivalent circuits to fit impedance data recorded in this thesis. CPE is an acronym for Constant Phase Element. . . . .	25
4.1	Calculated capacitances for a 100 nm thick YSZ layer with a grain size of 20 nm and an electrical grain boundary width of 4 nm on a 0.5 mm thick sapphire single crystal. The capacitances are normalized to the electrode length. . . . .	51
4.2	Capacitance values are averaged over the temperature range from 200°C to 400°C, resistance values obtained at 300°C and activation energies, all determined on layer A (105 nm thick) for different electrode geometries. For comparison, calculated substrate capacitances and activation energies of poly- and single crystalline YSZ are shown. Capacitances and resistances are normalized to the electrode length. Measured stray capacitances are averaged over values of $Q$ with $r > 0.98$ for the constant phase element in Fig. 4.1(c). . . . .	62

4.3	Stray and grain boundary capacitances as well as activation energies for transport through grain bulk and grain boundaries (GB) and the corresponding resistances at 300°C measured on layer B and C with different annealing times. Capacitances and resistances are normalized to the electrode length. Measured stray capacitances are averaged over values of $Q$ with $r > 0.98$ for the constant phase element in Fig. 4.1(c). . . . .	70
5.1	Physical and electrical parameters of the YSZ layers under investigation, as well as the activation energies of macroscopic reference samples for comparison. All thin films were annealed at 1200°C for 12 hours. GB means grain boundary, $E_a$ activation energy. . . . .	75
7.1	Substrates, geometrical parameters and activation energies of bulk and grain boundary (GB) conductivities in the YSZ thin films used in this study. No microstructural features were observed in the AFM image of the surface of STO-PLD, hence the grain size is listed as infinitely large. .	102
7.2	Estimated surface exchange coefficients at 300°C and diffusion coefficients measured at 500°C of the layers used in this study. Diffusion problem “step” denotes an experiment with an incorporation of the tracer in half of the sample, cf. left column in Fig. 7.9 and Fig. 7.2(a). “Box” corresponds to an incorporation step as in the right column of Fig. 7.9 and Fig. 7.2(b). Conductivity based diffusion coefficients $D^\sigma$ are compared to tracer diffusion coefficients $D^*$ of uncovered (“free”) and Pt covered YSZ. The tracer diffusion coefficient listed in the last row was measured in a YSZ single crystal by depth profiling, see Ref. [148]. . . . .	112

# Acknowledgements

In gewisser Weise gehört die Danksagung sicher zu den schwierigsten Kapiteln der ganzen Dissertation, immerhin ist sie sicherlich das meistgelesene, also sollte man sich doch ein paar Gedanken machen. Interessierten Laien seien an dieser Stelle jedoch die Kapitel 2, 6 und 7 ob ihrer bunten Bilder ans Herz gelegt. Ich denke aber, dass ich in ein paar Jahren, wenn mir mein Werk wieder in die Hände fällt, auch als erstes hier landen werde. Insofern ist das hier auch eine kleine Erinnerung an die Zeit als Dissertant, die ich ähnlich wie 0325384 so schnell wohl nicht mehr vergessen werde. Unvergessen sollen aber auch folgende Leute bleiben, quasi die *DRAMATIS PERSONAE* des vorliegenden Stücks:

Prof. Dr. Jürgen Fleig, der trotz stetig anwachsender Arbeitsgruppe immer Zeit für eine ausführliche Besprechung meiner Ergebnisse fand und mir auch die Gelegenheit gab diese in zahlreichen Veröffentlichungen und Konferenzen vorzustellen. Er war es auch, der mich durch seine hervorragenden Vorlesungen für die Elektrochemie begeistert hatte.

Prof. Dr. Werner Sitte, mein Zweitprüfer, der einst auf einer Konferenz als einziger den Weg zu meinem Poster fand.

Prof. Dr. Herbert "Hörbie/Herbie" Hutter, an dessen TOF-SIMS Höllenmaschine ich viele, teils schöne Stunden verbringen durfte und Prof. Dr. Frank Kubel, der meinen XRD Messungen Sinn einhauchte.

Mein langjähriger Zimmerkollege Dr. Martin Ahrens, bei dem ich immer ohne Voran-

meldung eine Privatvorlesung in Physik erhalten konnte und der außerdem ein begnadeter Karikaturist ist.

Und natürlich meine Kollegen während der Dissertation, deren Aufzählung ein bisschen Tradition in der Arbeitsgruppe geworden ist. Daher nun ohne wertende Reihenfolge und Anspruch auf Vollständigkeit: Dr. Alex Opitz, der Briefkastenonkel des wissenschaftlichen Alltags und Meister fernöstlicher Lebens- und Kampfkunst; Markus Kubicek, der als einziger authentisch meinen Wiener Grant auf alles teilen und zurückgeben konnte; Lukas Andrejs, dessen tschechisches Äquivalent aber auch nicht von schlechten Eltern ist; Steffi Huber und ihre Schokoladenvorräte, die sie unversperrt herumliegen lässt und dennoch nie auf mich sauer war; Dr. Elmar Völkl, das Comeback-Kid der Elektrochemie und neuerdings Dokumentationsfilmstar; Edvinas Navickas, whom i had the privilege to teach a word in his native language i do not speak: Sėjamasis avinžirnis; Tobias Huber, der immer tolle Sachen bestellt und sie zu noch tolleren zusammenschraubt; Dr. Till Frömling, der gar nicht mal ungehalten reagiert hat, als ich ihn spätnachts anrief um ihm eine Fehlermeldung an der SIMS vorzulesen; Dr. Judith Januschewsky, die bei diesem grottenschlechten Nerdrock-Konzert die ganze Zeit getanzt hat. Aber auch die neueren Zugänge Gerry und Sandra, denen ich noch nichts andichten konnte.

Besonderer Dank gebührt meinen Eltern, die mein Interesse an technischen Dingen geweckt haben und mir eine Ausbildung ermöglichten, für die sie selbst größere gesellschaftliche Hürden überwinden mussten, als sie mir je begegnet sind. Auch die “Lilly” [90] soll hier mehr als nur ehrenhalber erwähnt werden.

Zum Schluss besteht das Leben aber aus mehr als nur der Arbeit und dafür sorgten meine Geschwister, FreundInnen und natürlich meine liebe Isa. Danke für Alles!

# CURRICULUM VITAE

**Name:** Dipl. Ing. Matthias Gerstl  
**Geburtsdatum:** 27. Jänner 1984  
**Familienstand:** ledig

## Werdegang

etwa 03/2012 **Rigorosum**

01/2009 – 12/2011 **Universitätsassistent und Doktoratsstudium - TU Wien**  
Thema der Dissertation: *Grain boundaries and Interfaces in Thin Films of Yttria Stabilized Zirconia (YSZ)*  
Betreuer: Univ.Prof. Dipl.Phys. Dr. Jürgen Fleig

11/2008 **Diplomprüfung mit Auszeichnung - TU Wien**  
Thema der Diplomarbeit: *Stromgetriebener Einbau und Diffusion von Tracerionen in Yttrium stabilisiertem Zirconiumdioxid*  
Betreuer: Univ.Prof. Dipl.Phys. Dr. Jürgen Fleig

010/2003 – 11/2008 **Studium der Chemie** an der technischen Universität Wien  
Spezialisierung: „Chemistry and Technology of Materials“

2003 **Ableistung des Präsenzdienstes** in Linz Hörsching

06/2002 **Matura mit Auszeichnung**

1994 – 2002 **Bundesgymnasium 8 - Piaristengymnasium Wien**

1990 – 1994 **Piaristenvolksschule – Wien**

## Industriepraktika

2005 Borealis Agrolinz Melamine, Linz

2004 Borealis Agrolinz Melamine, Linz

2002 Praktikum bei OMV, Wien-Schwechat

## Sonstiges

2002 – 2010 Ehrenamtlicher Jugendleiter bei den Wiener Pfadfindern